2007

Investigation of Oxygen Growth Pressure Effects on Tio[subcsript 2-#]: Co

Erhong Hu

THE FLORIDA STATE UNIVERSITY

COLLEGE OF ARTS AND SCIENCES

INVESTIGATION OF OXYGEN GROWTH PRESSURE EFFECTS ON $TiO_{2-\delta}$: Co

By

ERHONG HU

A Dissertation submitted to the
Department of Physics
in partial fulfillment of the
requirements for the degree of
Doctor of Philosophy

Degree Awarded:
Spring Semester, 2007

The members of the Committee approve the Dissertation of Erhong Hu defended on February 21st, 2007.

_____
Stephan von Molnár
Professor Co-Directing Dissertation

_____
Patricia A. Stampe
Professor Co-Directing Dissertation

_____
Albert E. Stiegman
Outside Committee Member

_____
Peng Xiong
Committee Member

_____
Vladimir Dobrosavljevic
Committee Member

_____
Jorge Piekarewicz
Committee Member

Approved:

David Van Winkle, Chair, Department of Physics

Joseph Travis, Dean, College of Arts and Science

The Office of Graduate Studies has verified and approved the above named committee members.

For My Mom& Dad, My Husband and My Daughter

ACKNOWLEDGEMENTS

The first person I would like to thank is my thesis advisor, Dr. Stephan von Molnár, for his continuing advice, encouragement, and support throughout my graduate school years. He helped me not only with my physics, but also with my presentation skills. Besides being an academic advisor, Steve is also my role model of working hard, being serious in Science, and always being polite to others. I have been extremely fortunate to work for him and will always cherish my memories of MARTECH.

The next person I would like to acknowledge is my co-advisor, Dr. Patricia A. Stampe, for her tireless work helping me. She was always there to answer my physics questions, even before she is my co-advisor. Without her help it is hard to believe that this work could have been completed. I have benefited from and enjoyed working with her. Outside of physics, she is always there as a friend.

I also thank Dr. Robin J. Kennedy, Dr. Yan Xin and Dr. Peng Xiong. I thank Robin for his invaluable help since the very beginning. As a materials fabrication expert, he not only made the samples upon which this thesis is based, but he also instructed me. Thanks, Robin. I thank Yan for her kind cooperation in performing the all important TEM characterization for these studies. She instructed me to prepare good specimens, did the TEM spectroscopy for us, and was always there for discussions and questions. I would like to thank Peng (a member of my advisory committee and much more) for his help concerning my understanding of physics as well as revisions to conference proceedings, presentations and talk rehearsals, from which I benefit more than a lot.

I would also like to thank Dr. Glen Held, IBM T.J. Watson Research Center for his invaluable assistance in applying his programs to fit my magnetization data. I learned physics as well as computing skills from him.

I would also thank my former and current colleagues in the group. I thank Ray Kallaher, Jeff Parker, Jazcek Braden, Jelena Trbovic and Fonsie Guiliran for helping me to

develop experimental skills and equipment utilization. I thank Ray for introducing me to experimental physics and being always helpful. Jeff was a good person to discuss physics with; besides, he is always friendly. I thank Jazcek and Jelena for their invaluable help in utilizing lock-in amplifiers and cryostats. I thank Fonsie for the first instructions in operating thermal evaporators. I would also like to acknowledge the former Post-docs in our group: Dr. Cong Ren, Dr. Jens Müller, Dr. Steve Mcgill and Dr. Dan Read, for their continuous help and for being good role models. In addition I would like to thank other group members: Goran Mihajlovic, Khaled, Jennifer Misuraca, Yi, Pradeep, Ashwani, Xiaohang, Jeff, Jennifer Murray, as well as Dr. Hirst and her group. Their presence exposed me to new ideas and techniques; and they were there to help when it was needed.

Of course it would be impossible to finish the work without our gracious and expert MARTECH staff. I am grateful to Dr. Eric Lochner, Kurt Koetz, Ian Winger, Joe Ryan and Jim Valentine for their help with machines and technologies. I thank Linda Lynes, Roger Beck, Kathy Bailey and others in the MARTECH offices, for providing a smoothly functioning workplace and for their kindness to the people they work with.

I would also like to thank my additional committee members, Dr. Albert E. Stiegman, Dr. Vladimir Dobrosavljevic, and Dr. Jorge Piekarewicz for their cooperation and advice.

The work presented in this thesis was supported by DARPA–HR0011-04-1-0028 and National Science Foundation.

TABLE OF CONTENTS

LIST OF TABLES

LIST OF FIGURES

ABSTRACT

Room temperature ferromagnetic semiconductors not only play an important role in the development of spintronics, but also are interesting from the viewpoint of fundamental physics since they combine two important realms of condensed matter physics: magnetism and semiconduction. This dissertation presents a study on selected magnetic transition metal doped oxides as potential diluted magnetic semiconductors (DMS).

The goal is to understand the room temperature ferromagnetism (RTFM) mechanism in $TiO_{2-\delta}$: Co. Several steps have been taken to approach this problem. Polycrystalline and epitaxial $TiO_{2-\delta}$: Co thin films were deposited on (0001) α-Al_2O_3 substrates by PLD under well controlled growth conditions. Detailed characterization demonstrates that laser ablated $TiO_{2-\delta}$: Co under low oxygen growth pressure (PO_2) is a multiphase system with Co nanoparticles precipitated out of the TiO_2 lattice. Depending on PO_2, the samples show dramatically different magnetic behavior. For example, with PO_2 lower than a critical value a transition from a blocked magnetic state at low temperature to a superparamagnetic state at higher temperature is observed, which is a signature of superparamagnetic Co nanoparticles. For samples grown under higher PO_2, the blocking temperatures are higher than 350K, as determined from zero field cooled/ field cooled (ZFC/FC) measurements. In agreement with this observation, the hopping transport behavior expected in multiphase granular metal systems, $\ln(\rho) \sim T^{-1/2}$ is observed for most of the samples in the measured temperature range and low bias (linear I-V) regime. Related hopping conduction behaviour in magnetic fields and high electrical fields (non-linear I-V regime) will also be presented. Cross sectional TEM images provide further corroboration of the multiphase structure of these materials.

Preliminary work to understand the mechanism dominating the room temperature ferromagnetism in $SnO_{2-\delta}$: Co is also presented. To obtain optimal RTFM, films fabricated over a wide growth parameter space were examined through magnetic, transport, and microstructure characterization. This research suggested a uniform,

intrinsic ferromagnetism in $SnO_{2-\delta}$: Co films. Defects, such as oxygen vacancies and crystal lattice defects, are suggested to be the cause of RTFM.

CHAPTER 1

INTRODUCTION

1.1 Background

Modern semiconductor-based electronic technology has developed to attempt higher processing complexity. The number of transistors per square inch of integrated circuits is a common way to measure the complexity. Intel Corporation co-founder, Gordon E. Moore, noted that the processing power (speed and numbers of transistors) of computers increases following a log law as the overall cost per component decreases [1]. This is shown in figure.1.1.

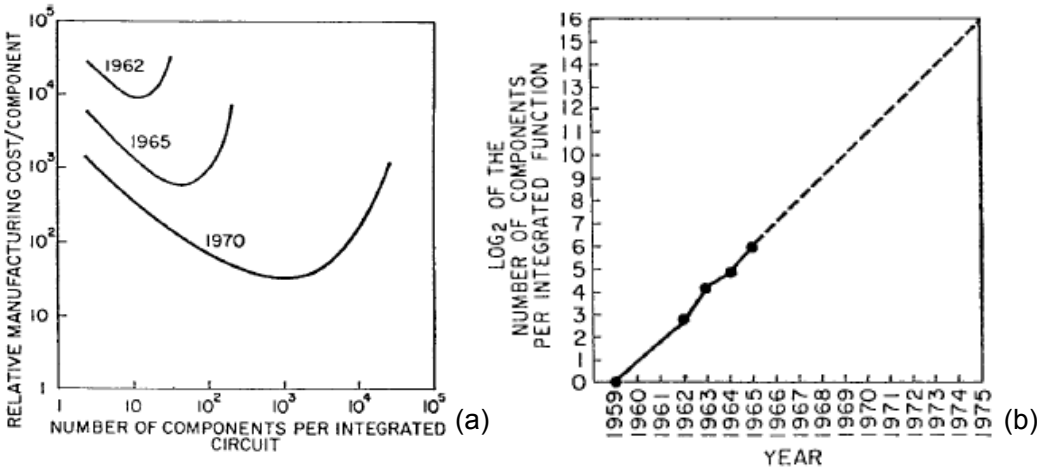

Figure1.1 The cost per component is almost inversely proportional to the number of components. The sharp increase beyond the minimum comes from the increased complexity at any time (a). Component count per integrated function grows exponentially following Moore's Law (b) (after Ref 1).

Although Moore's law was initially made in the form of an observation and prediction, the more widely it became accepted, the more it served as a goal for the silicon based semiconductor industry. Over the intervening time scientists and engineers have been working to push technology following this law to approach higher processing speed with accompanying device size shrinkage. However, even with the amazing modern technical innovations, the development of conventional semiconductor-based electronic

technology will be pushed to its limit because of anticipated difficulties. For example, one difficulty comes from SiO_2, which is the main gate oxide in the silicon industry. Since the gate oxide thickness must keep pace with the lateral dimension shrinkage, Moore's law requires the thickness of the gate oxide to diminish while maintaining the overall device function. However unacceptably high gate leakage currents occur with oxide films thinner than 1.5nm, resulting in unwanted power dissipation. In this situation, the conventional viewpoint of designing and building devices must be broadened or changed. Scientists and engineers are inevitably faced with the quantum mechanical world, which they have tried to avoid for a long time. R. Feynman described future computers in his mind and proposed a new field at very "small" scales in his famous quotation "there is plenty of room at the bottom" [2]. Now some new concepts and technologies have been developed, of which spintronics is promising to be revolutionary.

1.2 Spintronics

Traditional microelectronics technology is based on semiconductor devices, where electron charge is utilized to store data and process information. In contrast, magnetic materials take advantage of electron spin. It is very interesting to combine these two natural freedoms of electrons in technology and utilize the electron spin to carry information. There exist "up" and "down" states of electron spin, rather than conventional on and off states for charge based electronics. Furthermore, the quantum mechanical nature will allow intermediate spin states, depending on the energy, in other words, the spin carries more information than the charge. Once the electron spins are exploited in technology, it could be possible to approach the small computers described by Feynman and gain improvements in material requirement including less heat generation, power consumption, and possibly higher processing speed [2]. There exists the possibility of opening a new era of technology. Spintronics, a new, intensely pursued topic of research, proposes this idea.

"Until recently, the spin of electron was ignored in mainstream charge-based electronics. A technology has emerged called spintronics (spin transport electronics or

spin based electronics), where it is not the electron charge but the electron spin that carries information, and this offers opportunities for a new generation of devices combining standard microelectronics with spin-dependent effects that arises from the interaction between the carriers and the magnetic properties of the material " [3].

Since the spins are closely linked to magnetism, spintronics is closely linked to magnetism. Work in magnetism, together with work in semiconductor physics, optics and superconductivity, was the starting point in applied and fundamental spintronics research in the past two decades.

According to David Awschalom, et al. [4], there exist three categories in spintronics. The first category, the most mature one up to now, is metal based spintronics. Magnetic and non-magnetic metals are a class of materials very well studied and relatively easy to make compared to good quality semiconducting materials. This category of spintronics has been successful in providing effective information storage. For example, one existing magnetic device is read-heads for magnetic data storage technology, which exploit the Giant Magneto-Resistance (GMR) effect and are based largely on magnetic metals. The GMR observation in layered films of iron and chromium [5] was the first manifestation of the plausibility of technological usage of spintronics. GMR is explained by the fact that parallel ferromagnetic orientation of adjacent magnetic layers gives lower resistance than the case of anti-parallel orientation, since the spins with opposite orientation scatter off the anti-parallel layer. A large external magnetic field tends to align the FM layers' magnetization, as shown in figure 1.2. Another important class of technique in metal-based spintronics is the magnetic tunnel junction with two ferromagnetic layers sandwiching a nonmagnetic insulator, which is already making an enormous impact on information storage technology. Tunneling magneto-resistance in these structures is a large and intriguing field which will not be fully covered in this thesis.

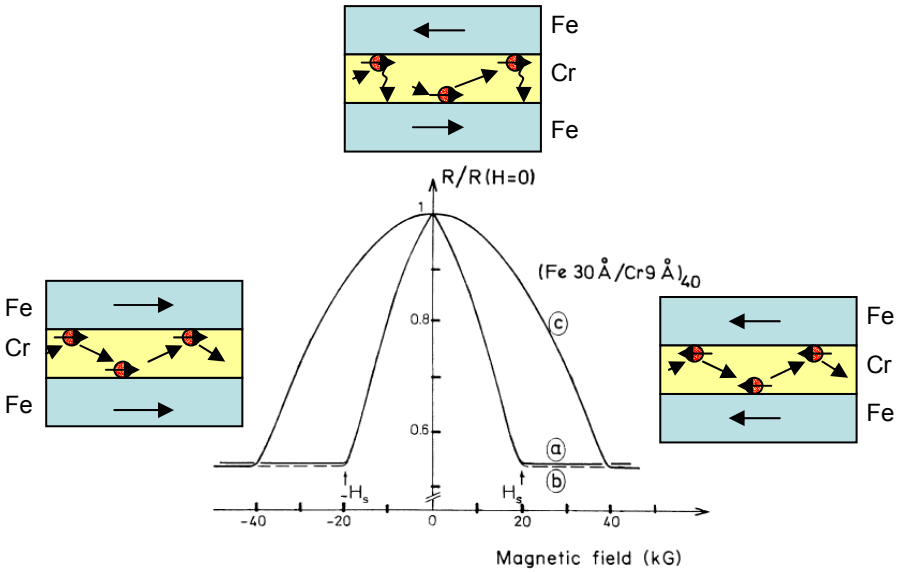

Figure 1.2 Magnetoresistance of (Fe 30Å/Cr 9Å) $_{40}$ at 4.2K. Current is applied along a certain direction in the film plane with the applied field parallel to the current (curve a), applied field in the layer plane and perpendicular to the current (curve b) and applied field perpendicular to the layer plane (curve c). At low applied magnetic field, the magnetic Fe layers are not aligned, and scattering results in high resistance. At high field, magnetic layers are aligned and lower resistance occurs (after Ref 5).

The second category is semiconductor based spintronics, which I will discuss later.

The third category of spintronics is looking forward toward the more distant future. This category is based on devices that manipulate the quantum spin states of individual electrons. The spintronics quantum logic gates in this category could enable the construction of quantum computers on a large scale, which could surpass standard computers greatly for certain tasks. The research areas in this category are: ions in magnetic traps, “frozen” light, nuclear magnet resonance of molecules in liquid, etc.

The second category of spintronics is semiconductor-based spintronics. Compared to metal based spintronics, semiconductor spintronics is more promising, since besides attractive improved functionalities, this category of spintronics is compatible with existing semiconductor technologies. The elements of the semiconductor-based spintronics device are three-fold: a spin injector to inject spin polarized carriers, a magnetically neutral region to transfer and/or manipulate information written in the spins of electron, and a spin detector. To utilize spins rather than charges in information processing, there are certain technical problems to solve, as stated below:

- How to efficiently inject spin polarized currents into a semiconductor;
- How to maintain the information stored in spin-polarized current during the transport and manipulation;
- How to measure the spin polarized current once it is there.

The first problem comes from the difficulty in interfacing magnetic materials with semiconductors in such a way that electron spin information is preserved upon passage across the interface between the materials. In the case of metallic ferromagnetic injectors, the spin injection efficiencies are low; one of the physical causes being that in passing from a ferromagnetic metal to a semiconductor, the conductivity decreases because a dead magnetic layer exists [6] so that the spin polarization in the magnetic metal is lost [6]. If a magnetic semiconductor is applied as a spin injector, these problems will be absent. Furthermore the semiconductor device will make it easier to combine spin electronics into traditional semiconductor electronics technology. Thus it is highly desirable to make this kind of ferromagnetic semiconductors. They must have favorable magnetic and transport properties, as well as Curie temperatures above room temperature, and must be compatible with common semiconductor materials.

1.3 Physics Motivation

As described above, magnetic semiconductors are key materials for semiconductor-based spintronics technology and will certainly be utilized for devices in the future. Furthermore, it is also interesting to study this kind of material from the physics viewpoint since it combines two important realms of condensed matter physics: magnetism and semiconduction.

In fact there has been research on ferromagnetic semiconductors for decades. The earliest studied ferromagnetic semiconductors were mainly europium chalcogenides, such as rock-salt type EuO, EuS, and chromium chalcogenides such as spinel type $CdCr_2S_4$ and $CdCr_2Se_4$ (see [7] and references therein). In these concentrated ferromagnetic semiconductors there is a periodic array of magnetic elements, shown in figure 1.3(a); there are various theoretical models to explain the ferromagnetism, e. g.

competitive ferromagnetic superexchange interaction in insulating materials. Since these kinds of materials are usually difficult to grow; more importantly, they are only magnetic at temperatures far below room temperature (<100K), there is very little hope of applying them for today's application for room temperature spintronics. Instead, an alternative called diluted magnetic semiconductor (DMS) has become an important class of materials for potential room temperature application.

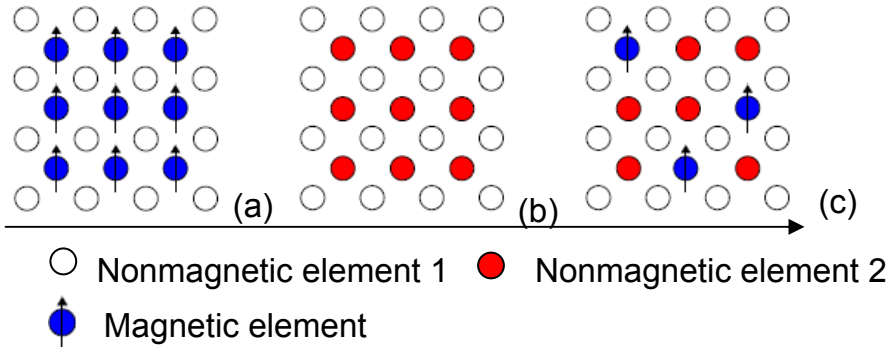

Figure 1.3 Schematic pictures of (a) a concentrated magnetic semiconductor, (b) a non-magnetic semiconductor, and (c) a diluted magnetic semiconductor (after Ref 8).

In a DMS, magnetic atoms are doped into a nonmagnetic host, as shown in figure 1.3(c). Various hosts have been explored as a DMS host material. The II-VI semiconductors such as ZnSe and CdTe have been intensely studied ([7] and [9]). The physical reason comes from the fact that the valence of the cations (2+) matches the valence of common magnetic transition metal ions such as Mn. Also, magnetic metals can be easily introduced into the II-VI hosts with very high concentration. However, Mn can neither introduce nor bind carriers of either n-type or p-type to mediate ferromagnetic interactions, but only give rise to the presence of localized spins. It has been demonstrated that the interactions among Mn ions are antiferromagnetic and it is difficult to enhance the magnetic transition temperature from ≤ 4K. Thus the II-VI hosted DMSs are not attractive for real life spintronics applications.

After Ohno et al. published their discovery of Curie temperatures as high as 110 K in MBE deposited Mn doped GaAs, with Mn content from 1.5% to 7% in 1996 [10], intense research has been focused on diluted magnetic semiconductors with the host material

being III-V semiconductors, such as GaAs, GaN, InAs, etc. The physical motivation comes from the fact that when a divalent transition magnetic ion substitutes a trivalent cation, a hole will be induced and possibly will be able to mediate ferromagnetic interactions. A well known calculation applied the Zener model and predicted that it is possible to increase the Curie temperature of p-type DMSs upon Mn incorporation [10]. In fact, the reported Curie temperatures of III-V hosted DMSs have been greatly enhanced up, e. g. with $x = 8\%$, ($Ga_{1-x}Mn_x$)As shows a Curie temperature of 170K in thin films [11]. However, there still are no reports of Curie temperature above room temperature. Thus the III-V hosted DMSs are still not feasible candidates for room temperature spintronics.

Theoretical work also predicts that ferromagnetism is stable in a DMS based on a wide band gap semiconductor [10]. Many transition metal oxides are well known as wide band gap materials and can be doped heavily with both n and p-type carriers. This can be promising for making DMSs, since once localized spins are introduced into the oxide semiconductor, there can be strong ferromagnetic interactions through RKKY exchange and double exchange. Furthermore they are transparent at room temperature and thus have potential for optical applications. There has been considerable experimental work in diluted magnetic oxides (DMO) research, particularly after the observation of room-temperature ferromagnetism in transparent transition metal-doped TiO_2 [12]. However there is considerable controversy in the current reports in these DMOs such as, what is the interplay between transport and magnetic properties? Furthermore, there exists a more fundamental question: is the material a single phase magnetic semiconductor or a system in which transition metal particles precipitate out of the oxide lattice resulting in phase segregation? We are interested in this fundamental physical question: whether the diluted magnetic oxides are a single phase system, or multiphase systems such as granular metals. I have done a series of physics experiments on laser ablated $TiO_{2-\delta}$: Co films and it turns out that under certain preparation conditions this particular diluted magnetic oxide is a kind of phase segregated system, with Co granules embedded in TiO_2 lattices.

The organization of this thesis is as follows: (1) I set the stage by an introduction of the background and motivation, which is done in this chapter. (2) Then I will focus on a review of the general growth considerations and physical properties studies on DMOs. (3) After the review I will describe my own characterization work on the material of $TiO_{2-\delta}$: Co. This chapter will make up the bulk of this thesis as this has been my primary project. In this part a number of subjects will be covered, including a general introduction and fabrication considerations, followed by subdivision into three parts: detailed SQUID magnetic measurements and the observation of superparamagnetism, hopping transport determination, and Transmission Electron Microscopy (TEM) measurements for detailed structural observation. A central theme in the characterization portion is how the physical properties may be affected by the film deposition conditions, particularly growth oxygen pressure. (4) There is another chapter devoted to $SnO_{2-\delta}$: Co thin films, on which I have worked for a while and have observed some interesting phenomena such as uniform, single phase magnetism, Mott type variable range hopping (VRH), etc. A systematic study by annealing the samples to cross the metal-insulator transition (MIT) has been inconclusive to this date. (5) Finally there is a summary chapter, where I will summarize the project and give a conclusion.

CHAPTER 2

DILUTED MAGNETIC OXIDES

2.1 Introduction

After the observation of room temperature ferromagnetism in anatase TiO_2: Co [12], there has been intensive research on transition metal doped oxides and the transition metals responsible for the magnetic phenomena. Up to now most DMO related experimental work has been focused on host materials such as TiO_2 ([12]-[49]), ZnO ([50]-[84]), and SnO_2 ([85]-[96]). In addition there are also reports on $La_{0.5}Sr_{0.5}TiO_{3-\delta}$ [97], Cu_2O [98], and NiO [99] as host matrices to make DMS. Ideally, as mentioned earlier, a DMS should be ferromagnetic at room temperature (T_c>300K), with the ferromagnetism originating from intrinsic exchange interactions mediated by charge carriers. In other words, it may not be applicable if magnetic impurities precipitate out of the oxide matrix during fabrication and are responsible for the room temperature ferromagnetism. Experimental researchers have been extensively working on this topic of phase segregation by means of physical characterizations, such as structural, magnetic, magneto-optic and transport measurements. However there appears to be no definite conclusion on this issue, even from the same individual research groups ([19]-[21] by Chambers group, and [16], [24] and [27] from the Maryland group). Here I will discuss and summarize some of the recent results in DMOs, with the emphasis on TiO_2 based DMOs. There will also be discussions on ZnO and SnO_2 based materials. My goal is to shed some light on the following questions:

- What characterization techniques will address the sample quality and magnetic origin?
- What preparation methods and growth conditions can lead to magnetic particle precipitation?
- What is the origin of the observed room temperature ferromagnetism (RTFM)?

- How do transport and magnetotransport relate to the microstructure?

2.2 TiO_2 based DMOs

2.2.1 Introduction

TiO_2 is attractive as a DMS host material. It occurs in several forms such as rutile, anatase and brookite, of which the unit cells are decribed in figure 2.1. The most stable phases of TiO_2 are rutile and anatase. All of these polymorphs have wide band gaps; which potentially enable the introduction of both deep donor and deep acceptor levels. Thus TiO_2 can be doped heavily with both n- and p- type carriers. The polymorphs are also transparent in the visible region and with a high refractive index, which enable optical application for this material.

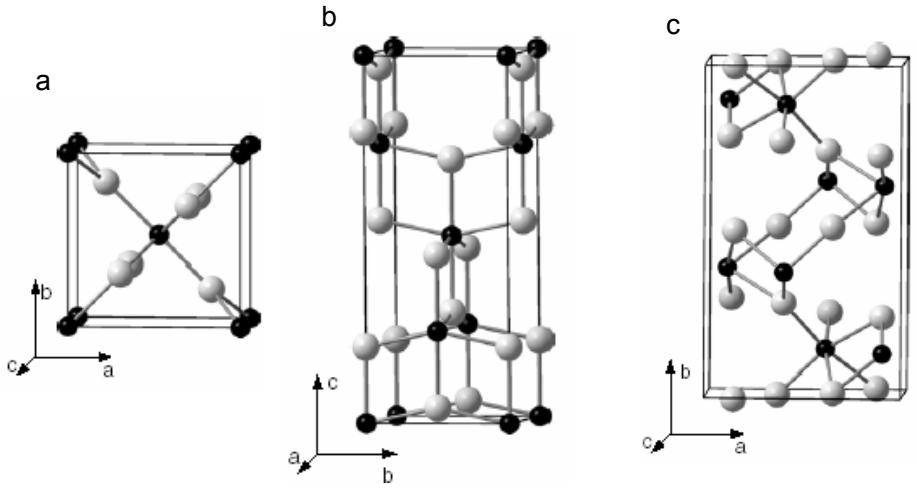

Figure 2.1 Schematic diagrams of the polymorphs of TiO_2: a) rutile, b) anatase and c) brookite. The phases of anatase and rutile are most stable.

In these structures the rutile phase is usually thought to be most thermally stable in bulk phase. The anatase phase is not stable at temperatures higher than 650°C, even though there are calculations showing that anatase should be more stable [44]. Furthermore successful fabrications of anatase films have been reported, as described in the next paragraph. Traditional research in TiO_2 has been focused on the rutile phase due to its relatively simple crystal structure. However recent spintronics research also

turned to the anatase phase, because in anatase TiO_2 the n-type carriers have higher mobility than in the rutile phase. Our review will describe both the rutile and anatase phases.

Single phase TiO_2 films have been fabricated on a selection of lattice matched substrates and with proper growth conditions. As demonstrated in table 2.1, epitaxial TiO_2 films, both in rutile and anatase phase, can be deposited on (100) $SrTiO_3$ (STO) with Pulsed Laser Deposition (PLD). Anatase TiO_2 films with high crystallinity and atomically defined interfaces can also be prepared on lattice matched (-0.2%) (100) $LaAlO_3$ (LAO) by laser molecular beam epitaxy (Laser MBE). Thus the metastable-in-bulk anatase TiO_2 can be grown as a stable form in films if the correct lattice matching is present with the substrate. Undoped TiO_2 films have also been prepared to attempt to find the best conditions before growth of the doped material, with both anatase phase ([12], [16], [22], [31]) and rutile phase ([24], [27]) utilizing different fabrication techniques. It should also be pointed out that the properties of pure TiO_2 films strongly depend on the growth conditions. For instance an increasing substrate temperature during growth can drive the anatase TiO_2 films from a metallic to an insulating phase [31]. In most TiO_2 based DMO studies, cobalt is introduced as a magnetic dopant ([12]-[47]) with a few exceptions ([48]-[49]).

Table 2.1 Crystalline TiO_2 phases.

Material	Structure	Band gap	Substrate	Fabrication	Reference
Rutile TiO_2	a=4.59Å c=2.96Å	3eV	(100)$SrTiO_3$ (111)$SrTiO_3$	PLD	[13] [14]
Anatase TiO_2	a=3.78Å c=9.52Å	3.2eV	(001)$LaAlO_3$ (001) $SrTiO_3$	Laser MBE	[14], [15]

2.2.2 General Fabrication

The structure and physical properties of Co doped TiO_2 films strongly depend on the substrate, growth method, growth conditions (such as oxygen partial pressure, substrate temperature, growth rate, etc). Special treatment after growth may also affect the properties, as will be discussed in this chapter.

2.2.2.1 Substrates

Many substrates have been used to grow cobalt doped TiO_2 films. Since the magnetic element has low atomic content compared to the Titanium element, the overall crystal structure is expected to be almost identical with that of TiO_2. It is desired to make epitaxial films of magnetic impurity doped TiO_2. Epitaxial film growth is greatly dependent on the mismatch between the lattice of the desired phase of TiO_2 and the corresponding lattice of the substrate. As mentioned earlier, $SrTiO_3$ (STO) and $LaAlO_3$ (LAO) have been used as substrates for growth of pure TiO_2 films because of the low lattice mismatches. They are also popular for Co doped TiO_2 film growth, such as STO(001) for anatase ([12], [16], [17], [18], [19], [20], [23], [25], [29]), LAO(001) for anatase ([12], [16], [17], [20], [21], [22], [23], [24], [28]), and (001) LAO for poly crystal rutile-anatase phase after post annealing [26]. Sometimes both TiO_2 phases grow on a single substrate. For example, a very small amount of rutile (111) in addition to anatase(001) has been reported on a (100) STO substrate [17]. The lattice mismatch between the anatase (001) form of TiO_2 and STO (001) is -3.1% with cube-on-cube orientation, making possible epitaxial anatase TiO_2 growth. With a=3.79 Å in LAO, the lattice mismatch between the anatase TiO_2 form and LAO is tensile with a value of +0.08%. The lattice mismatch between anatase TiO_2 (001) and LAO (001) is as small as -0.26% along $[100]_{anatase} \parallel [100]_{LAO}$ [20]. Sapphire has been used for rutile phase films ([23], [24], [27], [30]). The anatase phase of $Ti_{1-x}Co_xO_2$ can also be grown on $LaSrAlO_4$ (LSAO) [31], where the lattice mismatch is compressive (-0.79%). Rutile phase $Ti_{1-x}Co_xO_2$ has also been grown on Si or quartz by reactive co-sputtering [32]. Anatase polycrystalline phase can also be obtained on Si/SiO_2 through liquid delivery MOCVD followed by heat treatment [33]. Anatase films can also be grown on Si substrates with PLD, with STO/TiN as a buffer layer [34].

2.2.2.2 Consideration of growth method and conditions

There are many techniques being used to fabricate thin films of Co doped TiO_2. Molecular beam epitaxy (MBE) ([12], [19]-[22], [30], [44]) and pulsed laser deposition (PLD) are most frequently used ([16]-[18], [23]-[24], [27]-[29], [31], [34]-[35]). The

techniques of sputtering ([25]-[26], [32]), metalorganic chemical vapor deposition (MOCVD) [33] and ion-implantation ([36]-[38]) have also been used to deposit thin films. Furthermore sol-gel ([39]-[40]) and solid state reactions [41] are also used to make powders. The physical properties, such as RTFM and Co precipitationof the fabricated materials not only depend on the growth method, but also are greatly influenced by the growth conditions.

OPA-MBE has been employed and favored by some researchers even though it is relatively complicated to operate. In the first report of RTFM in anatase TiO_2: Co, the samples were prepared by combinatorial molecular beam epitaxy (MBE) [12]. There have been a large number of reports on films fabricated with various MBE techniques, as summarized in table 2.2. MBE is a complex diffusion system with many control factors. Nevertheless, compared to Pulsed laser Deposition (PLD), MBE can produce layers with very abrupt interfaces and good control of thickness, doping, and composition. The reason is a higher degree of control. During growth in MBE, reflection-high-energy-electron-diffraction (RHEED) is widely employed to monitor film surface crystallographic and morphological properties. For oxide growth an oxygen plasma is necessary [50], since normal oxygen molecules are not sufficiently active to oxidize the metal even for very slow growth rates. In other words, oxygen plasma assisted molecular beam epitaxy (OPA-MBE) is often the preferred technique.

So far there has been no definitive explanation of the origin of RTFM in MBE fabricated TiO_2: Co films. Consistent intrinsic ferromagnetism has only been reported by the Japanese groups ([12], [30], and [43]). Kim et al. reported that RTFM originates from cobalt clusters which are present in MBE fabricated anatase TiO_2: Co films and were accelerated with thermal treatment at 400°C, resulting in 20~60nm Co clusters [22]. Chambers et al. first reported that RTFM was only associated with samples without Co clusters, and samples with enriched-Co region are consistently nonmagnetic; they also pointed out that the growth termination with oxygen plasma cooling results in nonmagnetic films while cooling without plasma results in magnetic films, respectively [19]. They claimed, furthermore, a slow growth rate (0.18-0.6nm/min) resulted in better crystallographic quality single crystal films without cobalt clustering [20]. From the listed

reports in the table 2.2, Co clustering behavior is observed with growth rates from as slow as 0.1nm/min to as high as 30nm/min. The most recent paper from the Chambers group claims that Co segregates into nanoscale clusters, and that these clusters are responsible for RTFM [21]. A detailed review of this fabrication technique of Co doped TiO_2 films is given by Chambers et al. [20] and references therein.

Sputtering is also a popular way to make doped films or layered films, as summarized in table 2.3. The substrate temperature, $T_{s,}$ in this technique is relatively low, ranging from room temperature to 450°C, in comparison to $T_s = 600 - 700^o C$ in MBE and PLD techniques. However a recent report showed that $T_s = 750^o C$ results in the best crystallinity [46]. As shown in figure 2.2, with the highest T_s, a smallest full-width at half maximum (FWHM) from XRD is observed, indicating the best crystallinity.

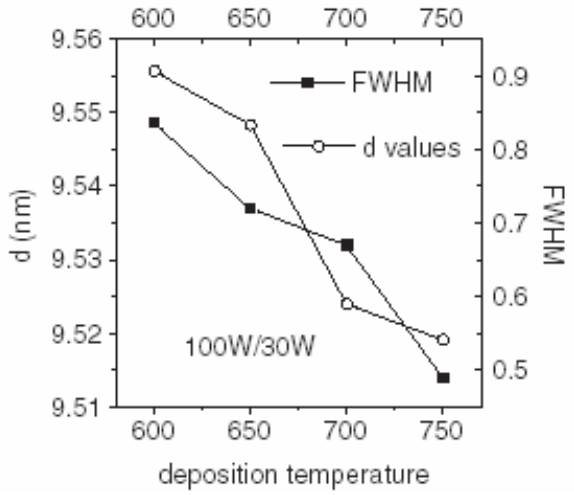

Figure 2.2 Dependence of substrate temperature of the lattice constant and FWHM from XRD measurements. The films are fabricated by co-sputtering Co and TiO_2 (after Ref 46).

There is also controversy about the presence of cobalt clusters in TiO_2: Co films fabricated by sputtering (sometimes followed by post annealing). As shown in table 2.3, no cobalt clustering was reported in earlier work. However a recent report on sputtered TiO_2: Co films fabricated by methods of co-sputtering and alternative sputtering [46] demonstrates that pure cobalt metal clusters are observed on the surface of the films, even though the films are epitaxial with very sharp film-substrate interfaces and cobalt is

Table 2.2 A list of reports of Co doped TiO_2 films fabricated using MBE.

Phase	Co content	Substrate	Fabrication technique	T_s (°C)	Growth pressure (Torr)	$Rate_{growth}$ (nm/min)	Tc (K)	Notes	Co clusters	Ref
Anatase	0~0.08	LAO(001), STO(001)	Laser MBE	677 ~727	$1*10^{-6}$ ~$1*10^{-5}$	N/A	>400	M_s: 0.32μ_B/Co	No	[12]
Anatase	0.01~0.1	STO, LAO	OPA MBE	550 ~750	$2*10^{-5}$	1.8~2.4	>300		No	[19], [20]
Anatase	0.05	LAO(001)	OPA MBE	570	2*10-5	6	>300		Yes	[21]
Anatase	0~0.1	LAO(001)	Laser MBE	650	$1*10^{-6}$ ~$1*10^{-5}$	0.1	>300		Yes	[22]
Rutile	0.01~0.1	r-sapphire	Laser MBE	400	$1*10^{-8}$ ~$1*10^{-4}$		>300	AHE	No	[30]
Rutile	0~0.12	r-sapphire	Laser MBE	400	$1*10^{-7}$~$1*10^{-4}$		>300	AHE	No	[42]

Table 2.3 Thin films of Co doped TiO_2 fabricated by sputtering

Phase	Co content	Substrate	Fabrication technique	Growth T(°C)	pressure (Torr)	$Rate_{growth}$ (nm/min)	Tc (K)	Notes	Co clusters	Ref
Anatase	0.08	STO(100)	Magnetron sputtering	550	Ar-O_2: $2*10^{-6}$ ~$2*10^{-4}$	3~5.4	>300	M_s: 0.87 or 0.57 μ_B/Co n: $2*10^{18}$~$5*10^{22}$	No	[25]
Layered films	0.04 ~ 0.09	LAO(001)	Magnetron sputtering	RT	Ar $2.5*10^{-3}$		>300	M_s: 1.325 μ_B/Co	No	[26]
Rutile	0.03 ~ 0.12	Si/quartz	Reactive co-sputtering	250 ~450	$3*10^{-4}$	1.5~2.6	>400	M_s : 0.95 μ_B/Co	No	[32]
Anatase	0.01 ~ 0.07	LAO	Sputtering Annealing	750	N/A	N/A	>300	Very mall MR	Yes	[46]

Table 2.4 Thin films of Co doped TiO_2 fabricated using PLD.

Phase	Co content	Substrate	Laser energy density	Laser wave length	T_s (°C)	PO_2(Torr)	Growth rate (nm/min)	Tc (K)	Notes	Co clusters	Ref
Anatase	0~0.15	STO(001), LAO (001)	1.8J/cm^2		700	$1*10^{-5}$ ~$1*10^{-4}$	N/A	1180, 700	M_s: 1.4μ_B/Co	yes	[16]
Anatase rutile	0.01~0.07	LAO(001) STO(001)		1064nm	750	$1*10^{-3}$	30	>300	M_s: 1.7μ_B/Co	yes	[17]
Anatase	0.04	STO (001)	1.5J/cm^2	248nm	600	$1*10^{-7}$~$1*10^{-4}$	0.2	750	M_s: 1.7μ_B/Co	yes	[18]

Table 2.4 –continued

Anatase rutile	0.07	LAO r-sapphire		1064nm	750	$1*10^{-3}$	20	>300	M_s: 1.7 μ_B/Co 0.6 μ_B/Co,	Yes	[23]
Anatase rutile	0, 0.02	LAO r-sapphire	1.8J/cm^2		700	Vac, 1mT H_2+Ar		>300	Hall or AHE	No	[24]
rutile	0~0.04	r-sapphire	1.8J/cm^2		700	$2*10^{-8}$		>300	AHE+SPPM	Yes	[27]
anatase	0.07	LAO(001)	1.8 J/cm^2		700	$2\sim4*10^{-5}$		>300	Co^{2+}, Co^{3+}	No	[28]
anatase	0.04	STO(001)	1.5 J/cm^2	248nm	600	$3.3*10^{-7}$	0.2	>300	Postannealed M_s: 1.7 μ_B/Co	Yes	[29]
anatase	0~0.05	$LaSrAlO_4$ LAO(001)	1.0 J/cm^2	248nm	700	$0.5\sim1*10^{-6}$		>300	n: $1*10^{-17}\sim2*10^{-1}$	No	[31]
anatase	0.04	Si	1-3 J/cm^2	248nm	500	$3*10^{-5}$		>300	STO/TiN as buffer	Yes	[34]
rutile	0.07	c-sapphire		1064	750	$5*10^{-5}$ $\sim3*10^{-3}$	20	>300	$\ln\rho \propto T^{-1/2}$	Yes	[35]

Table 2.5 A list of reports on transport and magneto transport properties in Co doped TiO_2 films.

ρ @RT (mΩ*cm)	n(cm^{-3}) and μ (cm/s*V)	ρ vs. T	MR	Co clustering	Notes	Ref
100~1000	10^{18}		60% @2K and 8T, ~2% @5K and 8T	No	Co at%: 0.07 anatase	[12]
650	$2.1*10^{18}$	Bandlike and oxygen vacancy contribution	40% @3K and 8T	Yes	$T_c = 1180K$ Co clusters	[16]
2, 13.4	$2*10^{18}\sim5*10^{22}$	Semiconducting; Magnéli phase like behavior		No	Vacuum ($2*10^{-8}$Torr) growth H_2-Ar 1mTorr growth; AHE	[24]
$20\sim10^4$	$10^{18}\sim10^{22}$, 0.1	Semiconducting	-0.4% @100K	No	AHE	[30]
20~200	$1*10^{17}\sim 2*10^{19}$ μ=10cm^2	Semiconducting		No	PO_2 controls n Systematic variation	[31]
50~1000	10^{18}	$\ln\rho \propto T^{-1/2}$		Yes	Hopping conduction	[35]
10~1000	$10^{18}\sim10^{22}$, 0.1	semiconducting		No	AHE, consistent and systematic	[42]
>10M	$5.16*10^{19}$	N/A	Small, 0.2% @2K	Yes	Annealed at 750°C in vacuum, Co clusters	[46]

Here in table 2.2 –2.5, M_s means the saturated magnetization, AHE the Anomalous Hall Effect, and MR the magnetoresistance.

in a +2 oxidation state inside the film. Furthermore, the saturated magnetization is found to be independent of carrier concentration [46].

The most prevalent technique in the fabrication of potential oxide based DMS is PLD, also called laser ablation. This technique is also favored by us. The advantage of this technique is that it is relatively easy to utilize. It has also proved to be successful in depositing materials of complex stoichiometry. Many materials that are normally difficult to deposit by other methods, especially multi-element oxides, have been successfully deposited by PLD. The main components in a PLD apparatus are a vacuum system, a laser, and optics. In a typical PLD process, a pulsed laser beam hits a ceramic target surface, forming a vapor; a thin film of the material of interest is then formed when the vapor condenses on a substrate, whose temperature is usually precisely controlled. The $TiO_{2-\delta}$: Co films and $SnO_{2-\delta}$: Co films studied in this work were all deposited in this manner. Sometimes two or more targets are used. Similar to the methods of MBE and sputtering, growth conditions are also crucial to deposit the desired films. Particularly an optimal substrate temperature of around 700°C is required to grow the best crystallographic quality of films of TiO_2 based DMOs ([31], [49]); and the oxygen partial pressure is usually controlled to adjust the oxygen vacancy concentration, which is expected to supply charge carriers.

There is also controversy concerning RTFM and cobalt clustering in PLD fabricated films. That cobalt atoms substitute into the TiO_2 lattice without the presence of Co enriched regions has been reported. For example, Cui et al. reported cobalt substitution into anatase TiO_2 lattice with cobalt content of 7%, but there is no evidence showing that their samples are ferromagnetic [28]. Intrinsic RTFM consistent with AHE and MCD has only been obtained in Japan [31]. The Maryland group reported both clustering and substitution in RTFM films depending on the Co content [16]. There was a report of carrier mediated RTFM evidenced by AHE [24]. However later on the same group claimed that AHE was observed in samples containing superparamagnetic Co particles [27]. Thus the Co clustering problem in samples fabricated by PLD still exists, as summarized in table 2.4. A major objective of this thesis is to determine if Co has been dissolved into rutile TiO_2. This will be described in chapter 3.

Metalorganic chemical vapor deposition (MOCVD) is another method to synthesize Co doped TiO_2 films. Anatase $Ti_{1-x}Co_xO_2$ can be grown on SiO_2 (200nm)/Si with liquid-delivery MOCVD [33]. The deposition temperature is 400-500°C. After annealing in vacuum ($1x10^{-6}$ Torr) for 1 hour at 700°C, films of $x \leq 0.05$ show ferromagnetism without a clustering phase, while for films with $x = 0.05$ a second phase of $Ti_{1-x}Co_x$ was detected [33].

More recently ion-implantation into TiO_2 has been applied for possible DMS fabrication ([36]-[38]). Cobalt ions can be implanted into single phase TiO_2 thin films as well as single crystal TiO_2. Cobalt clusters were detected via the observation of superparamagnetism when cobalt ions were implanted 200nm deep into MBE fabricated anatase TiO_2 films [36]. It is also reported that Co^{2+} was formed when cobalt was ion-implanted into rutile single crystal; furthermore RTFM was detected in the resulting samples [37]. Ferromagnetism induced by exchange interaction mediated by oxygen vacancies was also reported [38].

Sol-gel ([39]-[40]) and solid state reaction [41] are usually used to obtain powders, which can be heat treated with easier control, and post-growth heat treatment is usually applied for sol-gel fabricated powders to enhance the ferromagnetism or to change the structures of the powders. For example, for powders of TiO_2: Co, annealing at 220°C in air can produce amorphous ferromagnetic powders; annealing at 450°C will result in ferromagnetic powders with predominant anatase plus minor rutile phase; and annealing in 1000°C will result in rutile phase powder with pure paramagnetism [39]. It is also reported that the TiO_2: Co powders fabricated by sol-gel and followed by hydrogenation at 573K can be ferromagnetic without cobalt nanoparticles [40].

2.2.2.3 Effects of Co content in the prepared films

By whatever fabrication method, the Co concentration x in $Ti_{1-x}Co_xO_{2-\delta}$ is usually intentionally determined beforehand. In general the value of x is smaller than 0.15 to avoid the formation of Co clusters from excess Co atoms. Vegard's law is usually utilized to examine if the cobalt ions are dissolved into the TiO_2 matrix via substitution.

The Vegard's law states that there is a linear relationship between the substituted impurity concentration and the lattice constant if the bonding properties of the solute and solvent are similar. The relation between lattice constant and Co concentration has been examined by many groups ([12], [16], [31]).

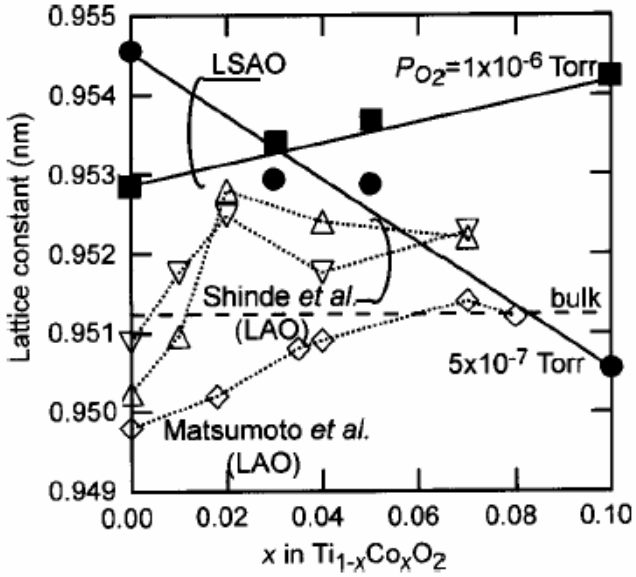

Figure 2.3 The lattice constant as a function of Co concentration in anatase $Ti_{1-x}Co_xO_2$ films. The solid square symbols are for films fabricated by PLD with PO_2=10^{-6} Torr and solid circles are for films with PO_2=5*10^{-7}Torr. The solid lines are a guide to the eye (after Ref. 31). The triangle symbols are from the results of Shinde et al. (after Ref. 16) and the diamond symbols are from Matsumoto et al.'s work (after Ref. 12). The horizontal broken line represents the value of bulk anatase TiO_2. (after Ref. 31).

Matsumoto et al. reported Co incorporation into the TiO_2 lattice with the evidence of Vegard's law for x up to 9% [12]. However Shinde et al. claimed that clustering of excess Co will occur with $x > 1.5-2\%$. In their report Vegard's law is followed only with $x \le 1.5-2\%$ and a saturation of the lattice constant is observed with x>2%. Yamada et al. [31] did a similar study and found that the relation depends on the oxygen growth pressure (PO_2) [31]. With $PO_2 = 10^{-6} Torr$, the lattice constant, which is deduced from the (004) anatase peak in XRD measurements, increases with x up to 10%; while for $PO_2 = 5*10^{-7} Torr$, the lattice constant decreases with x up to 10%. The authors claimed that the monotonic changes suggest successful fabrication of the solid solution films. The explanation of the different slopes is not given [31]. They summarized studies of the lattice constant vs. Co concentration with a single graph for comparison, as

shown in figure 2.3. It should be noted that earlier results (figure 2.2) shows the lattice parameter is strongly dependent on growth conditions [46]; furthermore, it has been noted that the lattice parameter will vary with film thickness [14]. Thus it is difficult, unless growth conditions and film thickness are exactly duplicated from sample to sample, to obtain conclusive evidence on cobalt substitution from lattice parameter data alone.

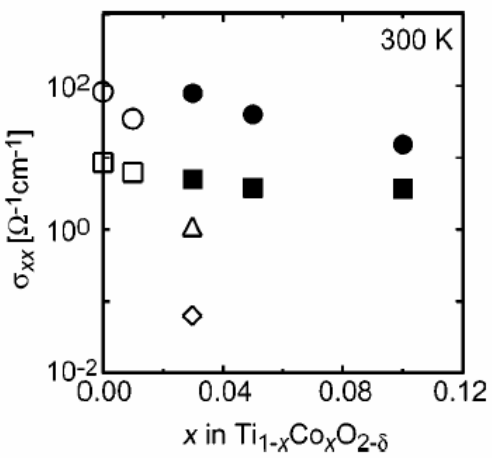

Figure 2.4 Mapping of σ-x space. Solid and open symbols represent ferromagnetic and paramagnetic information, respectively. The circle, square, triangle and diamond symbols represent samples with partial oxygen growth pressure of 10^{-7}, 10^{-6}, 10^{-5} and 10^{-4} Torr, respectively (after Ref. 42).

The appearance of RTFM depends on both Co concentration (x) and the electrical conductivity (σ_{xx}). This is shown in figure 2.4 by Toyosaki et al. [42]. In the figure, the solid symbols stand for ferromagnetic samples, and the open symbols are for paramagnetic samples. The ferromagnetic phase only occurs for a Co concentration higher than 3% with a conductivity higher than 1 Ω^{-1}-cm^{-1}. Furthermore, the observed Anomalous Hall Effect (AHE) was observed for the ferromagnetic samples in figure 2.4, providing more evidence of intrinsic ferromagnetism [42].

Kim et al. fabricated Co doped anatase TiO_2 films by OPA-MBE with variable Co concentrations of 4%, 7% and 10% [22]. Even with a very slow growth rate of 1Å/min and a resulting smooth film surface, Co precipitates out as Co clusters for all three concentrations. All samples are ferromagnetic up to 400°C, as demonstrated in figure 2.5. After a thermal treatment at 400°C, the saturated magnetization increased from

0.1μ_B/Co to 1.55μ_B/Co with observation of Co clusters with 20~60nm diameters. The only systematic trend is that the magnetic coercivity increases with Co concentration. Either this originates from the size and shape of the Co islands, or the magnetic correlation among the cobalt islands. There is no clear explanation for the coercivity trend with the cobalt concentration in the article [22].

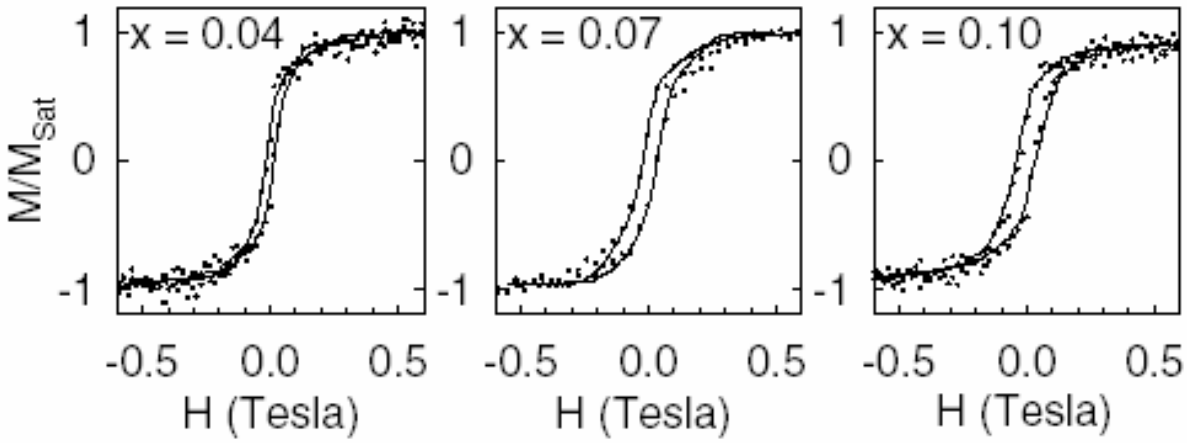

Figure 2.5 Magnetic hysteretic curves of anatase $Ti_{1-x}Co_xO_2$ films at 400°C with magnetic filed parallel to films (dotted) or normal to the films (solid lines). The difference between the two field orientations is negligible, indicating that the magnetic anisotropy is not considerable. The estimated coercivity is 150, 250, 400 Oe for $x = 0.04, 0.07, 0.10$ films (after [22]).

2.2.3 Co clustering in TiO_2 based DMOs

A hysteretic M vs. H loop at room temperature gives the first evidence of RTFM. This ferromagnetism can originate from intrinsic exchange interaction or extrinsic sources such as ferromagnetic impurity segregation. This is demonstrated in figure 2.6, where the upper band diagrams show the effect on spin-polarization for the two cases. For extrinsic DMOs, the RTFM is caused by magnetic impurity clusters, which are a secondary phase in TiO_2. For intrinsic RTFM, the magnetic impurity Co is substituted into the matrix of the TiO_2 in the form of Co^{2+} or Co^{3+} ions. The ferromagnetism comes from the interactions among distant magnetic impurities. The charge carriers, either electrons or holes, are playing a crucial role to mediate the exchange. This is the mechanism of RTFM in conventional DMS. Generally in carrier mediated magnetism, further phenomena are expected, such as AHE, which is a well known ferromagnetic

response of the charge carriers in ferromagnetic semiconductors [30]. Of course ferromagnetism needs first to be confirmed by magnetic measurement, with either of the mechanisms dominating.

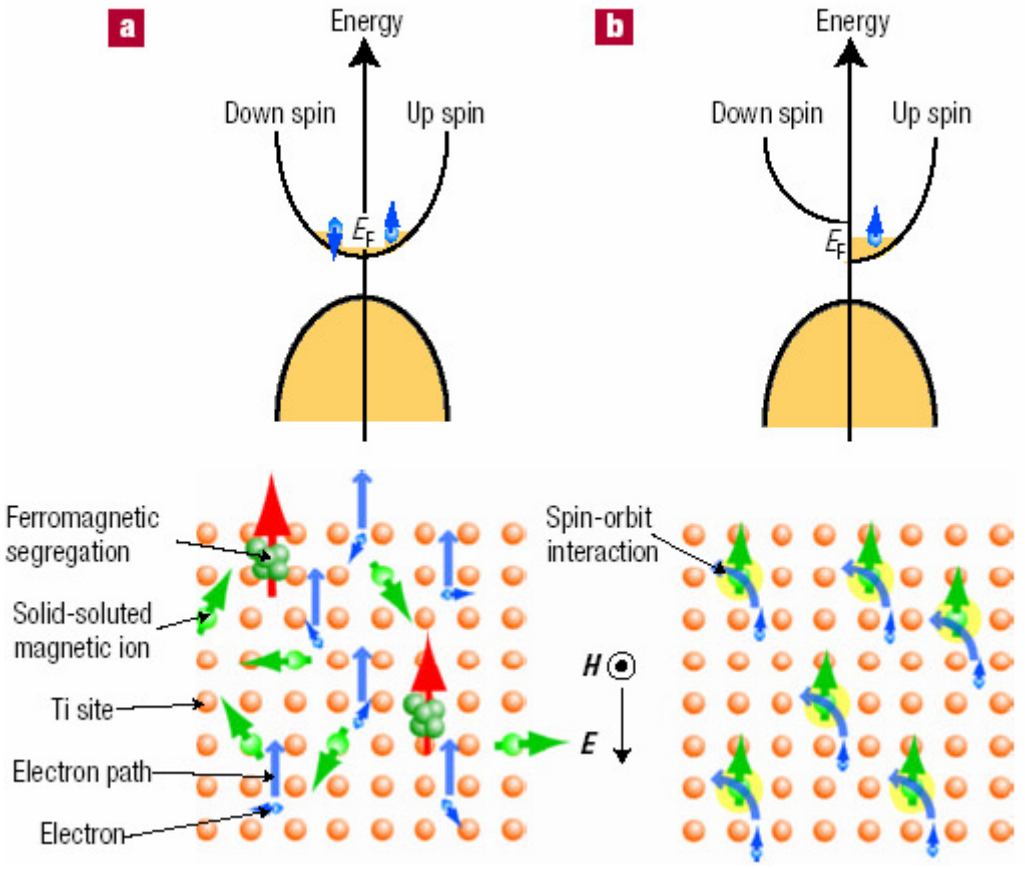

Figure 2.6 Schematics for extrinsic and intrinsic RTFM in TiO_2 based DMOs. a) FM originates from magnetic impurity segregation, and the band diagram shows no spin polarization. b) FM originates from interaction among distant localized magnetic moments mediated by charge carriers (after Ref. 30).

It is not sufficient to determine the nature of the magnetism only by magnetic measurements using a magnetometer. The reason is that RTFM in thin films of TiO_2: Co may come from extrinsic effects like cobalt metal enriched regions or cobalt clusters. In fact deduction of magnetic properties from magnetization measurements alone without careful examination of possible extrinsic effects can often be misleading [43]. Micro structure characterization must be performed to examine the uniformity of compositions and the possible cobalt segregation in the film. Table 2.6 lists various characterization techniques that can be used to examine possible nonuniform magnetic dopant distributions or magnetic element clusters in DMOs.

X-ray diffraction (XRD) is a non-destructive technique for characterizing single crystals or crystalline powder for their crystal structures, secondary phases, and other crystal parameters such as crystal defects. The XRD pattern is a fingerprint of the periodic atomic arrangements in a given materials, and is very often performed for detection of impurity phases other than the oxide phase. However since the impurity precipitation amount in DMOs is as small as a few atomic percent, the XRD may not be sensitive enough to detect the impurity phase.

Table 2.6 characterization techniques to determine impurity precipitation

Characterization method	**Definition of impurity precipitation?**
X-ray diffraction	Impurity phase
TEM	Clusters of impurities in microstructure (high resolution)
SEM	Clusters of impurities on surface
AFM	Clusters of impurities on surface
RHEED	Precipitation on surface
Electron Probe Microscopy	Lateral composition nonuniformity
Secondary ion mass spectroscopy	Perpendicular composition nonuniformity

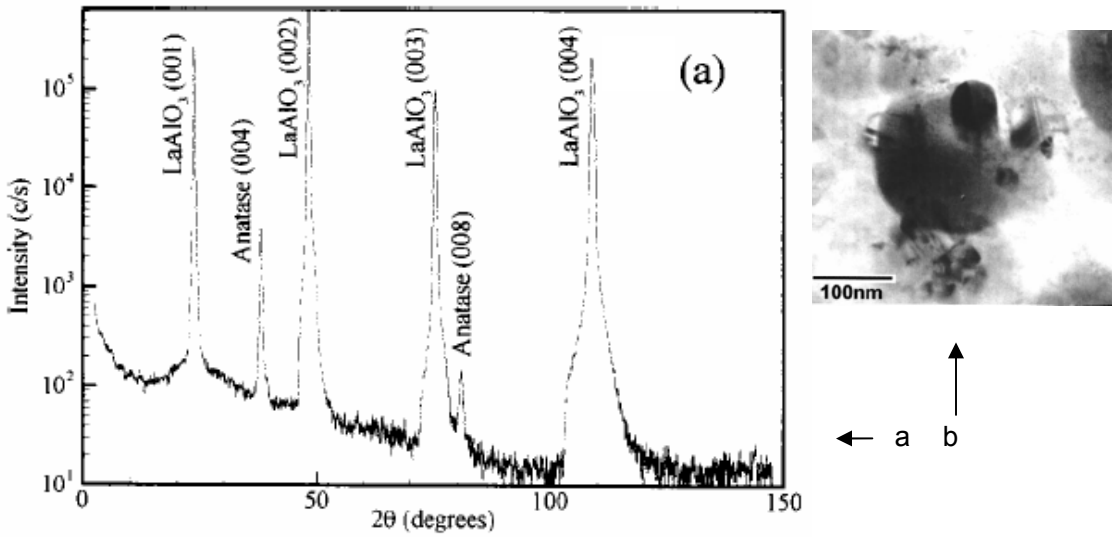

Figure 2.7 XRD and TEM characterization of the laser ablated anatase TiO_2: Co on LAO. a) X-ray diffraction failed to detect phase from Co clusters. b) TEM shows the presence of small clusters on the film surface. Further (EDS) and electron diffraction measurements confirmed that these clusters are face centered cubic (FCC) crystal cobalt metal (after Ref. 23).

In contrast transmission electron microscopy (TEM) can precisely detect possible precipitation on the atomic scale. Then element content detection methods, such as energy dispersive spectroscopy (EDS), can be used to identify the elemental content of

the TEM observed clusters. An example can be seen in figure 2.7, where TEM detected cobalt metal clusters which were unable to be detected by XRD [23].

Other than EDS, an X-ray-absorption near-edge spectroscopy (XANES) can be used to measure the chemical states of the dopant Co, which should be Co^{2+} or Co^{3+} if cobalt is successfully dissolved into the lattice of TiO_2. If the XANES is identical with that of a reference cobalt metal, cobalt metal clusters are present [29].

The scanning electron microscope (SEM) is, in fact, a kind of microscope, which utilizes electrons instead of light to magnify the surface of specimen with a larger magnification compared with a conventional light microscope. It can be applied to look at the film surfaces. The SEM creates a 2-dimensional image and is able to detect possible precipitation on comparatively large areas of specimen with a resolution of 1~20nm. However, unless the clusters are on the surface, they will not be seen with this technique.

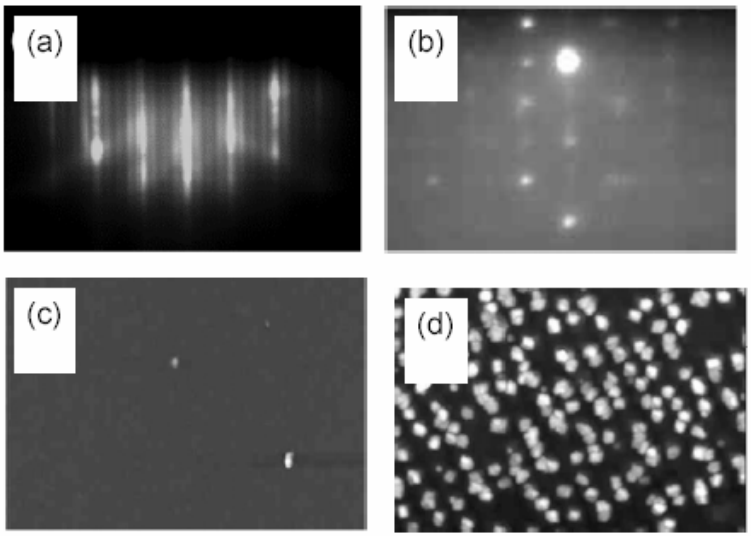

Figure 2.8 RHEED patterns and AFM images of $Ti_{1-x}Co_xO_2$ grown by MBE. a) A streaky RHEED pattern. b) A spotty RHEED pattern. c) A flat and clean surface observed in by AFM. d) A rougher multiphase polycrystalline film is observed in an AFM image where the particles on surface are composed of crystalline rutile as revealed by TEM (not shown). a) and c) are from the same sample, and b) and d) are from the same sample (after Ref. 20).

Atomic force microscopy (AFM) and reflection-high-energy-electron-diffraction (RHEED) are also used to examine surfaces. AFM examines the topography of a specimen and

thus can detect possible cluster precipitation on the surface of a film. In AFM a fine tip is brought into atomically close contact with a sample surface without actually touching the surface by sensing the attractive or repulsive force (~1 nanoNewton) between the probe tip and the surface. The tip is then moved back and forth over the sample surface, and can measure the topography with almost atomic resolution.

RHEED examines the perfection of the surface of the sample on a larger scale and can infer surface precipitation. If a surface is atomically flat, then RHEED patterns are sharp and streaky. If a specimen has a rougher surface, the RHEED pattern is more diffuse. Figure 2.8 shows an example of how RHEED patterns can indicate the surface quality of films, which was confirmed with AFM topography observation. The flat clean surface observation in AFM corresponds to a streaky RHEED pattern and a rough surface corresponds to a spotty RHEED pattern [20].

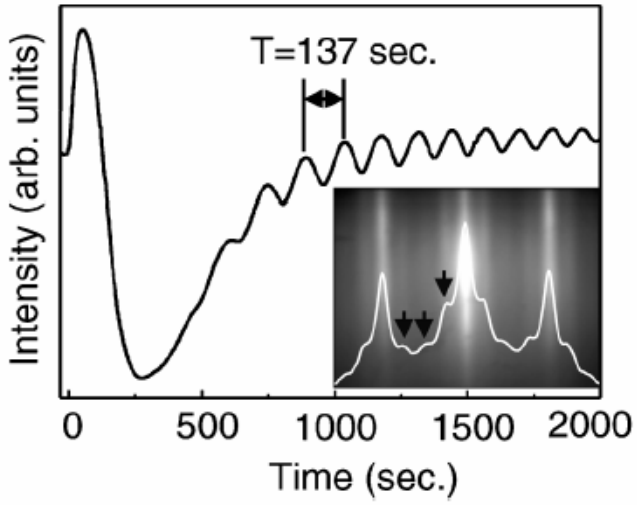

Figure 2.9 RHEED oscillations during deposition. The three additional lines in the inset profile represent a weak (4×1) surface reconstruction pattern (from Ref. 22).

In general during a layer-by-layer film growth, RHEED oscillations will occur. The reason is that a perfect initial surface results in a relatively high reflectivity of the specular spot; as a layer-by-layer growth starts, the island steps of the forming monolayer will partially scatter the incident electron beam, resulting in a decreased reflected intensity; and when a new monolayer completes, the surface is flat again, resulting in another maximum in reflected intensity. This feature makes RHEED a

particularly effective technique to monitor the film growth in MBE or PLD. Figure 2.9 shows clear RHEED intensity oscillations of the specular spot during the growth of $Ti_{0.93}Co_{0.07}O_2$ film by MBE, indicating that the film has grown epitaxially in layer-by-layer growth mode. The three weak streaks are due to (4×1) surface reconstruction [22].

Besides the precipitation detection on surfaces, electron probe microanalysis (EPMA) can examine the uniformity of composition along the lateral direction of samples, and secondary ion mass spectrometry (SIMS), in the perpendicular direction. Any detected magnetic impurity segregation may contribute to magnetic signals and result in extrinsic ferromagnetic signals.

2.2.4 Extrinsic ferromagnetism vs. intrinsic ferromagnetism

As mentioned before, magnetic measurement, i.e. a hysteretic magnetic moment vs. magnetic field curve is a straightforward way to observe room temperature ferromagnetism. A commercial superconducting quantum interference device (SQUID) may be used for magnetic measurements to detect signal as low as 10^{-6}—10^{-8} emu at temperatures up to 400K, whereas a vibrating sample magnetometer (VSM) can enable one to measure higher temperatures over 1200K with a magnetic moment sensitivity of 10^{-5}—10^{-7} emu. It is a general routine to perform magnetic measurements to check the existence of the RTFM for Co doped TiO_2 films.

As listed in tables 2.2 -2.4, the RTFM situation varies between various experimental groups. Apparently the ferromagnetism depends strongly on growth method and growth conditions. It has been shown that ferromagnetism is often observed in black tinged TiO_2: Co films with $PO_2 < 1mTorr$, while the green tinged films having the same cobalt concentration and grown at 3mTorr are non-magnetic [45]. A possible explanation is that oxygen deficiency promotes cobalt diffusion into clusters. However there is also a report of the RTFM in rutile TiO_2: Co with $PO_2 = 3.4mTorr$ [35]. The measured magnetic moment varies from $0.32\mu_B$/Co to above $1.7\mu_B$/Co in the literature. Thus it is hard to draw a precise conclusion.

In the following paragraphs, I want to discuss extrinsic and intrinsic RTFM from the viewpoint of magnetic data. An example of the magnetic data indicating RTFM is shown in figure 2.10 a). As pointed out in the last section, it often happens that the observed RTFM could originate from cobalt clusters.

Extrinsic Ferromagnetism Sometimes it is not complicated to identify extrinsic ferromagnetism, if the magnetic properties of a DMO are close to or even identical with those of pure Co metal. Cobalt metal has a Curie temperature of 1404K and a magnetization of 1.7μ_B/Co. The clusters of impurity Co metal in matrix of TiO_2 can result in similar magnetic properties for the overall material ([16], [17], [18], [23], [29]). For instance Shinde, et al. [16] have reported for their RTFM Co-doped TiO_2 films, the magnetization at 5K is 1.4 μ_B/Co, which is comparable to the value of 1.7 μ_B/Co in bulk Co; the curve of magnetization vs. temperature indicates the Curie temperature of the film is ~1180K, also comparable to the value of 1404K for bulk cobalt. In a microstructural examination the TEM image indicates 20~50nm clusters, which are labeled with Arabic numbers in the image. The clusters are Co metal clusters as confirmed by electron energy loss spectroscopy (EELS)/EDS. The magnetization and T_c values strongly indicate that it is these clusters that define the RTFM.

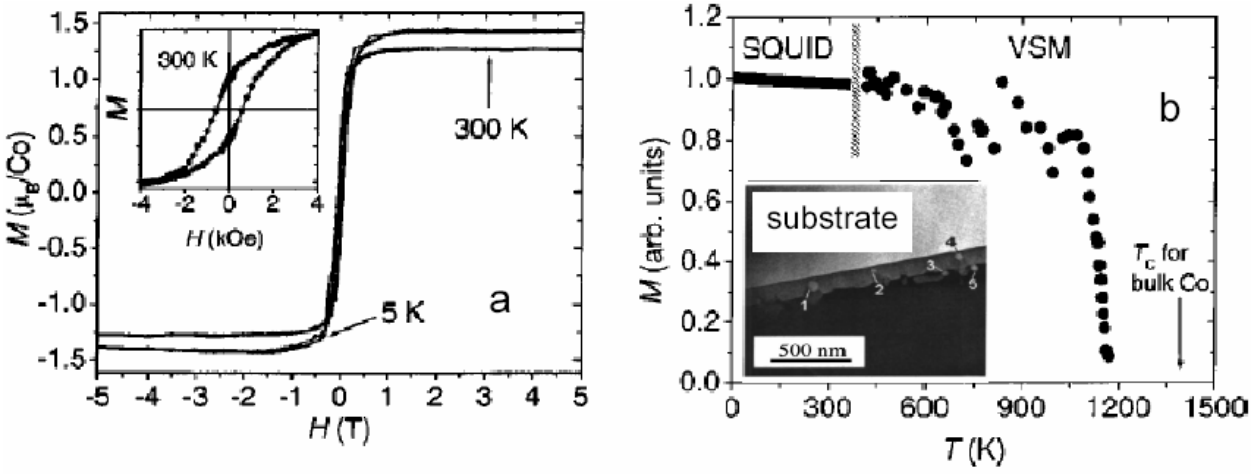

Figure 2.10 Magnetic data for a film of rutile $Ti0_{.93}Co_{0.07}O_2$. a) Magnetization as a function of magnetic field at 5K and 300K. The data at 300K is also shown in an expanded scale in the inset. b) Magnetization as a function of temperature with an inset TEM image (after Ref. 16).

On the other hand, if the measured saturation moment and Curie temperature is far from that of Co metal, the RTFM mechanism may occur for different reasons. Depending on the high or low spin state of Co ions, the intrinsic Co doped TiO_2 will present various saturated moments. The electron configuration of Co is [Ar] $3d^7 4s^2$. The Co ion should be either Co^{2+} or Co^{3+} if thermal equilibrium is assumed at the generally high substrate temperature during growth. The electron configuration of Co^{2+} is [Ar] $3d^7$ and for Co^{3+} is [Ar] $3d^6$. Thus the high spin states of Co ions will either be $S = 3/2$ or $S = 4/2$ with saturation magnetization of $3\mu_B$/Co or $4\mu_B$/Co. Low spin states will result in $S = 1/2$ or $S = 0$ with at most $1\mu_B$/Co of saturation magnetic moment (see figure 2.11). This kind of saturation magnetic moments have been observed together with absence of Co clustering [12, 19]. For instance the observed value of $0.32\mu_B$/Co magnetization, corresponding to a low spin state of Co ions in TiO_2: Co films, rules out Co metal [12].

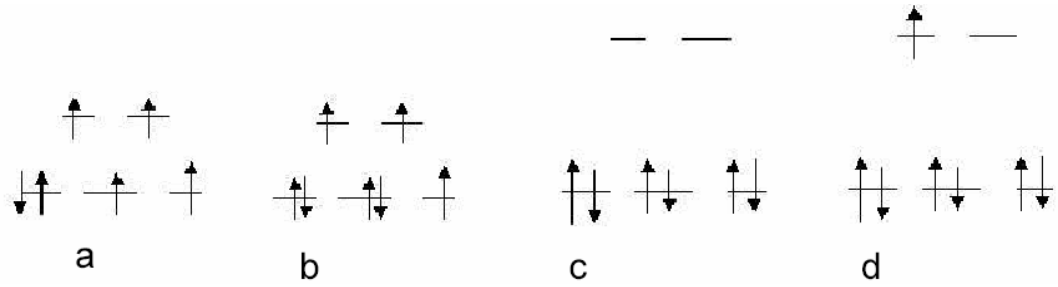

Figure 2.11 d orbital occupancy in Co^{3+} (a and c) and Co^{2+} (b and d) ions. The high spin states of $S = 2$, $S = 3/2$ are shown in a), b) respectively; and the low spin states of $S = 0$, $S = 1/2$ are shown in c) and d), respectively.

Another way to detect Co clusters at the nanometer scale is to measure the zero field cooled (ZFC) –field cooled (FC) magnetic response of the samples with a SQUID. To utilize ZFC-FC technique, one treats the cobalt clusters as giant molecules suspended in a solid solution of TiO_2. In the following paragraphs, a brief description of fine magnetic particles in a solid dispersion will be given.

To seek an equilibrium magnetization state of a specimen, the free energy, one part of which is the magnetic energy, must be minimized. Introducing the concept of magnetic domains may greatly decrease the self-energy of the magnetization in its own field

(magnetic energy F_D in [100]) and thus decrease the free energy. A domain wall is the boundary region between two domains. For specimens with dimension higher than a critical value, multi-domain formation will be energetically favored resulting in minimum total energy and a stable equilibrium state; if the dimension of the particle is lower than some critical value, a single-domain, minimum total energy, configuration will result [101].

In nature, as pointed out by Bean and Livingston, "single domain particles are not completely isotropic, but will have contributions to their total energy associated with the external shape of the particle, imposed stresses, or crystal structure itself" [101]. In a solid system containing single domain particles and at low temperatures, the particles have nonzero magnetization on laboratory time scales. Now they are said to be in a "blocked" state. In this situation the magnetization reversal can occur only by magnetization rotation. This requires work to be done against strong anisotropy energy, and thus requires a high magnetic field to switch the magnetization, in other words a nonzero H_c is expected at low temperatures [101].

For simplicity, for a single-domain particle whose anisotropy is uniaxial in symmetry, the anisotropy energy is $E = KV\sin^2\theta$. Here K is the anisotropy energy per unit volume, V is the volume of the particle, and θ is the angle between the moment and the symmetry axis of the particle, as shown in figure 2.12 a).

When a large magnetic field is applied, the single domain particles in an assembly are aligned and fully magnetized. As pointed out by Néel [102], after the field is removed, the remanence of the particle will decay as $M_r = M_s * \exp(-t/\tau)$, where M_r is the remanence, M_s is saturated magnetization, t is the time after removing the magnetic field, and τ is the relaxation time. The relaxation time has the expression of $1/\tau = f_0 \exp(-KV/kT)$, where f_0 is a frequency factor and is on the order of 10^{-9}sec^{-1}, and k is the Boltzman constant. The exponential dependence can be understood from the anisotropy energy dependence on θ, as demonstrated in figure 2.12 b) [101].

The thermal equilibrium state corresponds to zero remanence. As stated above, the probability of the remanence decay process is proportional to $\exp(-KV/kT)$. Thus to approach thermal equilibrium within laboratory time scales, sufficiently high temperatures should be applied so that the thermal energy can overcome the anisotropy energy to reverse sufficient number of particles. Now the system shows paramagnetic behavior without remanence or coercivity, and each nanoparticle can be viewed as a single spin which is usually as large as $10^3 - 10^5 \mu_B$. At this time the system is called a "superparamagnetic" system because of the "super" large spins in each particle.

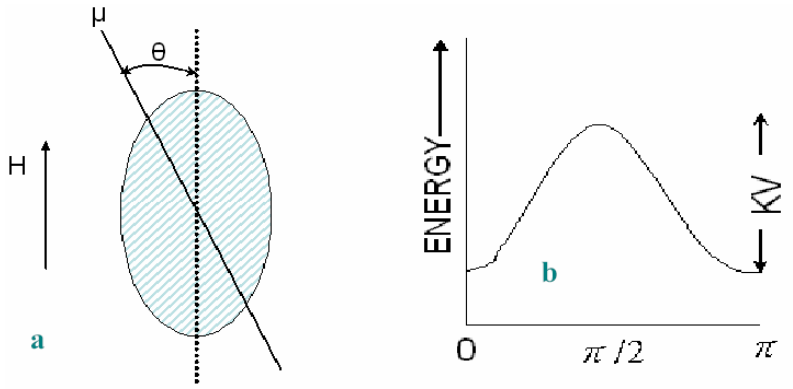

Figure 2.12 classical pictures for uniaxially anisotropic particles. a) single domain particle with uniaxial anisotropy. b) dependence of energy on θ without field. Here θ is the angle between magnetization μ and the easy symmetry axis. Both figures are from reference 100.

To measure the transition temperature from the blocked state to the superparamagnetic state, a rough method is to take $\tau = 100s$, which is on the laboratory time scale. Now we have $1/100 = 10^{-9}\exp(-KV/kT)$, and then at the transition temperature $KV = 25kT$. The critical temperature of the transition is called blocking temperature T_b.

T_b can be measured by a zero field cooling-field cooling (ZFC-FC) process. To measure signals via ZFC-FC, the sample containing single domain particles is first brought to liquid helium temperature in zero applied magnetic field. During this cooling, the particles will tend to magnetize along energetically preferred directions in the lattice; since the orientations vary, the net moment of the system will be zero when approaching the lowest temperature. Even when a small external field is applied, the

moments will remain locked into the preferred orientations. A ZFC magnetization vs. temperature curve is measured while heating the sample at a constant rate. As the temperature increases, more thermal energy is available to disturb the system, and more moments will align with the external field direction in order to minimize the Zeeman energy term until the net moment of the system reaches a maximum where the largest number of moments has aligned with the external field. This peak temperature is T_b. As temperature rises above T_b, thermal energy is strong enough to overcome the Zeeman energy, and thus randomize the moments, resulting in a decrease of total moment. A FC magnetization vs. temperature curve is obtained with the same small applied field while temperature drops. The FC curve will diverge from the ZFC curve at temperatures lower than the blocking temperature. This divergence occurs because during field cooling the spins from each particle will tend to align with the easy crystalline axis that is closest to the applied field direction, and remain frozen in that direction at low temperature. Thus the divergence of the ZFC-FC curves indicates that single domain particles dominate the magnetic signal.

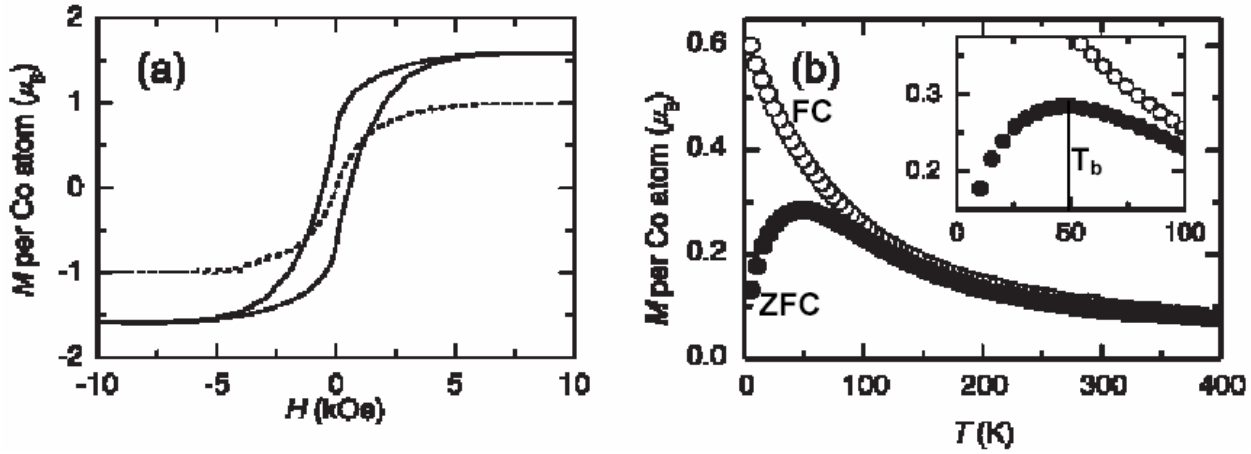

Figure 2.13 Cobalt magnetic nanoparticles can be detected by means of ZFC-FC magnetic measurement. a) Hysteresis loops at 5K and 300K show drastically decreasing H_c to almost zero as temperature is increased. b) ZFC-FC curves show substantial divergence at low temperatures; and T_b is observed in the ZFC curve, as measured in 100Oe (after Ref. 36).

For a TiO_2: Co film, the observation of T_b indicates the presence of superparamagnetic cobalt particles; in other words, cobalt metal clusters. Figure 2.13 is an example of the ZFC-FC curves with nanometer scale Co clustering in Co ion implanted epitaxial TiO_2

films [36]. In a), the film exhibits a ferromagnetic-like hysteretic behavior at low temperatures; at elevated temperatures the film shows paramagnetic-like behavior. In b) The ZFC-FC curves show features of superparamagnetic behavior with the observation of $T_b \sim 80K$. Both behaviors are not expected for a ferromagnet and suggest the presence of nanoparticles [36]. Estimates of Co precipitatie size are around 4nm, which is consistent with the metallic cobalt observed in TEM images [18].

Intrinsic Ferromagnetism In case of ferromagnetic DMS, RTFM is expected to originate from intrinsic effects. According to Spaldin, et al. [43], the most commonly used models to describe the magnetic interactions in DMSs are: a) direct and superexchange in insulators; b) carrier-mediated exchange; and c) bound magnetic polarons. Conventional DMS display RTFM originating from exchange interactions due to intrinsic effects and mediated by carriers. In this situation free carriers mediate the exchange interactions among localized magnetic moments. One type of this kind of interaction is called the Ruderman-Kittel-Kasuya-Yosida (RKKY) interaction, which describes magnetic exchange between individual localized magnetic moments and free electron charge [43]. Zener carrier-mediated exchange happens in a system where itinerant carriers mediate a ferromagnetic interaction between local moments [43]. Zener double-exchange was initially suggested to describe the oxygen atom mediated indirect ferromagnetic exchange between neighboring Manganese ions. It is different from superexchange because of the involvement of the carriers [43].

Since they are believed to be carrier mediated, the conventional DMS or DMO should have magnetic properties which depend on Co content and carrier concentration. For example T_c is expected to change systematically with oxygen growth pressure, since the oxygen deficiencies are usually expected to provide charge carriers. There are systematic studies on the effect of various cobalt concentrations, as reviewed in section 2.2.2.3. Section 2.2.6 summarizes a study of the effect of oxygen growth pressure and the concomitant carrier concentration on magnetism.

Other evidence of intrinsic FM is the observation of regular magnetic domain patterns at submicrometer scales. From the theoretical point of view, the existence of domains can

contribute to minimize the total free energy and to achieve a stable equilibrium state of a specimen's magnetization [100]. Such domain structure is observed in cobalt doped TiO_2 by some authors [12]. Figure 2.14 shows an example of magnetic domain observation, which suggests long-range ordering of magnetic moments induced by cobalt doping. Magnetic domains are not observed in TiO_2 without cobalt doping, indicating that the long-range ordering of magnetic moments is induced by cobalt doping. This is consistent with TEM where no evidence of cobalt clustering is observed [12].

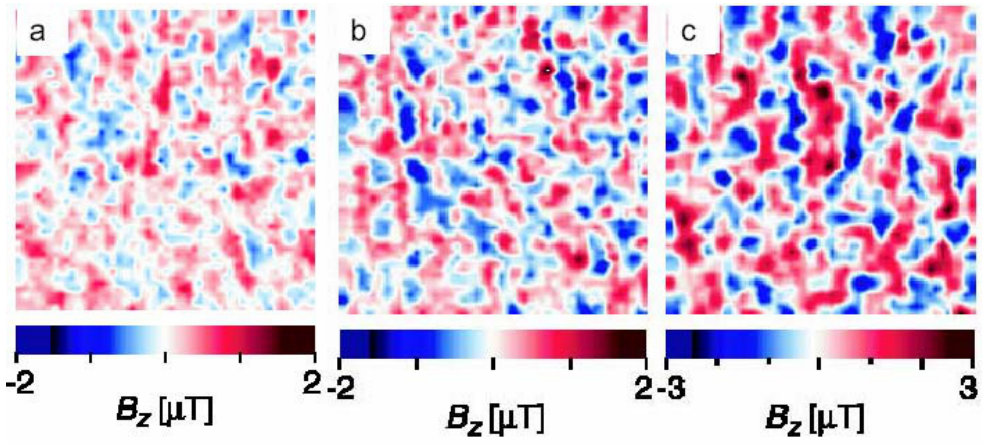

Figure 2.14 The observation of magnetic domain structures in TiO_2: Co thin films with different Co content. a) x= 0.02, b) x=0.03, c) x=0.06. The data are taken by scanning SQUID microscope images taken at 3K. The systematic increase in magnetic field results from the increased spontaneous magnetization. The images are 200μm * 200μm (after Ref. 12).

In magnetic measurement with a magnetometer, in many cases the substrate contributes most of the resulting signal. This is particularly true for thin films. With performance of magneto-optical spectroscopy such as magnetic circular dichroism (MCD), the signal from the substrate is negligible in the overall results. In contrast to magnetometer measurements where the magnetization represents the response of static spins; MCD measures the difference of absorption of the left and right circular dichroism as a ferromagnetic response of the photoexcited carriers. In situations where the carriers mediate the exchange interaction between localized spins, the MCD signal is generally enhanced at the absorption edge of the host material, such as TiO_2. This effect exists not only in DMOs. As seen in figure 2.15 a) and b), the MCD signal changes sign from negative to positive with photon energy, and there is a peak at

3.57eV, near the band gap of TiO_2. This feature is different from that in cobalt metal. Thus the possibility of bulk precipitation of Co metal is excluded. In c) and d), for $x = 0.03$-0.10, the steep increase at low magnetic field and the saturation at high magnetic field shows clear ferromagnetic behavior. The hysteresis is not clear in this figure due to the large magnetic field scale. There is also systematic change as a function of cobalt content, with the MCD signal appearing at x=0.03 and increasing with higher x [42].

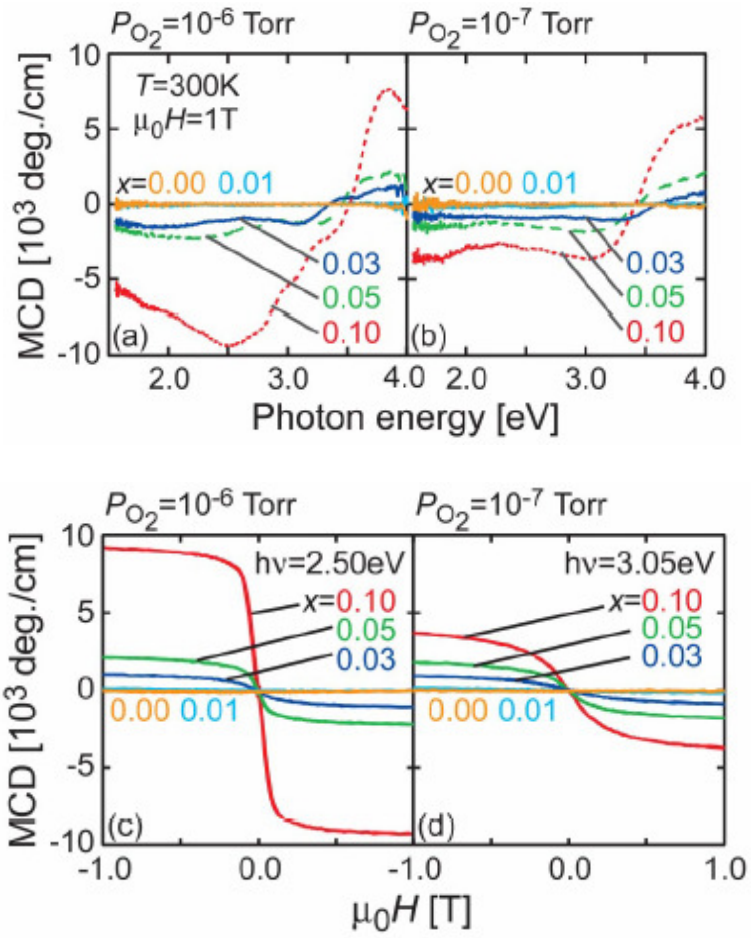

Figure 2.15 MCD spectra dependence on photon energy and applied magnetic field. The films are $Ti_{1-x}Co_xO_{2-\delta}$. a) and c) are for films with $PO_2 = 10^{-6} Torr$. b) and d) are for films with $PO_2 = 10^{-7} Torr$ (after Ref. 42).

Other than the magnetically observed intrinsic FM, an anomalous Hall Effect (AHE) or hysterestic magnetoresistance are generally also expected to be a signature of intrinsic DMS [42]. However there is an important exception in which AHE and Co particles were

observed simultaneously [27]. I will address this anomaly in the review of transport and magneto-transport properties.

2.2.5 Transport and magneto-transport properties

Transport and magneto-transport properties can provide important electrical information such as the material type (insulator, semiconductor or metal, etc), charge carrier type, and carrier concentration. The resistivity vs. temperature will reveal the physical mechanism of transport. Hall measurements and magnetoresistance measurements are often important in providing supporting evidence for magnetic observations. As can be seen from Tables 2.2-2.6, most of the reports on cobalt doped TiO_2 are focused on the fabrication, structural analysis and the occurrence or absence of room temperature ferromagnetism. The reported transport and magnetotransport behavior of cobalt doped TiO_2 materials is summarized in table 2.6.

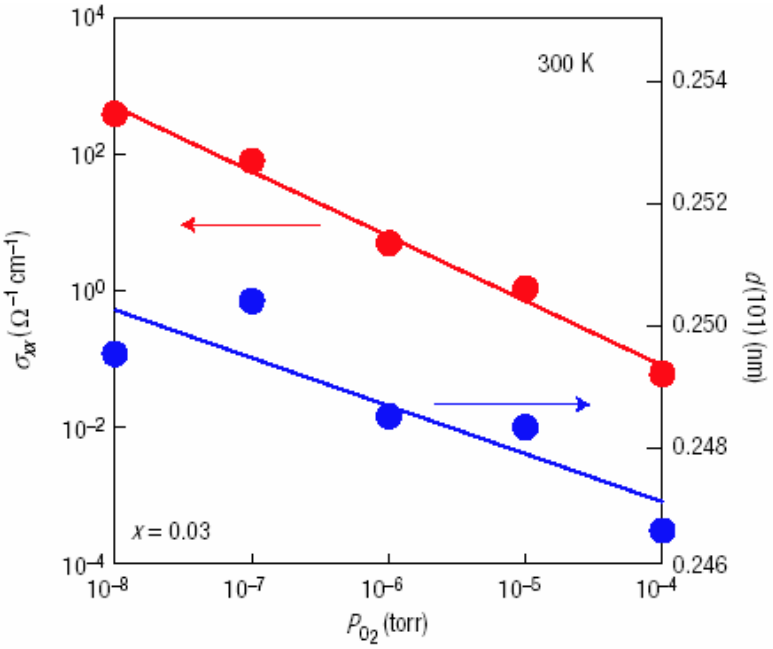

Figure2.16 PO_2 dependence of conductivity and lattice constant at room temperature (from Ref. 30).

Most of the reported resistivity values at room temperature for the cobalt doped TiO_2 are in the range of 10~1000 mΩ-cm ([12], [16], [35], [44]). Together with a few reports of more insulating ([30], [46]) and more metallic behavior [24], literature indicates that most

of the films have resistivity in the semiconductor range. The more conducting rutile samples are grown in lower partial oxygen growth pressure (PO_2). The reason is that lower PO_2 induces more oxygen vacancies, which supposedly form shallow donors, and thus provide more charge carriers. As demonstrated in figure 2.16, with decreasing PO_2, the carrier concentration and thus the conductivity, σ_{xx}, increase systematically ([30]).

For conventional DMS, the temperature dependence of the resistivity indicates semiconducting behavior ([16], [30], [31], [42]). For example in figure 2.17, for undoped anatase TiO_2, the temperature dependent resistivity has an upturn at a few K, which is because of the aforementioned oxygen vacancies, whereby states are introduced just below the conduction band and are depopulated at only a few K [16]. For cobalt doped anatase TiO_2, the resistivity is dramatically increased although the carrier concentration, $2.1*10^{18}cm^{-3}$, is similar to that of pure anatase, $1.4*10^{18}cm^{-3}$. This indicates a dramatic drop in mobility in the doped films. It has been suggested that the mobility drop is due to magnetic scattering or strain scattering effects, resulting from the incorporation of cobalt [16].

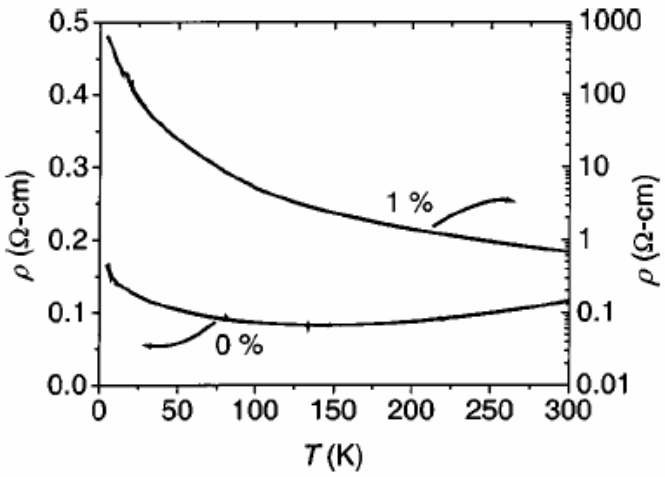

Figure 2.17 Temperature dependence of resistivity of an undoped anatase TiO_2 and $Ti_{0.99}Co_{0.01}O_{2-\delta}$ films (after Ref. 16).

Other than semiconducting films, there are also reports on metallic and insulating films. For example, all of the three kinds of temperature dependent resistivity are observed in cobalt doped anatase films on LaSrAlO4 (LSAO) fabricated by PLD [31]. Depending on

substrate temperature (600°C, 700°C or 850°C), the crystallinity differs for each case with various amount of defects resulting in metallic, semiconducting, and insulating ρ vs. T curves, respectively (see figure 2.18)[31].

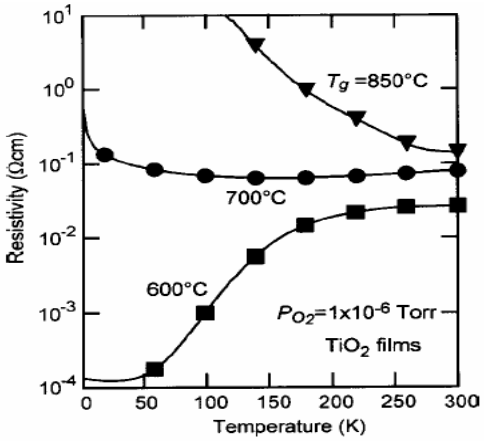

Figure 2.18 Temperature dependence of the resistivity for undoped anatase TiO_2 with various substrate temperatures during PLD (after Ref. 31).

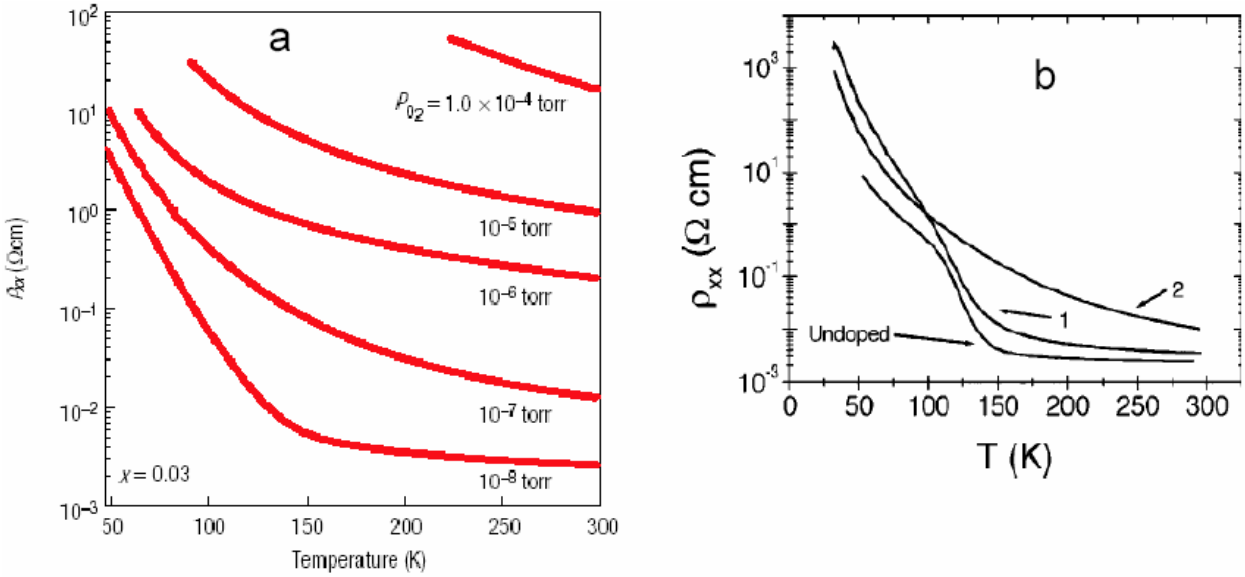

Figure 2.19 Elbow observation in ρ vs. T curve for highly reduced TiO_2 doped with Co. a) resistivity as a function of temperature for $Ti_{0.97}Co_{0.03}O_{2-\delta}$ under various PO_2 prepared by laser MBE. There is a clear elbow behavior in the ρ vs. T curve for the sample grown under $PO_2 = 10^{-8} Torr$ (after Ref. 30). b) Resistivity as a function of temperature for samples grown by PLD. Sample 1 is grown under vacuum at a base pressure of 2*10^{-8} Torr and sample 2 is deposited under a 5%H_2-Ar mixture at 1mTorr. Both samples 1 and sample 2 have Co content of $x = 0.02$. The "undoped" sample is a pure TiO_2 film deposited at the same growth condition as sample 1 (after Ref. 24).

When grown at extremely low PO_2 or under vacuum, the large oxygen vacancies will initiate a temperature induced metal-insulator transition, and an elbow in ρ vs. T with an

observed “transition” temperature of ~140K ([24], [30]). Examples are shown in figure 2.19. Figure a) exhibits a series of ρ vs. T curves for samples prepared under various PO_2. It is clear that there is an elbow at ~140K for sample with the lowest PO_2 of 10^{-8} Torr. The relationship to a large number of oxygen vacancies is clear. In figure b) the undoped TiO_2 films grown under vacuum show similar behavior to the cobalt doped film. This indicates that it is the oxygen vacancies rather the magnetic impurities that dominate this abnormal resistivity behavior [24]. Furthermore it is claimed that this resistivity behavior matches that of the Magnéli phase Ti_nO_{2n-1}, a form of reduced rutile [24]. A similar elbow in ρ vs. T has also been observed in Fe doped TiO_2. This provides further evidence that it is the reduced TiO_2 rather than transition metal dopants that dominate the resistivity [47].

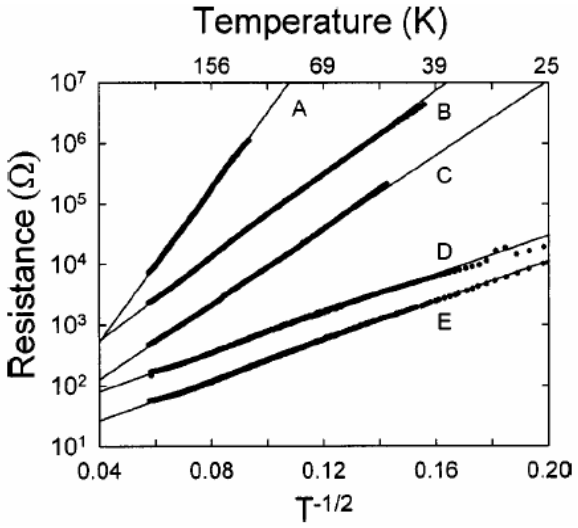

Figure 2.20 A hopping conduction mechanism is observed in cobalt doped rutile and anatase films, which were later on determined to be a multiphase system of cobalt nanoclusters plus the TiO_2 dielectric lattice (after Ref. 35).

A hopping conduction, $\ln\rho \propto T^{-1/2}$, relationship between resistivity and temperature in both rutile and anatase films doped with cobalt was reported by us earlier [35]. The resistivity as a function of temperature is demonstrated in figure 2.20. In the figure, rutile samples A, B and C are grown at $PO_2 = 1mTorr$, $PO_2 = 0.2mTorr$ and $PO_2 = 0.05mTorr$, respectively. Sample D and E are anatase films grown at $PO_2 = 1mTorr$. Curves D and E have been scaled down by a factor of 1000 for clarity. This hopping conduction has

been observed in a group of laser ablated cobalt doped rutile and anatase TiO_2, but not in pure TiO_2. This $T^{-1/2}$ transport is characteristic of hopping transport in a multiphase system of metallic grains embedded in dielectric matrix. In the case of TiO2: Co, the hopping transport happens when the thermal activated charge moves from charged cobalt clusters to uncharged cobalt clusters. The existence of cobalt clustering is confirmed by TEM observation [35]. According to this mechanism, the Co clustering contributes more than the oxygen vacancies to the transport. This work suggests the transport characterization as another way to identify the presence of cobalt clusters [35].

Hall and magnetoresistance (MR) measurements are generally performed to explore the electromagnetic properties. From Hall measurement on iterant or band like charge carriers, one can derive the carrier type and concentration. With systematic measurements of Hall Effect and magnetism, one may be able to relate carrier concentration to the ferromagnetism. Furthermore an observation of room temperature AHE could be a signature of intrinsic RTFM. 10^{18} or 10^{19} cm^{-3} is typically observed as the value of carrier concentration in cobalt doped TiO_2, as summarized in table 2.6.

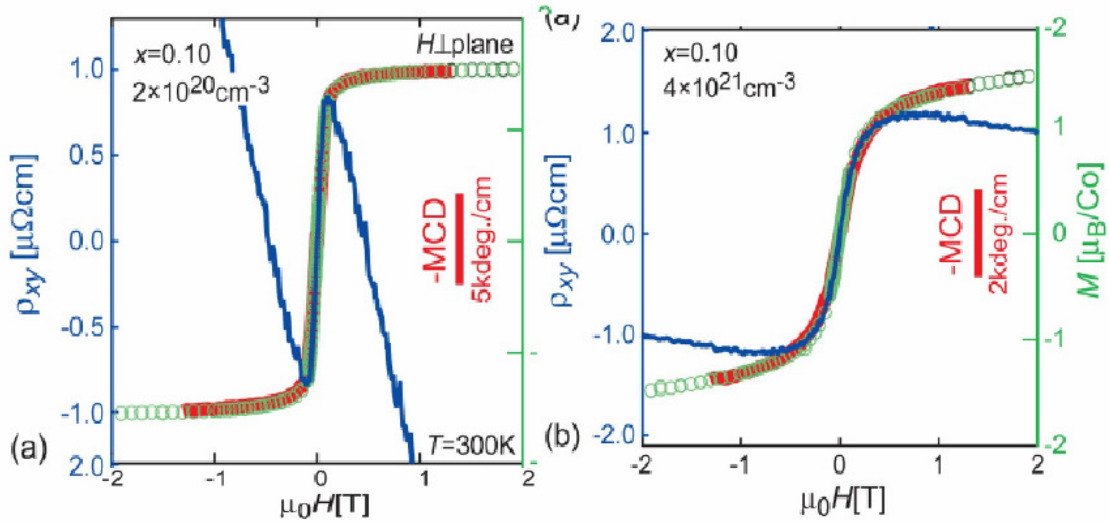

Figure 2.21 Magnetic field dependence of MCD (red curve), magnetization (green symbol) and Hall resistivity (blue curve). Both figures are for samples with x=0.10. The carrier concentrations are $2*10^{20}cm^{-3}$ and $4*10^{21}$cm for a) and b), respectively (after Ref. 42).

In 2001, Matsumoto et al. reported a carrier concentration of 10^{18} cm^{-3}, which is scarcely dependent on Co doping level [12]. AHE has been reported by Yamada et al.

on relatively conducting samples ([30], [31] and [42]). They demonstrated the coincidence of magnetization, MCD and Hall measurements, as shown in figure 2.21. The deviation of the Hall resistivity at higher magnetic filed is due to the ordinary Hall Effect. This coincidence suggests an intrinsic ferromagnetism with a single cause, which cannot be Co clusters since the concentration is much below the percolation limit [42].

AHE alone cannot be the signature of intrinsic ferromagnetism. Shinde et al. [16] also observed similar carrier concentration; they also claimed that the n- type carriers are due to the oxygen vacancies which behave as shallow donors. In a later work Shinde et al. fabricated highly oxygen deficient cobalt doped anatase films with carrier concentrations of 0.8-3 $*10^{22}$ cm^{-3} and resistivities of 5-10mΩcm. They observed the AHE at 300K and 200K with the magnetic saturation field (0.1T) coinciding well with the AHE data, which suggested a possible intrinsic RTFM [24]. However, a recent work from the same group reported an observation of ~10nm Co clusters at the interface of the substrate with the conductive film [27]. Thus when cobalt nanoparticles and superparamagnetism are observed in the highly reduced Co doped rutile films, it is not sufficient to determine the intrinsic nature of DMS only from the observation of AHE, without a detailed microscopic characterization of the samples.

Applying an external magnetic field will sometimes change the resistance of some materials. This property is the magnetoresistance (MR), which is often expressed as a resistance change $[R(H)-R(0)/R(0)]$, where R(H) and R(0) are values of the resistance with and without an applied magnetic field. MR measurements, together with magnetic, transport and Hall measurements, are often performed to attempt to clarify the physics of microscopic mechanisms for transport in cobalt doped TiO_2. Three types of MR have been reported: small negative (-0.4%) MR at higher temperatures [30], small positive (0.2%) MR down to very low temperature [46] and apparently positive MR at low temperatures ([12], [16]).

The small negative MR ~0.4% has been reported by Toyosaki et al. at temperatures >100K [30]. The absolute value of the MR increases monotonically with increasing applied field and at lower temperature. For samples grown at various PO_2 and thus with

various carrier concentrations, there is no significant difference in MR, as shown in figure 2.22. Along with this negative MR, a scaling relationship $\sigma_{AHE} \propto \sigma_{xx}^{\alpha}$ with α~1.5-1.7 was observed in the Hall Effect, which is independent of cobalt concentration, temperature, and oxygen deficiency. From these results the authors concluded that the scattering by phonons, magnetic impurities and non-magnetic impurities (oxygen deficiency) does not affect the charge-carrier dynamics in the AHE very much. The authors also suggested that the ferromagnetically spin-polarized charge carriers play a significant role. However there was no further discussion of the underlying physical dynamics of the emergence of AHE, RTFM and negative MR [30].

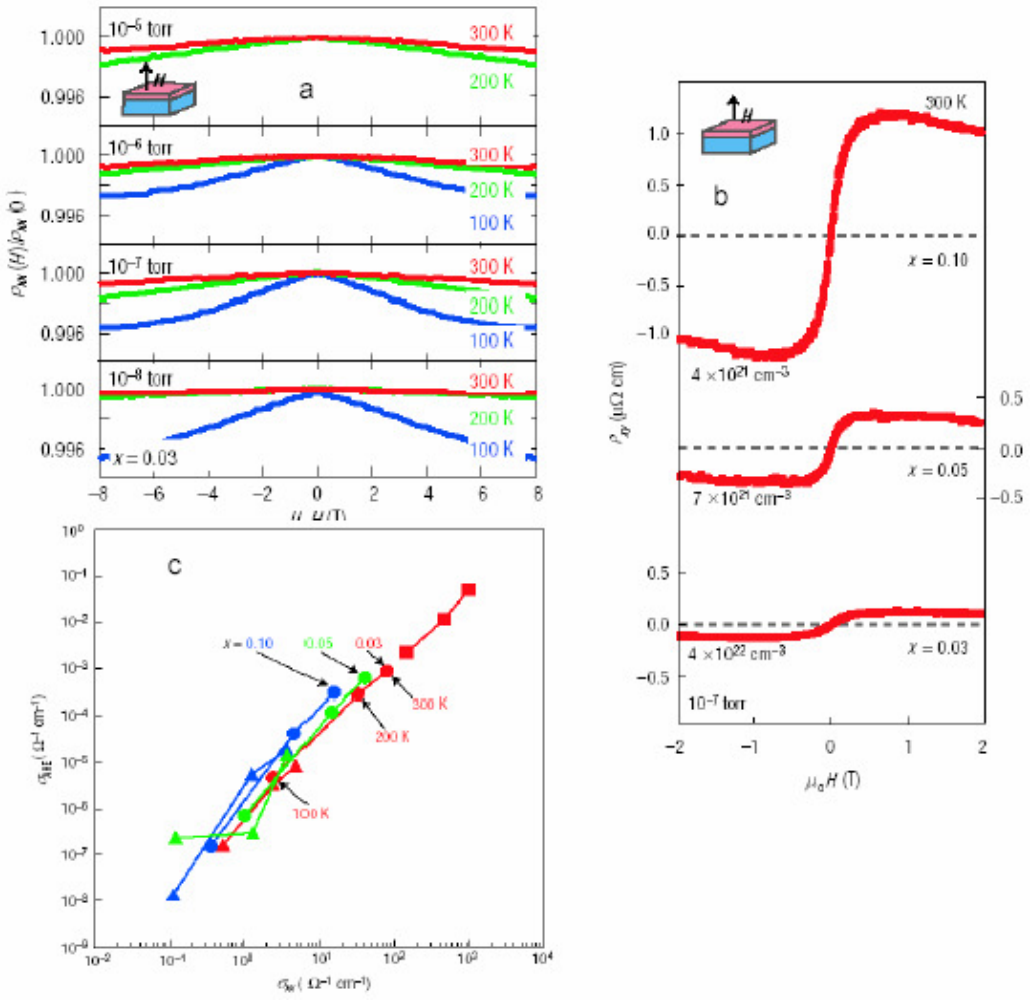

Figure 2.22 Observation of negative MR and scaling law of AHE. a) MR at various temperatures for samples grown with various PO_2. b) AHE at 300K for samples with various Co and carrier concentration. c) Observation of $\sigma_{AHE} \propto \sigma_{xx}^{\alpha}$ with α~1.5-1.7 for several orders of conductivity (after Ref. 30).

Han et al. also reported the electromagnetic properties of their sputtered Co doped anatase films [46]. According to their work, the MR is ~0.2% down to 2K. There is no observation of extraordinary Hall Effect, either, and the observed RTFM is attributed to the Co clusters. In this work it is suggested that the Co-doped TiO_2 is not an intrinsic magnetic semiconductor.

Other than negative or no clear MR effect, large positive MR has been observed at very low temperatures by several groups. When Matsumoto et al. announced the first observation of RTFM in transparent Co-doped anatase thin films, they also reported a representative MR for the films, as demonstrated in figure 2.23 a). Here the ferromagnetic $Ti_{1-x}Co_xO_2$ with x=0.07 exhibits a large positive MR of 60% at 2K in an applied field of 8T. With increasing temperature the MR effect decreases, and at 5K the MR is close to zero. Clear long range ordering of magnetic moments was confirmed by the systematic observation of magnetic domain structures on samples with various x. The underlying microscopic mechanism of the long range order was left as an open question in this article [12].

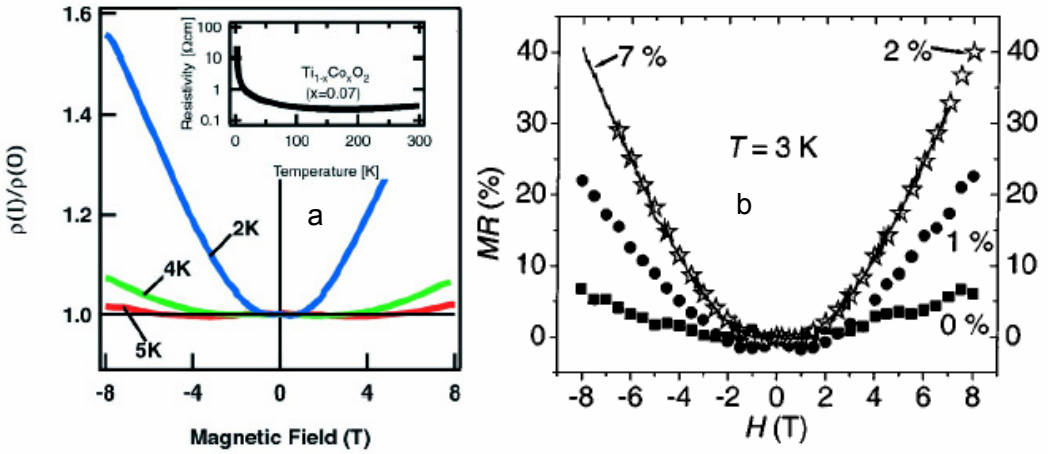

Figure 2.23 Observation of large positive MR at low temperatures. a) A positive 60% is observed for 7% Co doped anatase on LAO (after Ref 12). b) MR at 3K for TiO_2 and various Co contents (after Ref. 16).

Shinde et al. proposed the combined role of magnetic Co ions and a defect state (oxygen vacancy) as controlling the physics of MR properties [16]. As demonstrated in figure 2.23 b), the MR is approximately quadratic and only significant at 3K. At this

temperature, the value of MR in a field of 8T is only 6% for undoped TiO_2, 23% for x=0.01, and 40% for x=2%. For higher Co concentration the MR also shows saturation, which is due to clustering of excess Co. Referring to the curves of ρ vs. T in figure 2.17, the oxygen vacancies are shallow donors which cause the upturn of ρ at low temperatures, and the Co atoms contribute to lower mobility due to scattering. Thus based on the understanding that oxygen vacancy related states lie close to the bottom of the conduction band, the observed MR behavior is understandable. The coupling between the Co ion spin and the states related to oxygen vacancy will experience a Zeeman splitting in the presence of magnetic field. Since the lower split band will be occupied, the MR should be positive [16].

2.2.6 Co Clustering, Oxygen Ambient and Defects

As mentioned earlier, whether the ferromagnetic Co doped TiO_2 is a true DMS depends on the presence of Co clustering or Co-rich regions. Jaffe et al. presented a computational study of Co doped TiO_2 [47]. Their total energy calculations show a strong tendency for Co-atom clustering or segregation on Ti sites. There is also a strong tendency for the oxygen vacancies to form complexes with the Co clusters [48]. Experimentally, the clustering in Co doped TiO_2 films is closely related to the Co diffusion in the materials during film fabrication. This is particularly true for the case of anatase films. As discussed earlier, anatase can be obtained in the form of thin films on lattice matched substrates. Since anatase is not thermodynamically stable, however, it is easy to form defects with slight changes in growth conditions.

One way to study the oxygen effect on clustering is to grow films under different PO_2 and to investigate the microstructures. Kim et al. [18] grew anatase $Ti_{0.96}Co_{0.04}O_2$ by PLD at different PO_2 and found that with $PO_2 \geq 10^{-5} Torr$, no Co clustering was observed with a 2D layer by layer growth on a very smooth surface; while with lower PO_2, 3D island like growth was observed by spotty RHEED patterns, which was confirmed to be cobalt clustering with Cross-Sectional Transmission Electron Microscopy (XTEM) patterns. As demonstrated in figure 2.24, cobalt clustering occurs at the interface of the

substrate and film for $PO_2 = 10^{-7} Torr$. For $PO_2 = 10^{-5} Torr$, no cobalt clustering was observed. The explanation is the following. From the viewpoint of thermodynamics, Co oxide is less stable than TiO_2 at low PO_2 [18]. Thus Co ions are less likely to form anything other than cobalt metal clusters. Furthermore, at low PO_2, oxygen vacancies are easily formed, which can help the diffusion of cobalt atoms to form Co clusters. This is also confirmed by the trend in saturation magnetization variation with PO_2, where the low oxygen growth pressure yields films having magnetization close to cobalt metal. This also can be seen in figure 2.24 (e). In the same figure, the M vs. T curve for a sample with $PO_2 = 10^{-7} Torr$ is flatter than the one with $PO_2 = 10^{-5} Torr$, indicating that the former sample has T_c closer to that of Co metal of 1404K. Furthermore, the higher magnetization than 1.7μ_B/Co might come from the formation of Co intermetallic compounds [18], or just from uncertainty in the cobalt concentration.

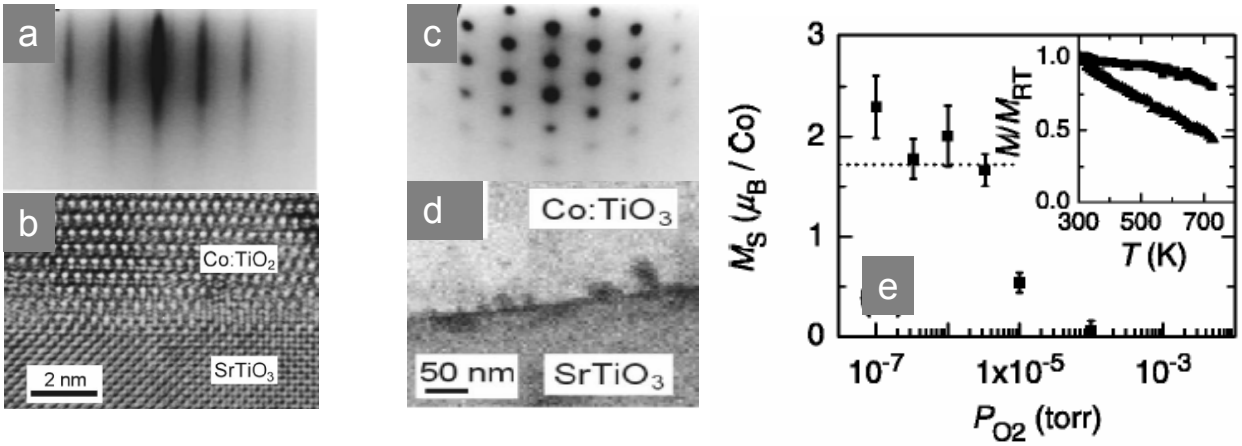

Figure 2.24 PO_2 effects on Co clustering during growth of anatase $Ti_{0.96}Co_{0.04}O_2$. Streaky RHEED pattern (a) and no sign of Co clustering (b) correspond to $PO_2 = 10^{-5} Torr$; Spotty RHEED pattern (c) and Co clustering formation (d) are for samples with $PO_2 = 10^{-7} Torr$. In e) the M_s increases with lower PO_2 because of Co metal clustering. The dotted line corresponds to the value of bulk cobalt value. The inset shows the M vs. T for sample with PO_2=10^{-7} (upper curve) as well as for PO_2=10^{-5} torr (lower curve), where the former shows a more flat curve indicating a T_c closer to 1404K (after Ref. 18).

Another method is to oxidize the as grown films under various PO_2. Kim et al. made two groups of Co doped anatase TiO_2. One was laser ablated and the other was prepared by ion-implantation, and then the films were annealed under precisely controlled PO_2 varying from 10^{-6}Torr to 10^{-1}Torr [29]. Their ion-implanted films showed superparamagnetic behavior, demonstrating Co clusters formation. Some of the laser

ablated samples were annealed just after growth. The laser ablated films are ferromagnetic at room temperature. The FM disappears after annealing at 900°C under abundant oxygen with $PO_2 = 10^{-1} Torr$ for 30min for samples from both groups. If the PO_2 during anneal is controlled to 10^{-6} Torr, large clusters are formed, with ~100nm size clusters on the surface of ion-implanted films and ~170nm clusters at the interface of samples prepared with PLD. These observations confirm the role of oxygen vacancies in facilitating the diffusion of Co atoms. The different regions where the Co formed during anneal indicate that cobalt tends to diffuse to regions of high density of defects, since the ion-implantation generates defects on the surface while for PLD samples the lattice mismatch between STO and TiO_2 creates defects [29].

Annealing in pure argon is analogous to annealing in vacuum. The as grown films of anatase $Ti_{0.93}Co_{0.07}O_{2-\delta}$ are ferromagnetic with Co clusters at the interface [16]. After measuring the as grown film in pure argon by VSM up to 1200K, namely continuously annealing the film in argon up to 1200K, it turns out the cobalt metal is still present as ferromagnetic metal with almost complete matrix incorporation [16]. This is confirmed since the room temperature magnetic moment remains unchanged but T_c varied from ~1180K before anneal to ~700K after anneal [16].

2.2.7 Other TM doped TiO_2

Other than Co, some other transition metals have also been doped into TiO_2 to fabricate DMS. As mentioned earlier, room temperature ferromagnetism is observed in Fe doped TiO_2 with high oxygen deficiency [48]. Recently N. H. Hong reported work on $Ti_{1-x}TM_xO_2$, where the TM are Sc with $x = 5\%$, V with $x = 5\%$, Cr with $x = 5\%$, Mn with $x = 5\%$, Fe with $x = 8\%$, Co with $x = 12\%$ and Ni with $x = 8\%$ [49]. The XRD patterns show that all the films are well oriented single anatase phase without impurity peaks, thus it is assumed that the transition metal dopants are well substituted for Ti in TiO_2 host matrix and a solid solution is achieved. All the films show room temperature ferromagnetism and the observed saturation moment is large with a maximum value of $4.2\mu_B$/ V for V doping. This is remarkable since V itself is not magnetic. Furthermore the observation of big domains of 5-10μm suggests the intrinsic origin of the RTFM.

2.3 Other Oxide based DMOs

2.3.1 ZnO Based Materials

2.3.1.1 Introduction

The stable crystal structure of ZnO is wurtzite where each zinc atom is surrounded by four atoms of oxygen in tetrahedral coordination. ZnO is attractive because it is potentially a multifunctional material. It is a wide band gap of 3.35eV oxide. It is also transparent. ZnO naturally has n-type conductivity; but it has also been reported that p-type ZnO can be obtained by codoping two dopants of Ga (donor) and N (acceptor) [49]; Phosphorus doping of (Zn, Mg)O also results in p-type carriers [81].

The starting point for ZnO as a possible DMS candidate came from the work on materials design by Sato and Katayama-Yoshida [50]. The authors demonstrated that doping 3d transition metal atoms, such as V, Cr, Fr, Co and Ni into a ZnO matrix can induce ferromagnetic order without introducing additional carriers by doping. Mn with additional hole doping can also result in ferromagnetism. There has been intense experimental work following the calculation.

2.3.1.2 Growth condition

As a potential host material for DMS, ZnO has been doped with various transition metals (TM), such as V ([53], [82]), Ni ([56]-[57], [76], [82]), Mn ([57], [59]-[64], [75], [77]-[81]), S ([58]), Co ([57], [66]-[75], [82]-[83]), Fe ([64]-[65], [74], [82]), Cr ([57], [64]); it was also studied when doped with non transition metal Mg ([54], [55], [81]). Similar to TM doped TiO_2 films, the studied TM: ZnO films are preferably deposited by the PLD technique ([53], [56]-[59], [60], [62], [66]-[70], [72], [75], [79]-[81]) with minor exceptions of MOCVD ([54]-[55]), sputtering ([60], [71], [74]), MBE ([63]-[64]), solid state reaction ([65]), and so-gel methods ([73]). Ni-ZnO powder has also been fabricated by co-precipitation and ceramic methods [76]. Nanostructures of Mn-ZnO were also fabricated by chemical vapor deposition [77]. Furthermore Mn ions were implanted into Sn-doped

ZnO single crystal. The most prevalent substrate to deposit ZnO based films is c-sapphire due to the low lattice mismatch of 2% between the film and the substrate. For film growth on r-sapphire, Muthukumar et al. noticed that a buffer layer of at least 50Å ZnO is necessary to achieve the wurtzite crystal structure [54].

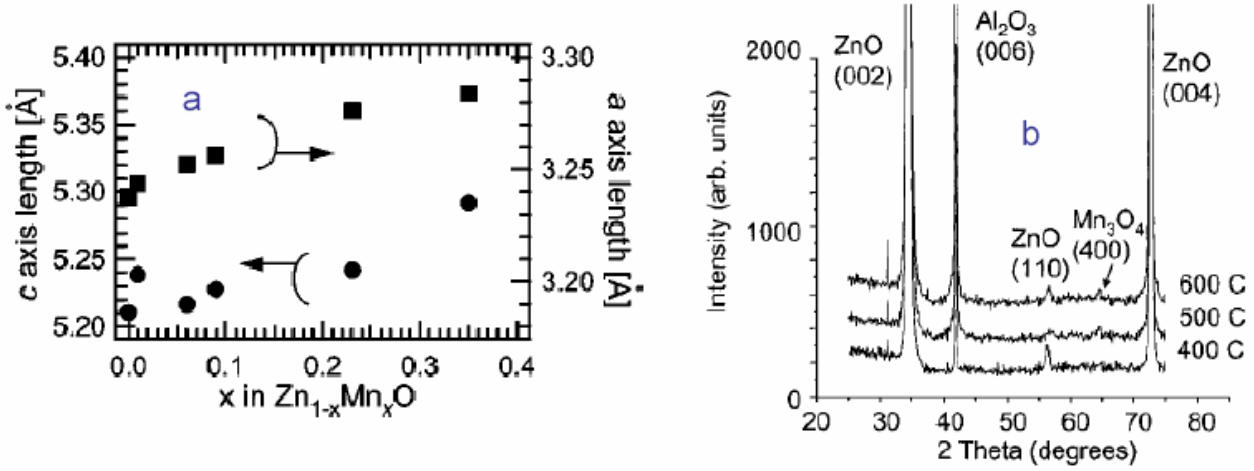

Figure 2.25 Mn solubility in laser ablated $Zn_{1-x}Mn_xO$ films. a) Mn content dependence of a- and c- lattice constants for $Zn_{1-x}Mn_xO$ films suggests a wurtzite $Zn_{1-x}Mn_xO$ can be achieved with x up to 35% (after Ref. 59). b) XRD pattern indicates the precipitation of Mn_3O_4 in $Zn_{1-x}Mn_xO$ films deposited from a target containing 3% Mn and 0.01% Sn (after Ref. 80).

Generally the limit of transition metal solubility in ZnO is much bigger than that of Co in TiO_2. Within the solubility limit, Vegard's law is frequently observed. It indicates that the dopants ions are systematically substituted for the Zn ions without changing the wurtzite ZnO structure. The solubility of the dopants varies depending on growth method and the tuning of fabrication parameters. Unlike the situation of cobalt doped TiO_2, much higher incorporation limits of magnetic dopants in ZnO have been reported by various groups. For Mg dopant, the solubility can reach 33% [54]. Ni can incorporate into the wurtzite matrix with a solubility of 25% [56]. The highest limit of ~35% for Mn dissolved into ZnO is reported by Fukumura et al. [59] with PLD deposition at $5x10^{-5}$mTorr PO_2. However a recent report by Ivill et al. noted that a Mn oxide phase will be present when the Mn concentration exceeds 3 at% in the PLD fabricated films at a much higher PO_2 of 20mTorr [80]. The authors claimed that the very different PO_2 might determine the Mn solubility [80]. Figure 2.25 shows evidence of the two very different results. There is more controversy on the solubility of Co into ZnO. Prellier et al. observed a plateau in

lattice constant with concentration above 10%, which indicates the limit of solid solubility is ~10% [64]; Lee et al. claimed that the limit is lower than 25% [73]; and Ueda et al. observed phase separation into CoO and ZnO with target containing 50% Co, which indicates a limit of <50% [57]. The resulting film homogeneity is affected by the growth conditions. For instance, for $Zn_{0.75}Co_{0.25}O$ films on c-sapphire substrate fabricated by PLD, a paramagnetic homogeneous alloy with wurtzite structure can be achieved at substrate temperatures lower than 600°C; with substrate temperature higher than 600°C and PO_2 lower than 10^{-5} Torr, Co clusters will be formed during growth; with substrate temperature of 600°C and $PO_2 = 10^{-5} Torr$ the best quality film can be fabricated with x=25% and the solubility will reach 40% [72].

2.3.1.3 Properties

Magnetic properties We are interested in understanding the dominant physical mechanism for the RTFM. Many magnetic properties of the transition metal doped ZnO have been obtained by various research teams. However many of the results are not very reproducible. Ueda et al. [57] observed RTFM in $Zn_{0.85}Co_{0.15}O$ with PLD fabrication with a saturation magnetization $1.8\mu_B$/Co. 1wt% of Al was added to the target to provide electronic dopants. In their films, T_c and M_s increased with carrier concentration, and RTFM is observed only in films with carrier concentration as high as $10^{20}cm^{-3}$ [57]. They suggested a carrier mediated mechanism, either RKKY or double exchange, is the origin for RTFM: cobalt metal was excluded as an origin for RTFM because the lattice constant systematically increased with the Co content, indicating Co substituted in Zn sites; CoO was excluded as an origin of RTFM because it was not observed in the XRD patterns, and the resulted magnetic moment exceeds that of the weak ferromagnetism of CoO. However the reproducibility of ferromagnetic $Zn_{1-x}Co_xO$ thin films is as poor as 10% from the same group [57].

Prellier et al. used alternate deposition from Zn and Co targets by PLD under 0.1Torr pure oxygen. A $T_c \sim 300K$ is observed with $M_s = 0.7\mu_B / Co$ in $Zn_{0.95}Co_{0.05}O$. No further transport properties were reported in these highly crystalline films [66]. Other magnetic properties have also been reported. Rode et al. reported RTFM and strong out of plane

anisotropy in $Zn_{0.75}Co_{0.25}O$, and claimed that the RTFM is at least partly due to intrinsic properties of $Zn_{0.75}Co_{0.25}O$ and does not result from segregation effects [67]. Lim et al. concluded that RTFM in $Zn_{1-x}Co_xO$ ($x > 20\%$) results from the substitution of Co^{2+} for Zn^{2+}, with more activated sp-d interactions and d-d transitions at a higher cobalt conentration [71]. Ferromagnetism in $Zn_{1-x}Co_xO$ at 350K with x from 5% to 25% was also reported, where the authors claimed that the high temperature ferromagnetism is caused by ferromagnetic spin-spin interactions between cobalt atoms [73]. A recent remarkable report is the observation of a giant magnetic moment in insulating $Zn_{0.96}Co_{0.04}O$ with $M_s = 6.1\mu_B / Co$ and $T_c = 790K$ [76]. A supercoupling mechanism in terms of bound magnetic polarons rather than carrier mediated interaction is proposed to discuss the ferromagnetism and the giant magnetic moment as well as the high Curie temperature [76]

One observation of RTFM is shown in figure 2.26 [71], where clear ferromagnetic M vs. H loops at room temperature can be seen for films with $x > 20\%$ and the saturation magnetization, M_s, increased from 1.47 to 2.25 emu/cm^3 with increasing Co content [71].

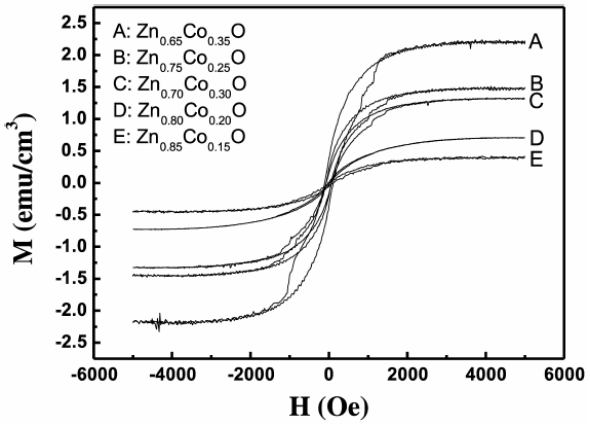

Figure 2.26 M vs. H curves for a series of $Zn_{1-x}Co_xO$. These curves are measured at room temperature (after Ref. 71).

In addition, the UF group has reported a series of detailed measurements on Mn doped ZnO ([78]-[81]). An early report showed a $T_c = 250K$ in Mn ion implanted Sn-doped n-type single crystal where the decreasing of M_s and H_c with increasing Mn concentration excludes the magnetic contribution from precipitating secondary phase such as Mn_3O_4

[78]. In a later work, RTFM was observed when Mn ion-implanted into laser ablated n-type phosphorus doped-ZnO thin films (which were initially annealed at various temperatures to achieve various carrier concentrations) followed by postannealing at 600°C; the resulting saturation magnetization is a strong function of initial annealing temperature whereby a lowest n-type carrier concentration results in maximum M_s. The authors suggested that hole doping stabilizes the FM state in Mn doped ZnO [79]. Recent work from the same research group ([80]-[81]) reported an inverse correlation of M_s with the n-type carrier concentration (see figure 2.27) and suggested a bound magnetic polaron model to understand the RTFM in (Mn, Sn) doped ZnO, where holes that are localized near the Mn ions are responsible for mediating ferromagnetism [80]; the authors also suggested that a low Mn concentration should be maintained to avoid Mn-Mn antiferromagnetic interactions, which are likely to dominate high Mn-doped ZnO films [80].

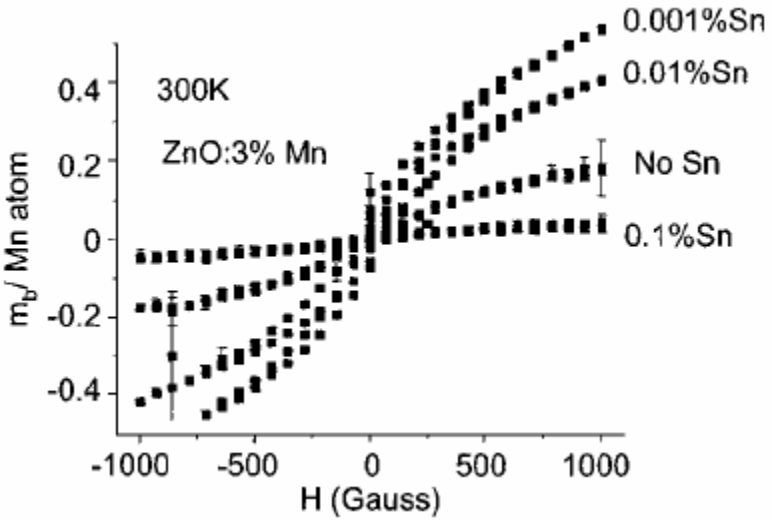

Figure 2.27 Ms monotonically decreases with increasing Sn concentration. Sn-doping will introduce n-type carriers (after Ref. 80).

Rapid thermal annealing in vacuum can greatly enhance the ferromagnetism in $Zn_{1-x}(Co_{0.5}Fe_{0.5})_xO$ thin films. Cho et al. sputtered the films with a substrate temperature of 600°C and annealed the as deposited films at 600°C in a vacuum of 10^{-5} Torr for 10min [74]. A significant increase in T_c and magnetic moment was observed, as demonstrated in figure 2.28. It is clear that rapid thermal annealing leads to a

remarkable enhancement in the saturation magnetization at 4K: M_s at 4K was increased from $M_s = 5.4 emu/cm^3$ for as deposited film to $M_s = 15.2 emu/cm^3$ for annealed films. In addition, the RTFM is also enhanced by annealing, as seen in figure 2.25 b), there is hysteretic M vs. H for the as deposited film with $H_c = 250 Oe$ and $M_s = 1.2 emu/cm^3$, and annealing increased both values, resulting in $H_c = 270 Oe$ and $M_s = 12.4 emu/cm^3$ for annealed samples [74].

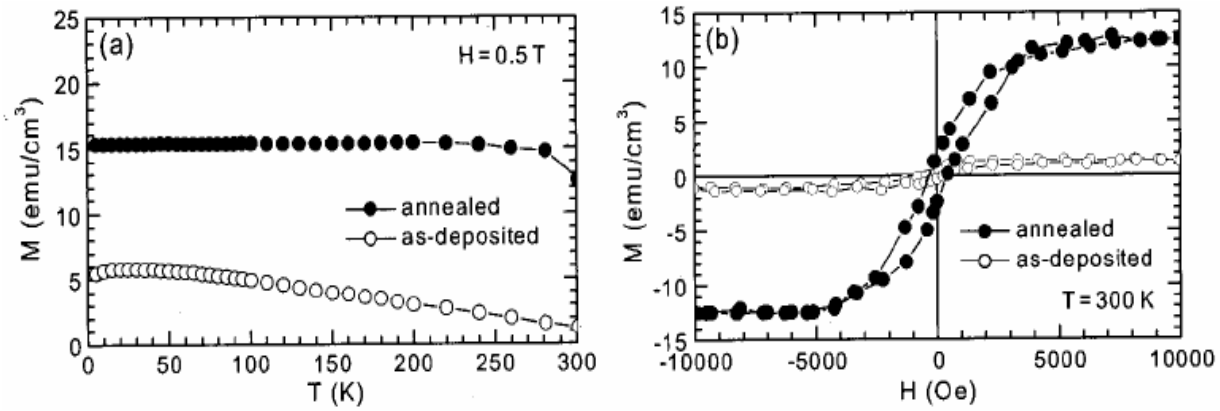

Figure 2.28 Effect of annealing in ferromagnetism of $Zn_{0.85}(Co_{0.5}Fe_{0.5})_{0.15}O$. a) M vs. T in a field of 0.5T. b) M vs. H curves at 300K (after Ref. 74).

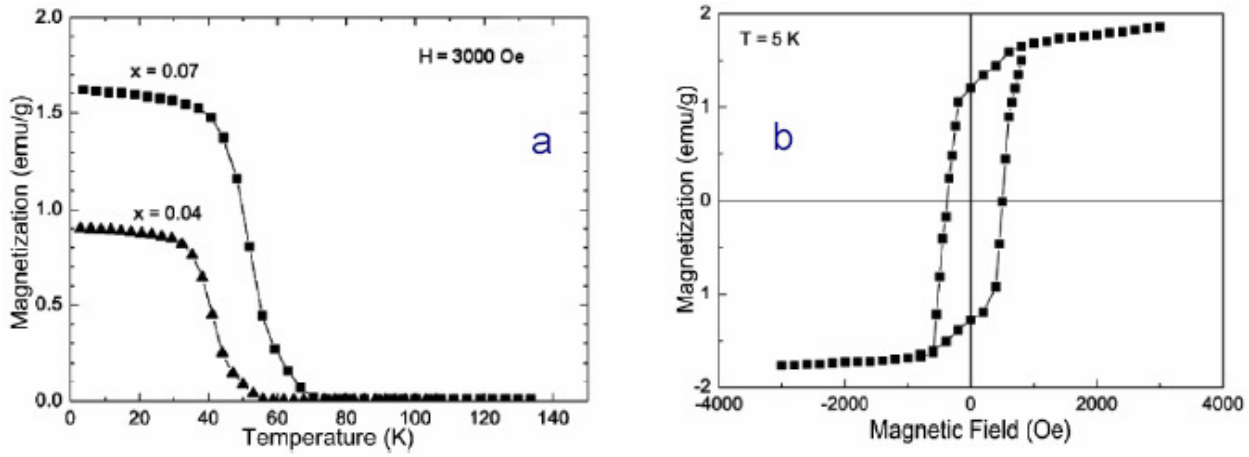

Figure 2.29 Ferromagnetic $Zn_{1-x}Mn_xO$ with low Tc. a) Temperature dependence of magnetization in a field of 3000 Oe from 5K to 300K. b) A hysteresis is for $Zn_{0.93}Mn_{0.07}O$ at temperature 5K; the T_c is determined to be 70K from a) (after Ref. 61).

Lower T_c or only all paramagnetism in transition metal doped ZnO has also been reported. Kim et al. reported T_c of 55K and 70K (see figure 2.29) for $Zn_{0.96}Mn_{0.04}O$ and $Zn_{0.93}Mn_{0.07}O$ without observation of other phase than ZnO by XRD [61]. Jung et al.

observed T_c=45K for $Zn_{0.7}Mn_{0.3}O$ [63]. Compared to the low T_c ferromagnetism observation, Cheng et al. found no ferromagnetism at all in their reactive rf magnetron sputtered $Zn_{0.93}Mn_{0.07}O$ films [60]. Instead the temperature dependence of magnetization from 5K to 300 K in 1000 Oe can be well described by the Curie-Weiss Law $\frac{M}{H} = \frac{C}{T - \Theta'}$ with small Curie-Weiss temperature as 1.17K, indicating the Mn moments are nearly noninteractive [60]. Paramagnetic homogeneous $Zn_{1-x}Co_xO$ films can be obtained by PLD with $T_s \leq 600^o C$; a large negative Θ' corresponds to strong antiferromagnetic exchange coupling [69].

Unlike the observed RTFM in Co doped TiO_2 that originates from Co clusters, most of the ZnO based DMOs have FM which is determined by carrier concentration. Saeki et al. confirmed this by providing a relationship between ferromagnetism and carrier concentration in V doped ZnO films [53]. The ferromagnetism can only be observed in samples with carrier density higher than $10^{18}cm^{-3}$, suggesting that the conductive samples are ferromagnetic and the insulate samples are non-magnetic (see figure 2.30). The authors claimed the RKKY carrier mediated ferromagnetism with substitution of V^{2+} for Zn^{2+} [53]. However, they assumed V is magnetic [53].

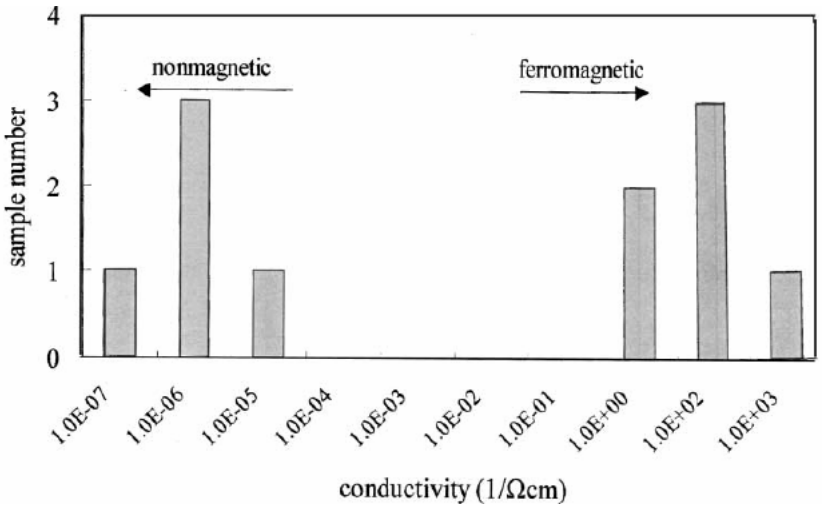

Figure 2.30 The Relationship between magnetic properties and conductivities in $Zn_{1-x}V_xO$ films (from Ref. 53).

Transport properties For transport and magneto transport measurements, small amounts of Al are generally added at 1 mol% (or 1 wt %) to the transition metal doped ZnO as an electron dopant. The resulting films are n-type. Compared to the Co doped TiO_2, ZnO based materials have higher carrier concentration. Carrier concentrations of at least $10^{19}cm^{-3}$ can be achieved as measured by the Hall effect ([57], [59], [64], [68], [69]). Doping with phosphorus results in p-type (Zn, Mg)O material [81]. Furthermore, as summarized by Norton, et al. p-type ZnO material can also be achieved with introduction of other candidate dopants, such as Cu [81].

Both metallic and semiconducting characteristics have been reported in the literature. As stated above, Ueda et al. noticed that the Curie temperature T_c, and saturation magnetization, M_s, of laser ablated $Zn_{1-x}Co_xO$ films depends on the cobalt concentration. Two samples from their work are listed in table 2.7. Thus they concluded that the ferromagnetism originates from a carrier-induced mechanism [57].

Table 2.7 magnetic and transport properties (after Ref 57).

films	Tc(K)	Ms (emu/g)	R vs. T	n(cm^{-3})	μ (units unavailable)
$Zn_{0.85}Co_{0.15}O$	300	17	Metallic	$2.9*10^{20}$	17.9
$Zn_{0.75}Co_{0.25}O$	280	5	Semiconductive	$1.2*10^{18}$	53.2

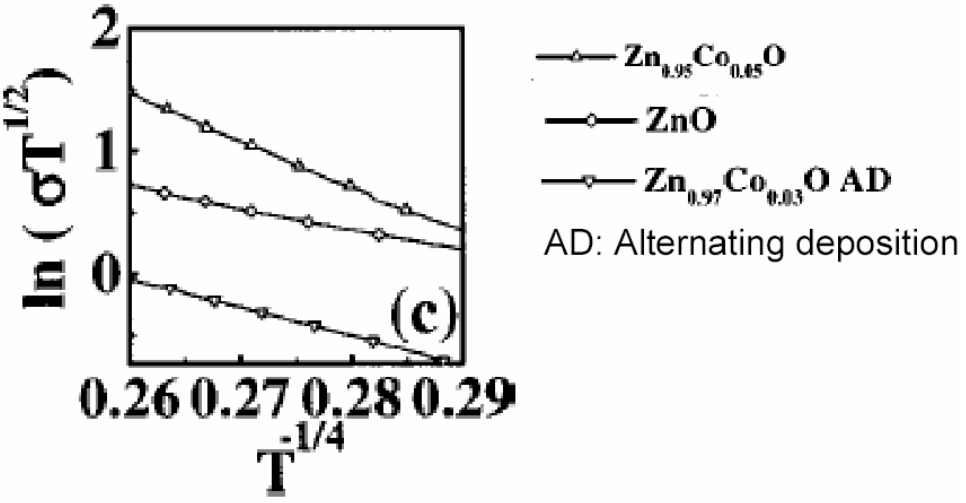

Figure 2.31 $\ln(\sigma T^{1/2}) vs. T^{-1/4}$ (after Ref. 70).

Yoo, et al. [70] reported a $T^{-1/4}$ temperature dependence of the resistivity in $Zn_{0.95}Co_{0.05}O$, $Zn_{0.97}Co_{0.03}O$ with Al codoping, ZnO (see figure 2.31), and suggested that the conduction mechanism in these ZnO based materials at temperatures below 220K is variable range hopping of localized electrons between impurity levels [70].

There have been very few reports on the anomalous Hall Effect observation in ZnO based materials and Hall measurements attain only the magnitude and sign of the carriers.

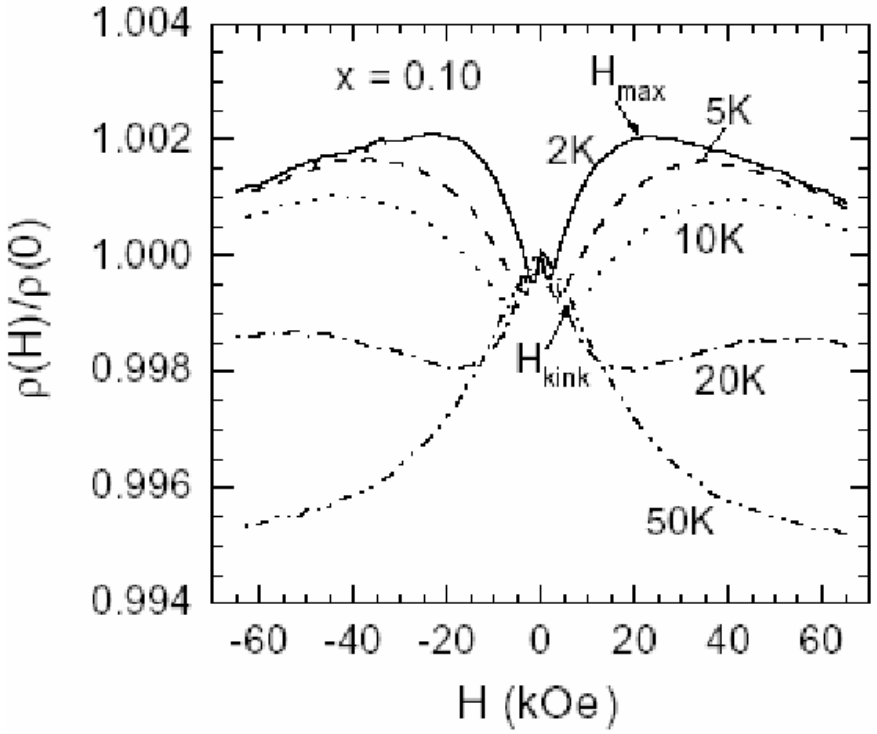

Figure 2.32 MR of $Zn_{1-x}Co_xO$: Al films of various Co content of $x = 0.10$ 1 mol% Al was added to the targets in the films fabrication by PLD (after Ref. 68).

ZnO is suitable for the study of magnetotransport, since it has a single-valley conduction band and the possibility of heavy n-type carrier doping [64]. There are two kinds of MR, positive and negative MR. The net MR is determined by the competition between them. Unlike the MR in TiO_2: Co, similar MR effects in ZnO based materials are consistently observed by several research teams ([59], [64], [68], [69]). As an example, isothermal MR at various temperatures for laser ablated $Zn_{0.9}Co_{0.1}O$ thin films with 1 mol% Al is shown in figure 2.32. At low temperatures ($T < 20K$) the sign of MR varies with applied

magnetic field. It is negative at low applied magnetic filed followed by an upturn at H_{kink}; after that with increasing magnetic filed, the MR turns negative again at a peak of H_{max}. H_{kink} and H_{max} decrease at lower temperature. In the vicinity of zero fields $H < H_{kink}$, the negative MR effect is due to a weak localization mechanism. The positive MR at $H_{kink} < H < H_{\max}$ is well understood in terms of the spin splitting caused by sp-d exchange interaction between the conducting electrons and the localized d-electron spins of the magnetic impurity ions [103]. At field $H > H_{\max}$ the negative MR happens due to decrease of spin-disorder scattering. This reduction is caused by the alignment of spins of both magnetic impurity ions and the electrons at high field. The spin-disorder scattering is also degraded at low temperatures, which results in smaller H_{max} at a lower temperature [68]. The authors claimed that H_{kink} decreases at a lower temperature because the sp-d exchange coupling is enhanced [68].

2.3.2 SnO_2 Based Materials

2.3.2.1 Introduction

Similar to TiO_2, SnO_2 also has a band gap with $E_g = 3.6eV$. SnO_2 has a tetragonal crystal structure with lattice constants of $a = b = 4.7374$ Å, $c = 3.1864$ Å. It has been investigated as a transparent electrode and gas sensors. SnO_2 has n-type conductivity, where the existence of oxygen vacancies acts as a source of donors and thus dominates the electrical conductivity [104]. Doping with Sb produces large n-type carrier concentrations up to 10^{20} cm^{-3} in SnO_2 [85]. All these properties have created interest in this material as a potential host of DMS for spintronics research. A giant magnetic moment of 7.5 μ_B/Co and high Curie temperature of $T_C = 650K$ has been reported in cobalt-doped SnO_2 thin film with $x = 5\%$ [88]

2.3.2.2 Fabrication

To produce SnO_2 based DMS, various transition metals have been doped into tin oxide or Indium-tin oxide, such as Mn ([84]-[87]), Co ([87]-[90]), Fe ([87], [91]-[92]), Ni ([87],

[93]-[94]), Cr ([87], [93], [95]), etc. There are also studies on rare earth doped $Sn_{0.95}RE_{0.05}O_{2-\delta}$ bulk material, where RE=Gd, Dy, and Er [96]. A variety of methods such as PLD ([84]-[85], [87]-[88], [90]-[93], [90], [95]), reactive thermal evaporation [86], and spray pyrolysis [89] have been used to prepare film samples. Ni^{2+}: SnO_2 nanocrystals synthesized by direct chemical methods were also studied with gentle annealing at 100°C [94]. Proper growth parameters are selected and adjusted during film deposition. Similar to TiO_2 based DMOs, sapphire is most widely used as a substrate to achieve good crystallinity ([84]-[88], [91]-[93]). There are also film samples grown on Si/SiO_2 [86], Si (100) ([90]), $LaAlO_3$ ([49], [93]) as well as quartz [89].

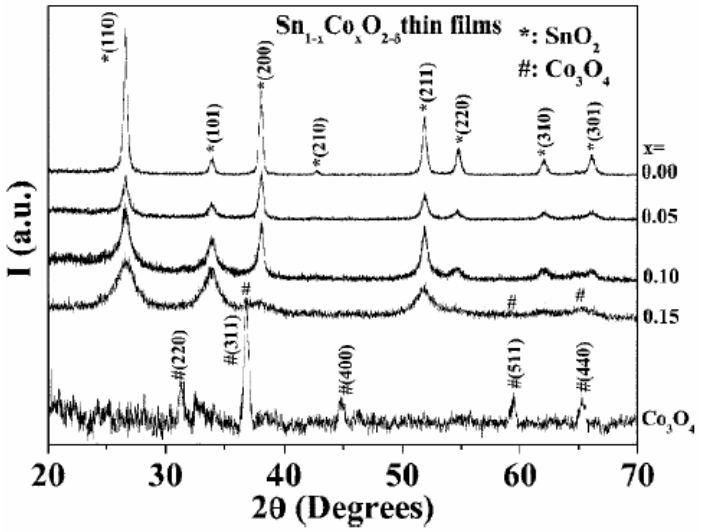

Figure 2.33 X-ray diffraction patterns of $Sn_{1-x}Co_xO_{2-\delta}$ and Co_3O_4 thin films, showing the presence of secondary phase (Co_3O_4) when $x = 15\%$ (after Ref. 89).

So far the high solubility of transition metal dopants into SnO_2 has been reported. The solubility of Mn in SnO_2 at thermal equilibrium is below 0.004%. It is possible, however, to exceed this value greatly by the nonequilibrium growth process of PLD. It is found that Mn doped SnO_2 can be achieved in the rutile structure without impurity phase up to $x = 0.34$ [85]. For Co doped material, PLD deposition with proper deposition parameters can result a uniform Co distribution with high XRD intensity for x up to 27% [86]. As for samples prepared by spray pyrolysis followed by annealing at 500°C for 30min, single phase rutile is observed for x up to 10%. For $x = 15\%$, a second phase of Co_3O_4 is observed [89], which suggesting the solubility limit of Co for spray pyrolyzed $Sn_{1-x}Co_xO_2$

is close to 10% (see figure 2.33). For Cr doped SnO_2, Wang et al. pointed out that up to 20% Cr can dissolve in SnO_2, as an interplanar spacing of the resulted samples exhibit a linear change with the Cr concentration [92]. Fitzgerald et al. studied laser ablated films of SnO_2 doped with Mn, Fe and Co in various dopant levels. They found that all the films are dilated perpendicular to the plane of the substrate. However there is no definite relationship between lattice constant and impurity concentration with random distribution of lattice constants around the value of bulk SnO_2 [87].

2.3.2.3 Properties

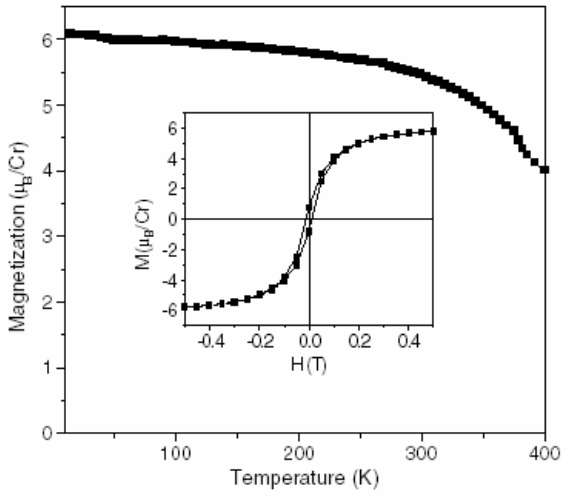

Figure 2.34 M vs. T for $Sn_{0.95}Cr_{0.05}O_2$ grown on LAO. The applied field for M vs. T is 5000Oe. The inset shows an open loop in M vs. H at 300K for the same sample (after Ref. 95).

The first report of room temperature ferromagnetism in SnO_2 based material is in $Sn_{0.95}Co_{0.05}O_2$ [88]. After that, high temperature ferromagnetism was subsequently reported in $Sn_{0.95}Fe_{0.05}O_2$ with $T_c = 610K$ and $M_s = 1.8\mu_B / Fe$ by Coey et al. [91], in Mn doped Indium-tin oxide films with $M_s = 0.8\mu_B / Mn$ [86], in $Sn_{0.95}Cr_{0.05}O_2$ on LAO substrates with a giant magnetic moment of 6 μ_B/Cr [95], in 0.48% Ni^{2+}: SnO_2 nanocrystals [94], and in $Sn_{0.9}Co_{0.1}O_{2-\delta}$ films with a saturation moment of $M_s = 0.47\mu_B / Co$ [89]. Fitzgerald, et al. reported that thin films of SnO_2 exhibit ferromagnetic properties at room temperature when doped with Cr, Mn, Fe, Co, or Ni,

but no room temperature ferromagnetism with other 3d transition metal dopant [87]. An example of the intrinsic ferromagnetism is demonstrated in figure 2.34.

Several suggestions for the origin of ferromagnetism have been advanced. Archer et al. hypothesized that nonstoichiometric grain-boundary defects can mediate magnetic ordering and proposed that interfacial oxygen vacancies are the activating defects [94]. Hong suggested that elimination of defects as well as filling up oxygen vacancies degrade ferromagnetism [93]. RKKY interactions have been proposed by Gopinadhan et al. as the mechanism for the ferromagnetic ordering in $Sn_{0.9}Co_{0.1}O_{2-\delta}$ [89]. Coey et al. proposed the ferromagnetic coupling of ferric ions via an electron trapped in a bridging oxygen vacancy (F center) to explain the high Curie temperature of 610K in $Sn_{0.95}Fe_{0.05}O_2$ thin films [91]. Fitzgerald et al. summarized that much of the magnetic moment is associated with electronic defects or lattice defects, and dopants somehow serve to activate the defect moment [87].

Other than the observation of high temperature ferromagnetism as well as single phase crystalline structure, many other magnetic properties are also reported. Wang et al. reported that films of SnO_2 with dissolved Cr are not ferromagnetic [92]. High T_c in Fe doped SnO_2 have been reported [91]. In the same material, superparamagnetic-like ZFC-FC curves have been reported which suggest the existence of precipitates of small ferromagnetic particles [92].

SnO_2 has always been reported to be n-type and a semiconductor, with or without Sb doping ([84]-[86], [87], [89]). The carrier concentration varies from 10^{19} to $10^{20} cm^{-3}$. As was found in some of the TiO_2 based DMOs, an abrupt increase of ρ with decreasing temperature below 50K or lower is usually observed for low doping concentration SnO_2([84]-[85], [87]-[88]). It is of note that in spray pyrolyzed $Sn_{0.9}Co_{0.1}O_{2-\delta}$ films, a room temperature anomalous Hall behavior is observed simultaneously with ferromagnetic properties. That the saturation field of the Hall resistance coincides with the M vs. H behavior confirms an intrinsic ferromagnetism ([86], [89]). Furthermore, the authors also reported that the saturation magnetization monotonically increases with increasing Co content (0-10%) from 0 to $0.47\mu_B$/Co, the resistivity monotonically

decreases from 35 to 6 mΩ-cm, and the carrier concentration monotonically increases from $1*10^{19}$ to over $6*10^{19}$ cm^{-3}. The authors proposed the RKKY interaction as the most probable mechanism for ferromagnetic ordering [89]. The relationship between M vs. H and the Hall resistance vs. H is demonstrated in figure 2.35.

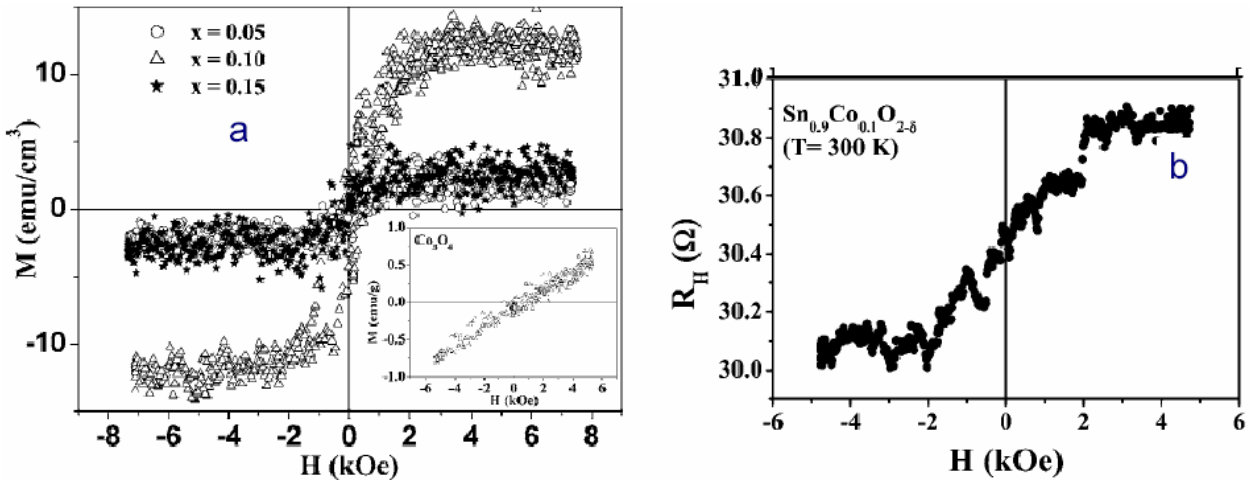

Figure 2.35 Results on magnetic and Hall measurements of $Sn_{1-x}Co_xO_{2-\delta}$ films. a) M vs. H curves. The inset shows the M vs. H behavior of Co_3O_4 thin film. b) Hall resistance as a function of applied field at room temperature (after Ref. 89).

MR has also been investigated in some of the magnetic doped SnO_2 films. The results of MR in Mn doped SnO_2 varies with the Mn concentration [85], this is similar to that of ZnO based DMOs ([68]-[69]) and is explained in the same manner.

2.3.3 Others

In addition, there has been work on potential DMS based on other oxides, such as $La_{1-x}Sr_xTi_{3-\delta}$ with cobalt doping [97], Cu_2O with cobalt doping [98], and NiO with Fe doping [99], all of which exhibit RTFM. Since the magnetism shows no clear dependence on the resistivity, the authors suggested the FM mechanism may be related to orbital defects in $La_{1-x}Sr_xTi_{3-\delta}$ thin films with 5 at. % Co doping and 0.5 at. % Al doping [97].It was suggested that carrier density and dynamics plays a strong role in the FM mechanism in Cu_2O: Co, and defects may also contribute to the FM mechanism [98]. For NiO: Fe, the authors inferred that ferromagnetic clusters and FM/AFM coupling due to composition inhomogeneity determine the RTFM.

2.4 Summary

Recent reports on potential DMSs prepared from the host materials TiO_2 with cobalt are reviewed. The following two important issues have been addressed: 1) the mechanism for the observed RTFM and 2) the presence of the secondary phase Co. It was found out that growth conditions greatly affect the formation of the nonstoichiomitry of TiO_2: Co; in particular, lower PO_2 results in more conducting films with enhanced phase segregation and cobalt clustering. Experimental evidence for both intrinsic carrier mediated FM and extrinsic secondary phase Co metal dominated FM has been observed. The solubility of cobalt in TiO_2 varies from 2% to 40%. Co precipitation depends on a number of factors including cobalt concentration, growth method and growth parameters.

The potential of ZnO doped with various TM impurities to produce DMS is reviewed briefly. Some of the resulting material show high temperature FM. Unlike the situation in TiO_2 based DMOs, most of the reported FM in ZnO based DMOs has been suggested to have an intrinsic origin. One highlight is that a bound magnetic polaron model is proposed to explain the RTFM in Mn doped ZnO with additional Sn doping, and for Co doped ZnO. The solubility of TM in the ZnO wurtzite lattice depends on growth conditions. It is also reported that ZnO could be either n-type or p-type, depending on dopant elements.

The magnetic and transport properties of SnO_2 doped with TMs are also briefly discussed. Most of the reported material is ferromagnetic at room temperature. RTFM has been explained by several mechanisms, such as RKKY carrier mediated FM and through defect coupling of oxygen vacancies to magnetic ions. There is also at least one report of FM due to the formation of secondary phase ferromagnetic particles.

There are few consistent results from group to group for any of these oxides, suggesting that film properties are very sensitive to growth conditions.

CHAPTER 3

$TiO_{2-\delta}$: Co

3.1 Introduction

Our previous work showed that cobalt clusters are formed in $TiO_{2-\delta}$: Co [35]. There are a number of reports claiming that there is an oxygen growth pressure (PO_2) effect on cobalt precipitation ([16], [18], [29]). However there is no report on the PO_2 effect on cobalt clustering over a smaller range of PO_2 variance. Furthermore, varying the PO_2 may provide more systematic correlation between the transport properties and magnetic properties, since lower PO_2 induces more oxygen vacancies which were proven to introduce n-type carriers and increase the overall conductivity of the films ([30]-[31]). Here we study a series of $TiO_{2-\delta}$: Co thin films deposited with various oxygen growth pressures within range from 0.023mTorr to 0.1mTorr. The characterization experiments will be described below, and the main points from magnetic, transport and structural studies will be presented. I will also discuss the results and draw a conclusion.

3.2 Sample preparation

3.2.1 Fabrication

The substrate for growth of rutile $TiO_{2-\delta}$: Co thin film was c-sapphire Al_2O_3 (001). Successful growth of (100) oriented rutile on c-sapphire has been reported in the literature [23]. The sapphire is a hexagonal crystal system, as shown in figure 3.1, and the lattice parameters are $a = 4.785$ Å and $c = 12.991$ Å. The lattice mismatch between c-sapphire and rutile TiO_2 ($a = 4.59$ Å, $c = 2.96$ Å) is 7.05% along $[001]_{rutile} \parallel [10\bar{1}0]_{sapphire}$ and -3.59% along $[0\bar{1}0]_{rutile} \parallel [\bar{1}2\bar{1}0]_{sapphire}$. Thus under certain conditions during growth, cobalt diffusion may produce Co clustering in the defect rich area at the interface. For film deposition, the c-cut sapphire substrates were cleaned with acetone and methanol prior to being mounted to a Kanthal heater inside a PLD chamber.

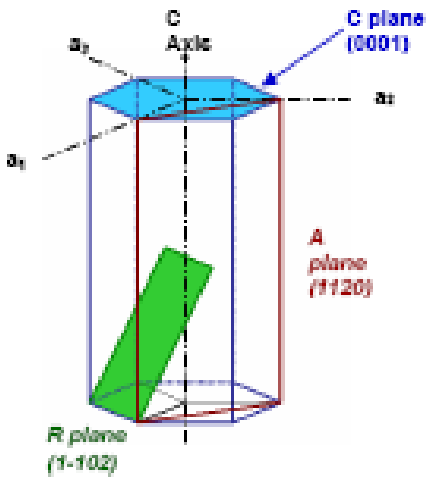

Figure 3.1 Crystal structure of sapphire.

The $TiO_{2-\delta}$: Co films were fabricated by means of the PLD technique. For film growth, an Nd: YAG laser operated at the fundamental frequency (1064nm, 10Hz) is used. To ensure even wear on the target, the laser beam was focused on and rastered across the target. The film deposition process is schematically shown in figure 3.2, where a pulsed laser beam hits and vaporizes the target surface to produce a plume, and then the vapor condenses on a substrate to create a film.

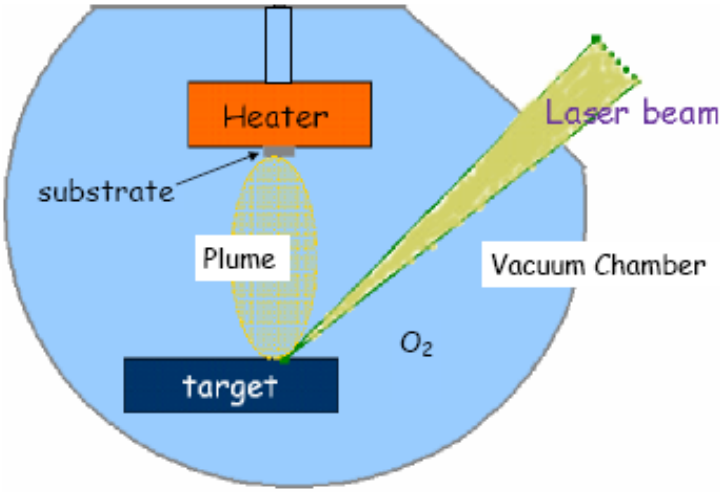

Figure 3.2 Principle of Pulsed Laser Deposition. The substrate temperature is usually maintained constant during deposition.

The targets were prepared with standard ceramic methods. Powders of CoO and TiO_2 with molar ratio of $Co/Ti = 0.07/0.93$ were mixed thoroughly. Then the resulting powders

were pressed into a 2.5cm diameter disc and sintered at 1200°C. The resulting disk serves as a target for growth of $TiO_{2-\delta}$: Co thin films with 7at% cobalt.

Prior to film deposition the chamber was evacuated to the base pressure of $1x10^{-7}$ torr. During growth the chamber was backfilled with O_2 gas to produce a constant ambient pressure during the film growth. As mentioned earlier, the growth pressures were varied from 0.023m Torr to 0.1m Torr over the series of films studied here. The relatively low oxygen growth pressures are expected to create a reasonable amount of oxygen vacancies, which are expected to provide charge carriers for further transport study; furthermore, it also assists the formation of cobalt clusters. Typically films are grown at pressures an order of magnitude larger to obtain oxygen stoichiometry. Thus it will be interesting to study the interplay among the magnetic, transport, and the structural behaviors.

The temperature of the substrate is measured with a Mikron optical pyrometer and controlled by applying a constant current through the heater. The temperature of the substrate during growth is maintained at 720°C value to obtain optimum growth [23].

3.2.2 Initial characterization

3.2.2.1 Experiment

The crystal structure of the films was measured by a Philips PW3040 four-circle X-ray diffractometer. This machine is optimized for characterization of thin films and has a minimum linewidth of 0.3° for the (004) reflection of a standard single crystal wafer of silicon.

The θ/2θ scans were routinely measured immediately after growth to check the epitaxy as well as to determine the crystal structure of the resulting samples.

The thickness and area of the films were also measured. A TENCOR profilometer was utilized to measure the sample thickness as well as the surface roughness. The area of each film was measured via an OLYMPUS optical microscope apparatus which is

equipped with a digital camera with scaling. The optical microscope also provides first look of the surface quality of the films.

3.2.2.2 Results and discussion

To study the effect of oxygen deficiencies, we focused on the 5 samples at PO_2 of 0.023mTorr, 0.04mTorr, 0.06mTorr, 0.08mTorr and 0.1mTorr with the other two samples at 0.05mTorr and 0.2mTorr for comparison. The five important samples were prepared in well-controlled manner. They were deposited for the same period of time, from the same target, and with almost identical growth conditions except the PO_2. The 0.2mTorr film and the 0.05mTorr film were deposited at an earlier time. As seen in table 3.1, the films are roughly 5000Å thick.

Table 3.1 Sample Dimensions

PO_2 (mTorr)	0.023	0.04	0.06	0.08	0.1	0.05	0.2
Thickness(Å)	4630	4662.5	4777.8	5230	4912.5	5525	6100
Area(mm^2)	1.25	3.50	2.87	2.29	5.42	23.37	4.49

It is well known that the nature of the nonstoichiometry defines the physical properties of cobalt doped $TiO_{2-\delta}$. Thus the creation of nonstoichiometry, which occurs during the deposition process, is crucial. Since the 0.05mTorr and the 0.2mTorr sample were grown at a different time, there may be some divergence in the properties of these samples as compared to the rest of the group due to a number of parameters: sample change during storage, variation in oxygen gauge over time, potential change in target, etc. Furthermore, compared to the other samples, the PO_2 of 0.2mTorr sample is much higher than the others, which may also result in a slight divergence of properties of this sample from tendencies of the rest group in physical properties as a function of PO_2. For discussion in this chapter, I will focus on the five samples from 0.023 to 0.1mTorr samples for PO_2 effect.

In general the samples are relatively rough on the surface. Figure 3.3 shows one image of 0.05mTorr film under optical microscope as a representative. All the films have almost identical surface roughness. The rough surface was also confirmed from

profilometry. The roughness of the films is not surprising because of the PLD deposition technique, as aforementioned in chapter two. The cluster-like features on the surface are not cobalt clusters but clustered $TiO_{2-\delta}$: Co, since further studies show the cobalt clusters are in the range of nanometers.

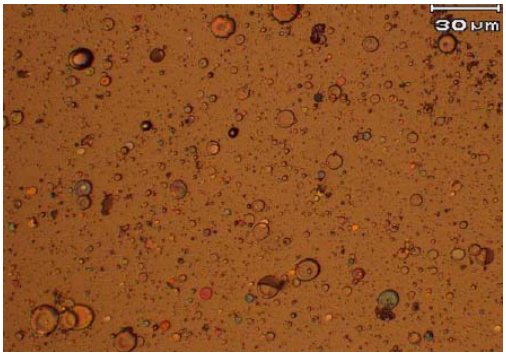

Figure 3.3 Representative surface image of the laser ablated $TiO_{2-\delta}$: Co films. The particles shown are not cobalt clusters but rather 'splatter' resulting from ablation of the target material.

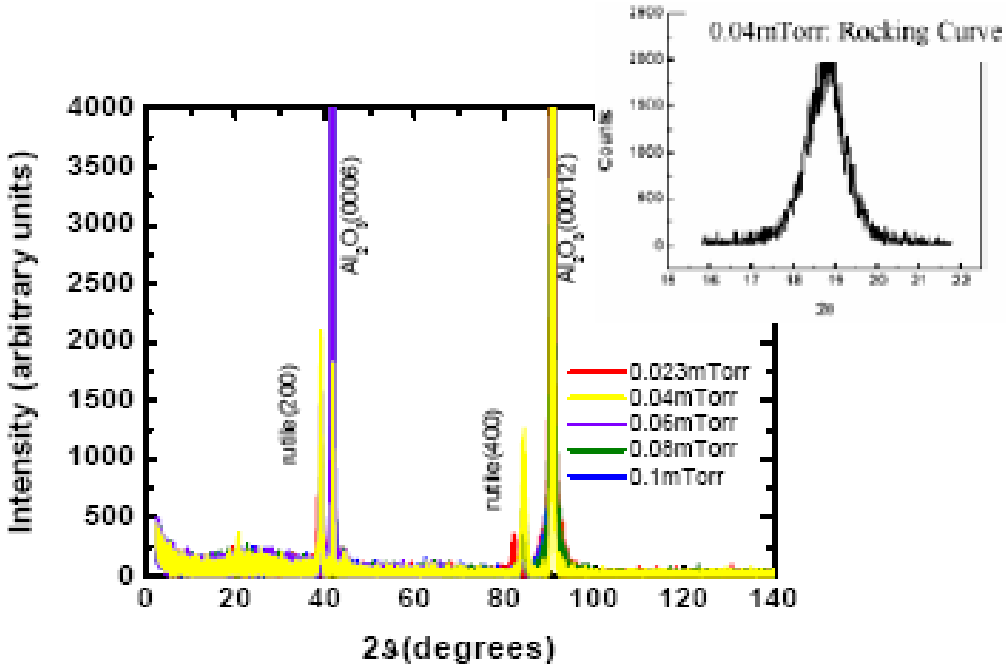

Figure 3.4 θ-2θ XRD patterns of cobalt doped $TiO_{2-\delta}$ thin films deposited on c-cut sapphire (001). The inset shows a representative rocking curve.

Figure 3.4 shows a representative θ-2θ XRD pattern of the deposited films. The scanned range is from 2.51° to 140°. The y axis is for the intensity. The inset shows a representative rocking curve. As can be seen from the inset, a normal FWHM for the

studied films is as large as 1°. This wide FWHM is a result of the large lattice mismatch, the large number of oxygen vacancies, as well as all of the cobalt clustering. For films grown at optimum conditions the FWHM is much smaller [14]. In the XRD pattern, other than the sapphire peaks, only (200) and (400) peaks of rutile structure are observed. This indicates that the film has grown epitaxially and with (100) orientation along with the film growth direction.

So far no secondary phase such as cobalt crystal structure was detected by XRD. However, as will be discussed later, cobalt nanoparticles are detected by further magnetic characterization, which was further confirmed by transport studies; finally cobalt clusters were observed via transmission microscopy.

3.3 Magnetic investigation

3.3.1 Experiment

The magnetic properties were measured by a commercial superconducting quantum interference device (SQUID) magnetometer. For mounting purposes, a clear straw was used. Prior to films measurement, identical straws were measured and resulted in negligible signal. Straw pieces may be used for stabilization in the case that the film sample is too small to stay in a certain location during measurement. Then the straw with the film inside was attached to a measuring probe and loaded into SQUID. Centering was performed to ensure the signal to be measured is from the sample. The signal from substrate was carefully subtracted from the resulted data in analysis. The magnetic field is parallel to the film surface during magnetic measurement.

To check the existence of ferromagnetism, measurements of magnetization as a function of applied magnetic field at certain temperatures were performed. In order to investigate the magnetic contribution from the cobalt precipitation out of the $TiO_{2-\delta}$ matrix, a Zero Field Cooled-Field Cooled (ZFC-FC) measurement was also performed. In ZFC-FC, the film was brought to the lowest measurable temperature with $H = 0$. After centering with an applied field of H~0, a small magnetic field ($H << Hsaturation$) is

applied, and the temperature dependence of magnetization, a ZFC curve, was measured with the temperature increasing. After the temperature reaches the highest measurable temperature, the ZFC curve was finished. Then with the same applied field, an FC curve of the magnetization as a function of temperature is measured as the temperature drops.

Magnetization as a function of temperature is also characterized with the following procedure: Starting from the lowest measurable temperature, at each temperature, magnetic moment is measured at a finite field of 1000Oe, then at a saturated field of 1T, followed by a remanence measurement 100s after the removal of the 1T applied field. Here the time of 100s was utilized because of convenience of data analyses; also it is the empirical laboratory time scale for magnetic measurements.

3.3.2 Results and discussion

Room temperature M_s vs. PO_2 The M_s of the samples varies in the range of 1.3-2.5 μ_B/Co. As shown in figure 3.5, the M_s distributes on both sides of 1.7 μ_B/Co of bulk cobalt metal. In this particular PO_2 range, it seems like M_s increased with higher PO_2.

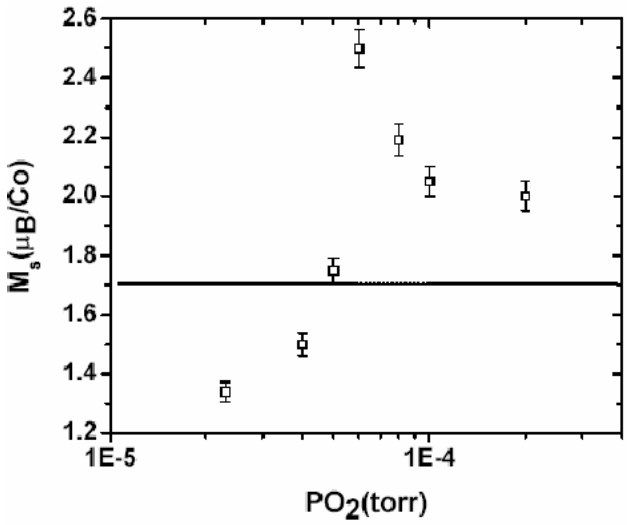

Figure 3.5 Saturation magnetic moment of $TiO_{2-\delta}$: Co thin films as a function of PO_2. The solid line is M_s for cobalt metal.

If the Co is incorporated into TiO_2 matrix in the form of Co ions, this tendency indicates that the Co ion is in a lower spin state with lower PO_2 and in a higher spin state with higher PO_2. The fact that the M_s is higher than that for bulk cobalt could be explained by a number of factors, one of which is uncertainty in the number of cobalt atoms contributing to the magnetic signal. As a result, further characterization is necessary to discover the cobalt distribution.

Magnetization as a Function of Field

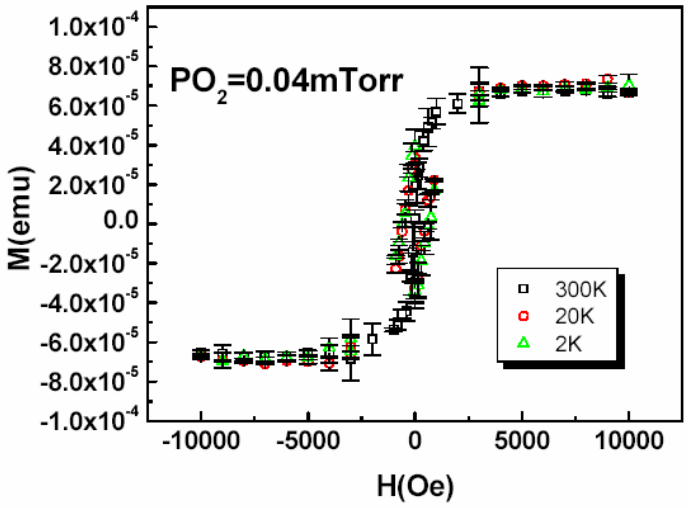

Figure 3.6 Representative M-H curves at different temperatures. The sample was deposited in an ambient of 0.04 mTorr PO_2.

Figure 3.6 shows the magnetization as a function of applied magnetic field at various temperatures for the 0.04mTorr sample as a representative. Similar curves were also observed in other samples with various M_s and H_c. In the figure, the M vs. H curves of the 0.04mTorr sample, the saturated magnetic moment is a constant in the measured temperature range from 2K to 300K. In fact this is also true for the other measured samples. For the sample with $PO_2 = 0.04mTorr$, at 2K and 20K, the coercive fields are as high as 608Oe and 517Oe, respectively. The coercive field quickly drops to ~0 within measurement uncertainty at room temperature.

The trend of the coercive field with temperature indicates that there is a transition from a ferromagnetic state at low temperatures to a paramagnetic state at high temperature. In

an intrinsic ferromagnetic material, ferromagnetism with nonzero coercive field occurs at temperature $T < T_c$, and a paramagnetic state with a closed M-H curve presents above the Curie temperature. However, when crossing the Curie transition temperature, the spontaneous magnetization drops from a constant value below T_c to ~0 above T_c. Apparently this situation doesn't fit the data in figure 3.6. Thus the 0.04mTorr sample is not an intrinsic ferromagnetic sample. In fact, for all the studied $TiO_{2-\delta}$: Co films, considering the constant saturation magnetic moment at all measured temperatures with a H_c variation from hundreds of Oe to around zero, an intrinsic ferromagnetism must be excluded. Thus there exists the possibility of cobalt clustering dominance in the magnetic behavior, since for cobalt metal, the T_c is as high as 1404K, below which the magnetic moment rises rapidly as expected for a Curie Weiss magnet and remains constant.

At low temperatures, all films show ferromagnetic behavior with open hysteretic loops. The observed H_c varies from 380Oe to 650Oe. Saturated magnetic moments keep being a constant in the whole temperature range from 2k up to 350K.

Room temperature H_c vs. PO_2 At the elevated temperature of 300K, the coercive fields are much smaller than at low temperature. The room temperature values of H_c vary from over 200Oe to around zero Oe, with an interesting dependence on PO_2.

Figure 3.7a) shows the room temperature coercivities as a function of PO_2. It is demonstrated that for the samples with lower PO_2 ($\leq 0.05mTorr$), the coercivities are ~0. For samples with $PO_2 \geq 0.05mTorr$, nonzero H_c exists and increases with PO_2 until the PO_2 reaches 0.1mTorr.

This overall trend of H_c is comparable with the variation of coercivity with particle diameter crossing the transition from superparamagnetic particles to single domain (not superparamagnetic) particles (as in figure 3.7 b) [105]. Figure 3.7b) shows a classical schematic picture of the correlation between coercivity and particle size for magnetic fine particles.

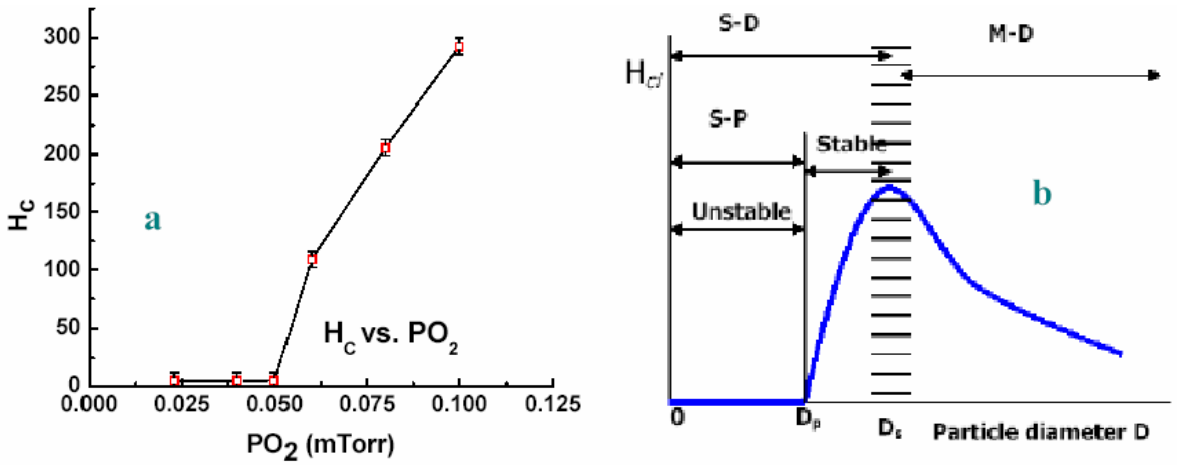

Figure 3.7 Coercive fields. a) The correlation between the coercivity (H_C) and PO_2 in $TiO_{2-\delta}$: Co thin films at room temperature measured at maximum field of 10kOe. b) The coercivity as a function of mean particle diameter, reproduced from [105]. Here in b) S-D means single domain, S-P means superparamagnetic and M-D means multi domain.

Depending on particle or grain size, the magnetic behavior can be subdivided in to three ranges:

- S-P is for superparamagnetic, where the particles have $D < D_p$ and are superparamagnetic particles (see pg. 30 and pg. 31).
- S-D is for single domain. In this range, the particles have diameter of $D < D_s$ and are single domain particles.
- M-D is for multi domain. The particles with $D > D_s$ contain multiple domains.

The variance of H_c when crossing the transition from superparamagnetic to single domain (non superparamagnetic) in figure 3.7 b) can be understood as follows. At a temperature which is lower than T_b but close to T_b, the thermal activation still does overcome the anisotropy energy of some particles since there is always a distribution of particle size. For an assembly of particles with smaller average volume, more particles are reversed, resulting in a state closer to superparamagnetism and with a smaller coercivity; on the other hand, with an average bigger size particles, H_c is bigger. Of course for those particles system above T_b and in superparamagnetic state, H_c is zero.

Now figure 3.7 a) can be understood as the behavior of assembly of single domain cobalt particles, which precipitated during film deposition. When at $PO_2 \le 0.05mTorr$, the cobalt particles are small enough to make the whole film show superparamagnetic behavior at room temperature. For films with $0.05mTorr < PO_2 \le 0.1mTorr,$ the precipitated cobalt particles are able to determine a blocked state magnetic behavior at room temperature. Furthermore, in this range, lower PO_2 results in lower H_c, which corresponds to smaller cobalt nanoparticles.

Thus it can be preliminarily concluded that when $PO_2 \le 0.1mTorr$, smaller cobalt particles resulted with smaller PO_2, and the cobalt particles dominate the magnetic properties. To confirm this, further characterization such as ZFC-FC is necessary to verify the clustering of Co in the laser ablated $TiO_{2-\delta}$: Co thin films.

ZFC-FC Representative ZFC-FC curves are shown in figure 3.8 for the sample with $PO_2 = 0.023mTorr$. In the figure a divergence of ZFC-FC curves at lower temperatures can be seen; the two curves overlap at high temperatures. Clearly, there is a hump in the ZFC curve, which occurs at T_b and indicates the presence of cobalt superparamagnetic nanoparticles. From the hump position in ZFC curve, $T_b \approx 80K$, a blocking temperature lower than 300K can be deduced.. Furthermore, the coincidence of ZFC curve and FC curve over 200K indicates a thermal equilibrium, which is consistent with the observation of zero coercivity at room temperature in figure 3.7 a).

The diverging ZFC-FC curves at lower temperatures are observed for all the samples, indicating the superparamagnetic cobalt particles occurrence in these films. For those samples with $PO_2 > 0.05mTorr$, the divergence between ZFC-FC curves happens at temperatures up to 345K, indicating that $T_b > 345K$. This is consistent with the nonzero H_c observation at room temperature in figure 3.7 a). For the other samples of $PO_2 \le 0.05mTorr$, $T_b < 300K$, which is consistent with $H_c \approx 0$ at room temperature in figure 3.7 a), indicating superparamagnetism at room temperature.

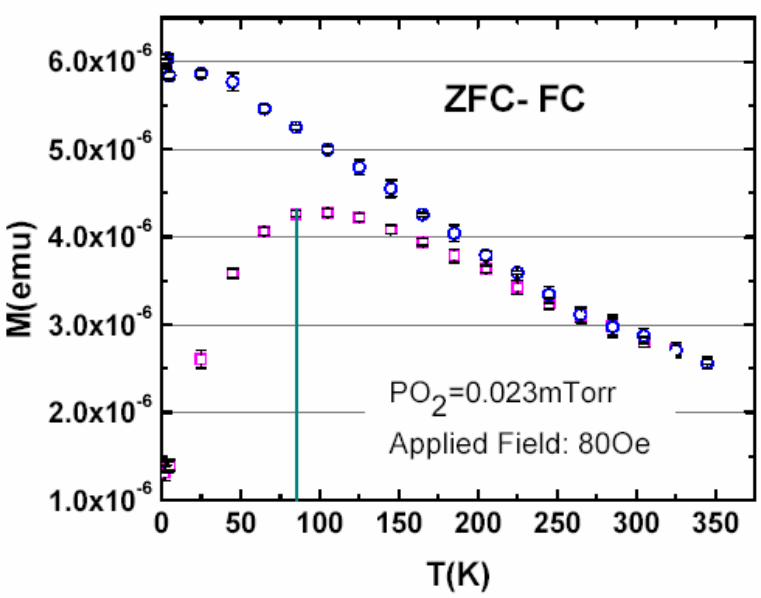

Figure 3.8 Representative ZFC-FC curves for the 0.023mTorr sample. The red symbols are FC curves, and the black symbols are for ZFC curves. The applied field is 80Oe.

Furthermore, lower T_b is observed in sample with lower PO_2. The observed blocking temperatures are listed in table 3.2. Since the blocking temperature is proportional to the product of anisotropy constant K and particle volume V, $KV = 25kT$, table 3.2 also implies that for the films deposited with lower PO_2, smaller Co nanoparticles are formed. This is also consistent with the variation of H_c values with PO_2 in figure 3.7 a).

Table 3.2 Correlation between T_b and PO_2

PO_2(mTorr)	0.023	0.04	0.06	0.08	0.1	0.05	0.2
T_b (K)	80	265	>345	>345	>345	285	>345

For the test film deposited with $PO_2 = 0.2mTorr$, the room temperature H_c of 254Oe is slightly smaller than the 292Oe of the film with $PO_2 = 0.1mTorr$. The nonzero H_c agrees with the observed $T_b > 350K$. However, this 0.2mTorr film was prepared with a PO_2 much higher than the rest group; furthermore this sample was not deposited in the same time period of the other samples. Film and target age may also affect film properties; thus the value of H_c for this sample may not not fall within those seen for the series grown at the same time.

Curve fitting to extract the dimension of cobalt particles Fitting the remanence as a function of temperature via the Néel decay law (see pg. 30) one can only obtain the product of the anisotropy constant K and the volume V. To derive the dimension of the cobalt particle from magnetic data on a dispersion of non-interacting superparamagnetic particles, Held et al. [106] simultaneously fitted the remanence over the measured temperature range and the finite field magnetization at temperature of thermal equilibrioum. Their theoretical model and fitting procedure will be described in the following.

The Néel decay law was described in the previous chapter (pg. 30). To fit the finite field moment at temperatures when the system is in thermal equilibrium, one must account for the energy of each particle. For an ideal isotropic single domain particle, the energy in an applied magnetic field $\vec{H}$ is $-\vec{\mu} * \vec{H}$. For an anisotropic particle, the energy is no longer $-\vec{\mu} * \vec{H}$; instead it turns out to be $E_{total} = -\vec{\mu} * \vec{H} + V * E_a$ [106], where the second term is the anisotropy energy. A unit vector $\hat{h}$ is can be used to indicate the orientation of the applied field with respect to the anisotropy axis of the particle with $\hat{h} = \vec{H} / \left|\vec{H}\right|$, and a unit vector $\hat{s}$ is used to indicate the orientation of the moment of the particle. Thus the total energy for a particle can be expressed as $E_{total} = -\mu\hat{s} * \vec{H} + V * E_a(\hat{s}, K)$ [106]. The resulted overall magnetic moment <M> can be calculated with a given $\vec{H}$, V, and K, followed by averaging over all orientations of $\hat{h}$. At temperatures where the system is in thermal equilibrium, the resulting <M> has the following form:

$$\left\langle M(H,T)\right\rangle = \int \frac{d^2\hat{h}}{4\pi} \times \left[\frac{\int d^2\hat{s}\mu(\hat{s} \bullet \hat{h}) e^{-E_{total}/kT}}{\int d^2\hat{s} e^{-E_{total}/kT}} \right] \qquad \text{([106])}$$

For the studied films, the initial remanence at the lowest measured temperature is always all around 0.5. This is consistent with a system containing superparamagnetic nanoparticles with one easy axis. For such a system with randomly distributed easy axis, after the system is fully magnetized, when the field is removed, the easy axis will

fall in a hemisphere around the field orientation and result in a remanence ratio (M/M_s) of $<\cos\theta>=0.5$ [105].

To simultaneously fit more than one group of M (M_R) vs. T is not straightforward. To process the fitting, Dr. Held has built a large amount of source code with Visual C. 6.0. With the help of my advisor, I have been lucky enough to contact Dr. Held personally and through his generosity was able to receive his code as well as invaluable instructions. I was able to go through the fitting with Visual C. software and Origin software in Windows operating system. To work it out, I built a dynamic-link library project with the provided code, added a user defined .fdf function definition file to a proper directory, modified the nonlinear curve fitting functions directory in Origin software, and finally choose proper parameters to perform the fitting. Since the fitting process is complicated with many fitting parameters such as K, V, dK, dV, etc, in general it takes as long as over 12 hours to finish one fit.

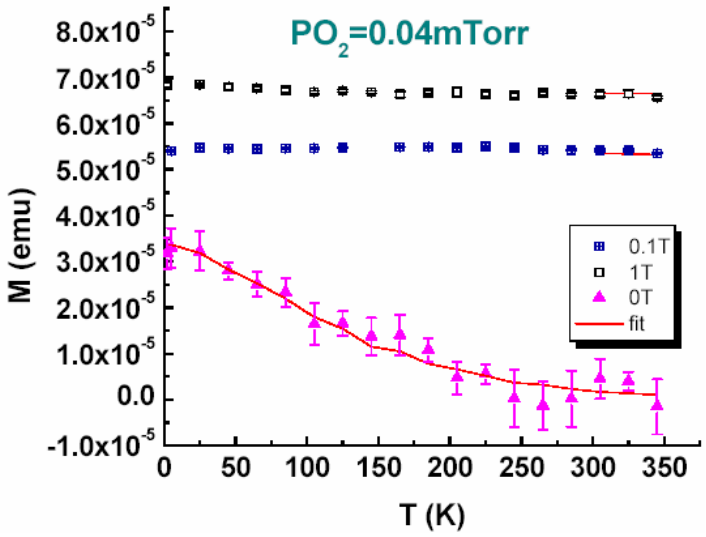

Figure 3.9 M vs. T for the 0.04mTorr sample. The blue crossed squares are moments at 0.1T, the black open squares are data at 1T, and the magenta solid triangles are the remanence points. The fitted curves are shown in as red solid lines.

Figure 3.9 demonstrates the magnetic moment as a function of temperature for the 0.04mTorr sample, where the solid lines are fitted curves obtained from the process sketched in the previous paragraphs. For this sample, a blocking temperature of 265K

and thermal equilibrium at temperatures over 285K were obtained and discussed previously. As can be seen in figure 3.9, the magnetization at 1T is almost temperature independent, indicating that the moments are saturated at this field; this is consistent with previous M vs. H investigations. In addition, the nonzero remanence at temperatures lower than 200K demonstrates that the system is at least partially blocked at this temperature range. This observation is consistent with the 265K blocking temperature. Using the procedure developed by G. Held et al. in [106], the magnetic moments at 1T and 1000 Oe are fitted at the thermal equilibrium temperature, which is above 300K in this sample, and the remanence is fitted simultaneously for the whole temperature range via Néel's decay law. The red lines are the fits.

With the mechanism and technique describe above, the fitting procedure has also been performed on the results from the 0.023mTorr and 0.05mTorr samples, since for these samples the thermal equilibrium state has been detected by the overlap of ZFC-FC curves. The extracted cobalt cluster dimensions have the tendency whereby smaller PO_2 results in smaller average dimension of the cobalt particles, as demonstrated in table 3.3. The slight deviation of the 0.05mTorr sample may be caused by many factors other than PO_2, as stated earlier. This tendency is consistent with figure 3.7 and suggested that the magnetic properties are sensitive to the dimension of cobalt clusters.

Table 3.3 Magnetic fitting suggested lower PO_2 results in smaller average cobalt clusters dimension.

PO_2 (mTorr)	0.04	0.023	0.05
$\bar{d}$ (nm)	8.12	8.06	8.74
Δd (nm)	2.70	2.68	1.46

Table 3.4 Comparison of magnetic fitting and TEM measurement for the 0.04mTorr film.

PO_2(mTorr)	$\bar{d}$ (nm)	Δd (nm)	$\bar{d}_{TEM}$(nm)
0.04	8.12	2.70	6.86

Table 3.4 lists the extracted dimension of nanoparticles with a normal distribution for this 0.04 mTorr sample. In the same table the average dimension determined from TEM

is also listed. It can be seen that the dimension from magnetic fitting is in good agreement with the dimension independently determined via TEM.

Furthermore the resulting anisotropy energy densities K from magnetic fitting are all of order of 10^5erg/cm^3, which is the same order of magnitude reported for K in bulk cobalt material.

These studies suggest that magnetic properties of the $TiO_{2-\delta}$: Co films are dominated by the precipitated cobalt particles, and fitting the magnetic data can result in reasonable dimensions of superparmagnetic particles as well as the anisotropy energy densities.

3.4 Transport properties

3.4.1 Experiment

Transport measurements were made via the conventional van der Pauw technique, which does not require special patterning or geometry. The contacts were soldered Indium (melting point 250°C) for small contact resistance. Before further experiments, the contacts were confirmed to be ohmic with linear I-V curves for both 2-probe and 4 probe measurements. To obtain the resistivity as a function of temperature, I-V curves were checked at fixed temperatures from 5K to 300K in a JANIS cryostat. The temperature was monitored by a Cernox thermometer below 77K and by a platinum RTD (resistance temperature detector) thermometer for higher temperatures. Isothermal Hall Effect and magnetoresistance were measured with a low frequency AC current source and lock-in amplifier detector during DC magnetic field sweeps at discrete temperature.

To measure the nonlinear I-V characteristics for field induced tunneling conduction after the observation of hopping conduction (the results and dominating mechanism will be described in the following results part), a large electrical field up to 10^5V/cm was applied across a sample strip with a width on the order of a micrometer. For that purpose, the films were patterned by photolithography. Prior to patterning, the samples were cleaned

with oxygen plasma so that better adhesion of photoresist on the film can be achieved. After patterning with photolithography, evaporation of chromium and gold was carried out, followed by liftoff to make contacts on both sides of the film strip (see figure 3.10).

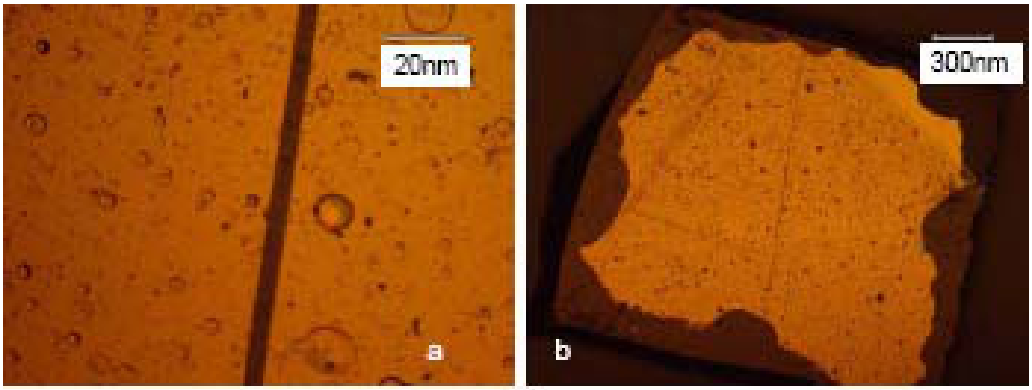

Figure 3.10 Representative geometry of the sample and contacts. The strip and circumference is for sample, and the rest golden area is for contacts. a) shows a 5.1 μm sample strip and b) shows the same sample in a larger scale.

For the voltage induced tunneling conduction, temperature need to be sufficiently low so that the thermal energy is less than the electrical energy and the dominant carriers are induced by voltage. Therefore, the measurements were completed at very low temperature of 0.35K using an OXFORD closed –cycle He_3 refrigerator.

3.4.2 Results and Discussion

Conductivity at RT The room temperature resistivity variation as a function of PO_2 is shown in figure 3.11. Clearly lower PO_2 resulted in lower resistivity. In other words, with more oxygen deficiencies during the deposition process, more conductive films are achieved. This is consistent with the reported variation of conductivity with PO_2 ([30], [31]) and confirms that oxygen vacancies in the films introduce charge carriers. Furthermore, the red solid line in this figure is an exponential fit of the ρ vs. PO_2. It indicates the resistivity roughly fits an exponential law with the PO_2, namely with increasing PO_2, the oxygen vacancies and charge carrier density decrease exponentially.

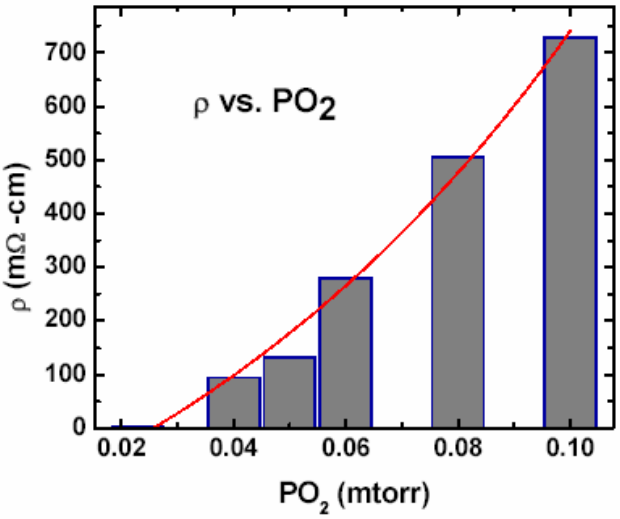

Figure 3.11 Room temperature resistivity vs. PO_2. The red line is an exponential fit.

Reduced rutile phase for 0.023mTorr film

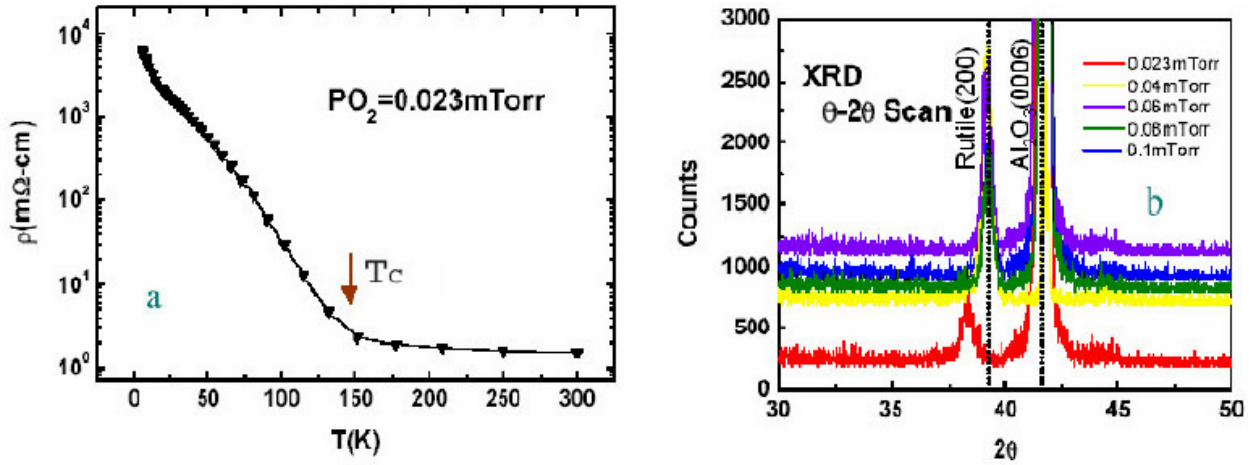

Figure 3.12 Reduced rutile observations. a) Resistivity as a function of temperature for the 0.023mTorr sample. b) XRD patterns for $TiO_{2-\delta}$: Co with various PO_2. The peak positions (200) and (400) of 0.023mTorr sample are shifted to lower 2θ angles (the shift of peak (400) is not shown here).

The lowest PO_2, 0.023mTorr, sample resulted in the maximum oxygen deficiencies in the series of samples, which was revealed by unique transport properties. The resistivity as a function of temperature of this sample is demonstrated in figure 3.12 a). At temperatures higher than $T_c \approx 150K$, the resistivity barely changed with decreasing temperature. When the temperature decreases to lower than 150K, the resistivity begins to rise steeply and keeps increasing. Similar behavior has been observed in cobalt doped rutile [30] and has been taken as an indication of the presence of the titanium dioxide Magnéli phase. The gross feature of this variation of resistivity in 3.12 a)is

analogous to the temperature induced metal-insulator transition in the Magnéli phase—a reduced rutile form of Ti_nO_{2n-1} ([108], [109]).

The Magnéli phase is found in a group of transition metal oxides. It has been of intensive interest to researchers because of its rich physical properties. In the Magnéli phase, there is a homogeneous semi-group which mainly includes titanium and vanadium compounds, showing temperature induced metal-insulator transitions. For the titanium Magnéli phase Ti_nO_{2n-1}, there are mixed valence Ti ions with 2 Ti^{3+} ions and (n-2) Ti^{4+} ions. In crystal structures, it is made of rutile-like blocks composed of chains of n TiO_6 octahedra aligned infinitely in parallel; and at the edge of two neighboring rutile block, the octaheda share their faces [108]. In the XRD pattern of reduced Magnéli phase Ti_nO_{2n-1}, the peaks are shifted slightly to lower angles compared to those of rutile crystals [48].

Overall in the titanium Magnéli phase there is a transition of metal/semiconductor to bipolaronic insulator as temperature drops. The reason is the bipolaron T^{3+}-Ti^{3+}. At high temperatures above the critical temperature, the electrons are completely delocalized and a metallic phase is defined; at T_c Ti^{3+}-Ti^{3+} bipolarons (dimers) are formed and then reordered. With bipolaron formation, charges are localized in alternate Ti^{3+} sites, resulting in an insulator. This metal-insulator transition is induced with decreasing temperature.

There is another increase in resistivity in the 0.023mTorr film below ~15K. This rise currently has no explanation in the literature and may come from reordering of the bipolarons due to the cobalt doping, which causes disorder in the rutile lattice.

Formation of titanium Magnéli phase in the 0.023mTorr film is also confirmed by XRD patterns. Figure 3.12b) shows an expanded view of the XRD patterns of $TiO_{2-\delta}$: Co films with various PO_2 in the 2θ range from 30° to 50°. The peaks at the two vertical lines are the (200) reflection of stoichiometric rutile and the (0006) reflection of the sapphire substrate. It is interesting to see that the (200) peak of the sample 2522 with $PO_2 = 0.023mTorr$, is shifted toward lower 2θ angle relative to stoichiometric rutile.

The same thing happens to the peak of the rutile (400) reflection in the same sample (also can be seen in figure 3.4). This is consistent with the formation of Magnéli reduced rutile and may also be influenced by the Co doping (see [47] and references therein).

The formation of reduced rutile in the 0.023mTorr film is not surprising because the sample was grown at the lowest PO_2. This may create enough oxygen deficiencies to form the Ti_nO_{2n-1} phase.

Evidence for multiphase structure from transport

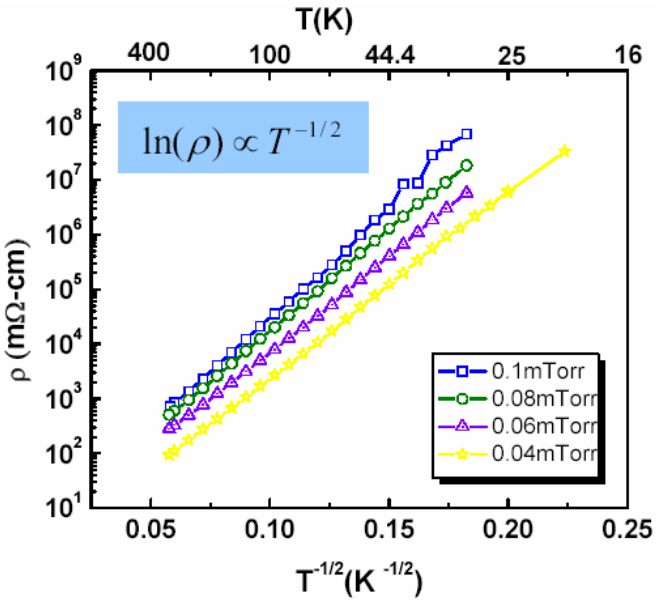

Figure 3.13 Hopping conduction. Thermal activated hopping conduction is observed for films with oxygen growth pressure higher than 0.023 mTorr.

Figure 3.13 shows transport for the other $TiO_{2-\delta}$: Co films with higher PO_2. The figure shows firstly that more resistive films result from higher PO_2 over all temperature ranges. Again this confirms that oxygen deficiencies introduce charge carriers which determine the conductivity. In addition, and more importantly, the figure indicates that the resistivity obeys a $\ln(\rho) \sim T^{-1/2}$ law over a wide temperature range from room temperature down to ~30K. This behavior looks very similar to the hopping conduction in a multiphase system composed of a dielectric matrix containing metallic granules, but differs from the correlated electron hopping between localized electronic states in a homogenious system normally encountered at temperatures below 30K

The conduction mechanism in a multiphase system of a dielectric matrix containing metallic granules was systematically studied by Sheng and Abeles ([110], [111]). As pointed out in their work, the electrical conduction in this multiphase system results from transport of charge carriers from charged grains to neutral grains. A charging energy E_c is necessary to remove an electron from a neutral grain and place it onto a neighboring neutral grain, and the product of E_c and the separation s between metallic granules is a constant, $sE_c = \text{constant}$. At low electrical field and higher temperature, the charge carries are thermally activated, resulting in hopping conductivity having the following form: $\rho \propto \exp[2(C_0/kT)^{1/2}]$, where C_0 is a constant, k is the Boltzmann constant and T is the temperature. At high electrical field and low temperature, the charges are generated by field induced tunneling; at zero temperature this results in a resistivity of $\rho \propto \exp[(C_0/\Delta l e)/E]$, where Δl is the average separation between neighboring grains in the direction of the applied electrical field, e is the electronic charge [110].

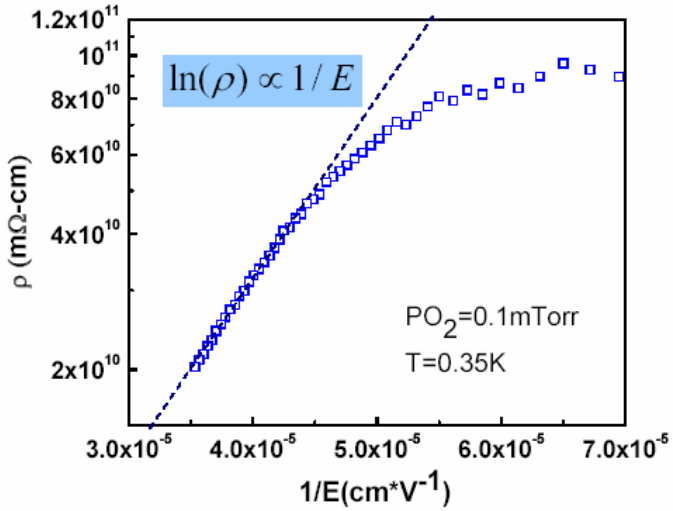

Figure 3.14 The high-field resistivity as a function of the reciprocal electrical field. This graph is a representative curve for the 0.1mTorr sample at 0.35K.

We succeeded in testing the validity of this multiphase system in the films of $TiO_{2-\delta}$: Co by observing voltage induced tunneling at very low temperatures . Figure 3.14 is a representative plot of the high field resistivity as a function of the reciprocal electrical field for the 0.1mTorr film measured at 0.35K. As can be seen, rather than a constant value, resistivity drops with higher applied electrical field, finally following the field

induced tunneling resistivity $\rho \sim \exp(C_0 / \Delta l e / E)$. Similar curves have been observed for all the other films with $PO_2 \geq 0.04 mTorr$, providing further evidence of the validity of the multiphase prediction.

It is possible to extract the average separation between cobalt granules from the slopes of the temperature and field dependence curves. For hopping conduction, the temperature dependent slope is expressed as $s_L = 2(C_0 / k)^{1/2}$. For field induced tunneling, the slope is $s_H = C_0 /(\Delta l e)$. With the resulting s_L and s_H, one can deduce the average separation between nearest clusters along one direction. Table 3.5 lists values of the deduced separations for the films. For the sake of comparison, the data for the 0.05mTorr and 0.2 mTorr films, grown at a different time, are also shown. As can be seen, most of the extracted separations are around 20nm. This is reasonable, as compared to TEM images in next section. There is a deviation for the value in the 0.04mTorr film, which has the maximum oxygen deficiency concentration of all the samples with the normal rutile structure and is consequently the most conducting. Since oxygen vacancies are crucial to induce charge carriers, the high voltage conductivity may also be affected by the large number of charge carriers even though the voltage induced tunneling conduction dominates over other possible conduction paths.

Table 3.5 Extracted cobalt granule separation from transport measurement.

PO_2 (mTorr)	0.04	0.06	0.08	0.1	0.05	0.2
Δl (nm)	61.8	20.1	17.9	18.6	21.8	18.9

Magnetotransport To further study the cobalt granules as well as other transport characteristics such as charge carriers in the films, routine measurements of the Hall Effect and magnetoresistance were made. No anomalous Hall Effect was observed in any of the films.

Overall the Hall data was noisy and it was hard to extract the carrier density. This particularly fits the situation in the higher PO_2 films with hopping conduction (for one of the cleanest Hall Effect data, see figure 3. 15a).

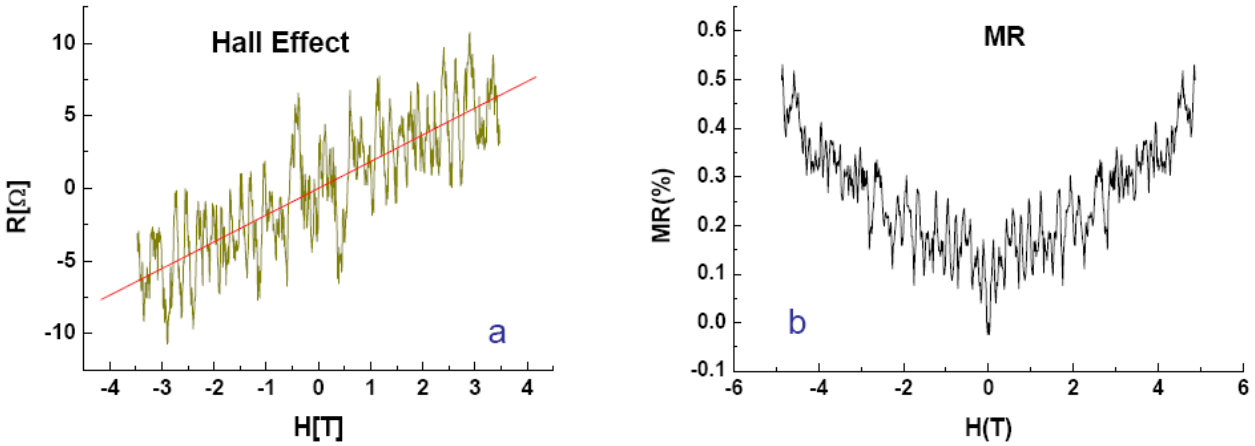

Figure 3.15 The cleanest magnetotransport data. a) shows Hall Effect of the 0.04mTorr sample at 135K after subtracting symmetrical part of the signal with magnetic field. b) is MR for the same sample at 135K after subtracting unsymmetrical signal with magnetic field. The measurements were carried out with a van der Pauw configuration.

From the best Hall signals measured, n-type carriers are detected; consistent with the assumption that the oxygen vacancies induce n-type carriers. The resulting carrier concentration (n) changes monotonically with PO_2: a higher n is associated with a lower PO_2. For the films with $PO_2 \geq 0.04mTorr$, the charge carrier concentration varies from 10^{17} to 10^{18} cm^{-3}, and the resulting carrier mobility is also low, typically lower than $2cm^2/(V*s)$. Carrier density is greatly enhanced by reducing the oxygen. The 0.023mTorr PO_2 sample has a carrier density of the order of $10^{20}cm^{-3}$ and carrier mobility of 6.8 $cm^2/(V*s)$ in the lowest PO_2 sample.

Isothermal magnetoresistance measurements were made for all the films at discrete temperatures in applied magnetic fields up to 8T. As summarized previously in chapter two, three kinds of MR have been reported in cobalt doped TiO_2 material: positive, negative and very small MR. Most of the films studied here exhibit the third kind MR. For the films with $PO_2 \geq 0.04mTorr$, the MR is noisy with a very small positive value at temperatures from 5K to room temperature (see figure 3.15 b). The highest value measured is 2%. This is reasonable, if we consider the film composition: a $TiO_{2-\delta}$ dielectric matrix and cobalt clusters forming a multiphase system in which hopping conduction is the main form of transport at low electric fields. For the more conductive 0.023mTorr sample, a cleaner MR signal was observed at lower temperatures. At

4.22K, a positive 6% MR was observed, and at 2K, the MR reached to +17% (see figure 3. 16).

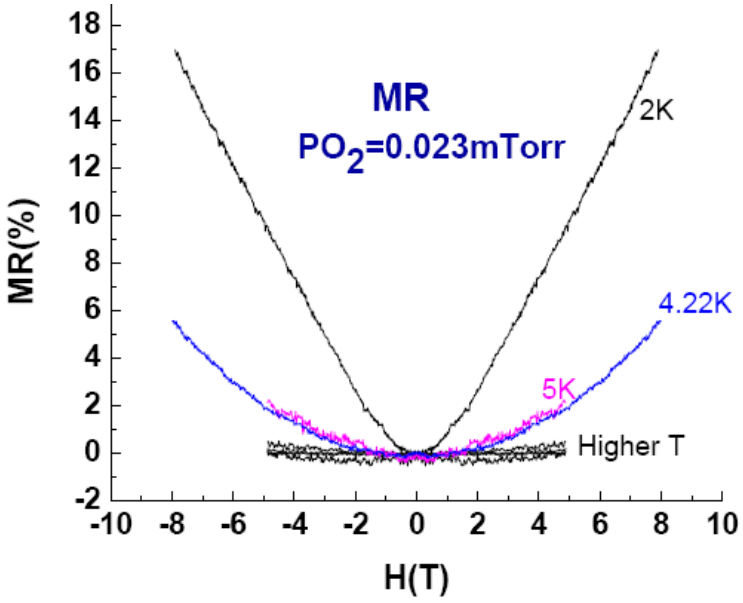

Figure 3.16 Isothermal MR for the 0.023mTorr sample at various temperatures from 2K to 295K. A small intrinsic MR of a cernox thermometer may contribute to the MR at 2K.

3.5 Microstructure properties

3.5.1 Experiment

Samples are prepared for TEM. TEM sample must be thin and polished enough that electron beams can be transmitted through them. For the cross-sectional view, two narrow strips are cut from the sample. The two strips are then glued together with their film sides facing using a particular kind of glue which is transparent under electron beam iradiation. After the glue dried, the sample was ground and polished.. Then the resulting polished side was glued on a copper grid. Again after the glue was dried overnight, the other side of the sample was ground and polished until the sample is thinner than 50 μm and ready for ion-milling. The ion-milling process will result in a very tiny hole around which the sample has gradient thickness for TEM measurement.

High resolution transmission electron microscopy, HRTEM, is a powerful tool to observe the microstructure on atomic scale. With the aid of the EDS, it is capable of determining

the elemental components in a small area. Selected Area Diffraction can be performed to explore the crystal structure of a particular point. Thus it provides an important tool to look at the small Co clusters in thin films of Co doped TiO_2.

3.5.2 Results and discussion

From TEM measurement, cobalt clusters were observed in all of the samples in the cross-section view. The resulting images look very similar for the films over this small range of $0.023 \le PO_2 \le 0.1 mTorr$. A representative cross-section view is shown in figure 3.17. The roughness of the film on the film surface and the smoothness of substrate surface can be observed here, in agreement with the results from profilometry and light microscope.

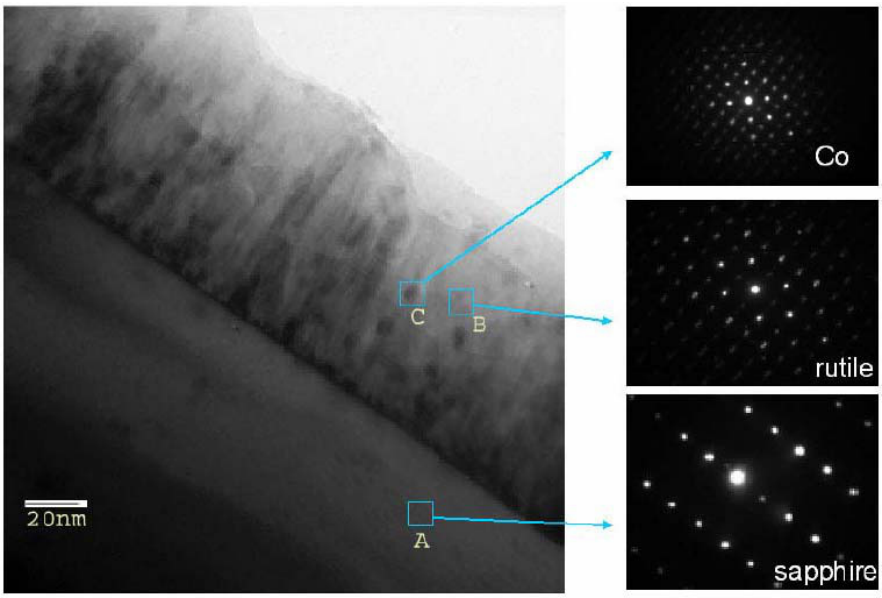

Figure 3.17 TEM image. A representative cross-sectional image of the 0.04mTorr film under TEM is demonstrated with SAD determined sapphire, rutile and cobalt areas.

In figure 3.17, three areas, labeled as A, B, and C are highlighted. The magnification is x500K. The clear straight line is the interface between the film and the sapphire substrate, which verifies the smooth surface of the substrate. The light uniform area below the line is the substrate with a sapphire crystal structure, as confirmed by the SAD pattern. The lightly shaded area B is found to be rutile. It can be seen that the rutile

has grown in a manner of columns perpendicular to the interface, which happens in all the films. Again, as determined by SAD, the dark dots (area C) were found to have the bulk fcc cobalt crystal structure. Thus the cobalt is precipitated out of the TiO_2 lattice as cobalt nanoparticles in the films. The clustering of cobalt is also confirmed with energy dispersive spectroscopy (EDS) which measures the elemental composition. From EDS measurement, the area B contains almost no cobalt, while over 90% of the composition of area C has been identified as elemental cobalt.

Besides the cobalt clusters in the films, there is also a layer of intensive small cobalt clusters at the interface between the film and the substrate. This is not surprising. Since the lattice mismatch between rutile TiO_2 and sapphire is 4.2%, there should be large numbers of defects at the interface, and the defects promote diffusion of cobalt dopant; resulting eventually in small cobalt clusters at the interface [112].

The cobalt cluster size averaged over individual TEM images are approximately 8nm for all the films. This is also consistent with the values derived from previous magnetic measurement. However, since there is a large distribution of the particle diameters within a given film, it is hard to draw precise conclusion of the relationship between cobalt size and the PO_2.

3.6 Conclusion

$TiO_{2-\delta}$: Co thin films are grown by PLD at various oxygen pressures PO_2. The structural, magnetic and transport properties of the resulting samples are studied and correlated wherever possible with the magnitude of PO_2. Within the particular PO_2 range studied, cobalt clusters are observed in all the samples. Magnetic properties are dominated by nanometer size Co particles, and indicate that lower PO_2 results in smaller cobalt naoparticles. Transport measurement show two kinds of conduction mechanisms. With PO_2 higher than 0.04mTorr, the samples show a thermally activated hopping conduction, which is consistent with low temperature (0.35K) voltage activated tunneling transport. The lowest PO_2 of 0.023mTorr results in a structure related to rutile, the reduced rutile Magnéli phase as confirmed by x-ray spectroscopy. This results in very

different transport properties, with no observation of either hopping conduction or field induced tunneling conduction. Overall the magnetoresistance is very weak above 4K for all the samples. TEM measurements have verified the clustering of the cobalt. Thus the role of oxygen deficiencies is determined to affect the nonstoichiometry of the material and induces n-type charge carriers, resulting in more conducting films compared to films grown at lower PO_2. Furthermore the oxygen defects assist the precipitation of cobalt particles during film deposition.

To summarize, our work in the oxide system $TiO_{2-\delta}$: Co shows strong evidence of cobalt clustering, which accounts for the ferromagnetic signature at room temperature and dominates the magnetic behavior. The multiphase material also results in a characteristic $\ln(\rho) \propto T^{-\frac{1}{2}}$ dependence indicating a type of hopping conduction as well as field induced tunneling. Thus, even though RTFM has been reported by many researchers in transition metal doped oxides, our work, at least in $TiO_{2-\delta}$: Co,confirmes that the structure is a mixture of phases, particularly when grown at low PO_2. The controversy over the issue of cobalt segregation points towards the necessity for detailed structural and transport characterization to understand the nature of oxide based DMS films.

CHAPTER 4

$SnO_{2-\delta}$: Co

4.1 Introduction

As summarized in chapter two, the ferromagnetism of SnO_2 doped with many kinds of transition metals such as Co, Mn, *etc.* has been predicted and observed in the literature ([77]-[91]) with some quandaries, such as the origin of the RTFM, etc. In chapter three, our detailed characterization shows evidence for the occurrence of cobalt clusters, in comparison with the reported work on TiO_2: Co; it also suggests that detailed characterization such as structural and transport is necessary to examine the nature of the RTFM.

The ionic radii of Co^{2+} and Sn^{4+} in octahedral coordination are 0.72 Å and 0.71Å, respectively. Compared to the ionic radius of Ti^{4+} of 0.68Å, the very similar values of the ion radii between Co^{2+} and Sn^{4+} may result in an easier substitution of cobalt into the tin sites in the SnO_2 lattice, potentially leading to an intrinsic DMS, $Sn_{1-x}Co_xO_{2-\delta,}$ for further spintronics research and application.

4.2 Experimental Description

$SnO_{2-\delta}$: Co thin films were grown by PLD. For this work the Co molar concentration in the target was 5%. The substrate for growing $SnO_{2-\delta}$: Co is r-sapphire. A Phillips 4-circle X-ray diffractometer was utilized to examine the crystallinity of the films. A Princeton Measurements Alternating Gradient Magnetometer (AGM) was used to measure the magnetic properties at room temperature, and a Quantum Design SQUID was used for low temperature magnetic measurement. For microstructure analysis, samples were prepared cross-sectional and measured by TEM. Resistivities were measured via a

conventional van der Pauw technique, with indium contacts for low temperature measurements, and needle probe contacts for room temperature measurements.

4.3 Initial Characterization

Our initial studies of the $SnO_{2-\delta}$: Co films focused on the structural part, concerned with the possibility of cobalt clustering as well as the overall crystallinity.

Although the crystalline quality varies with growth conditions, rutile crystal structure was always detected by XRD. A representative XRD pattern is shown in figure 4.2. The resulting $SnO_{2-\delta}$: Co films are single phase of primarily (101) oriented rutile.

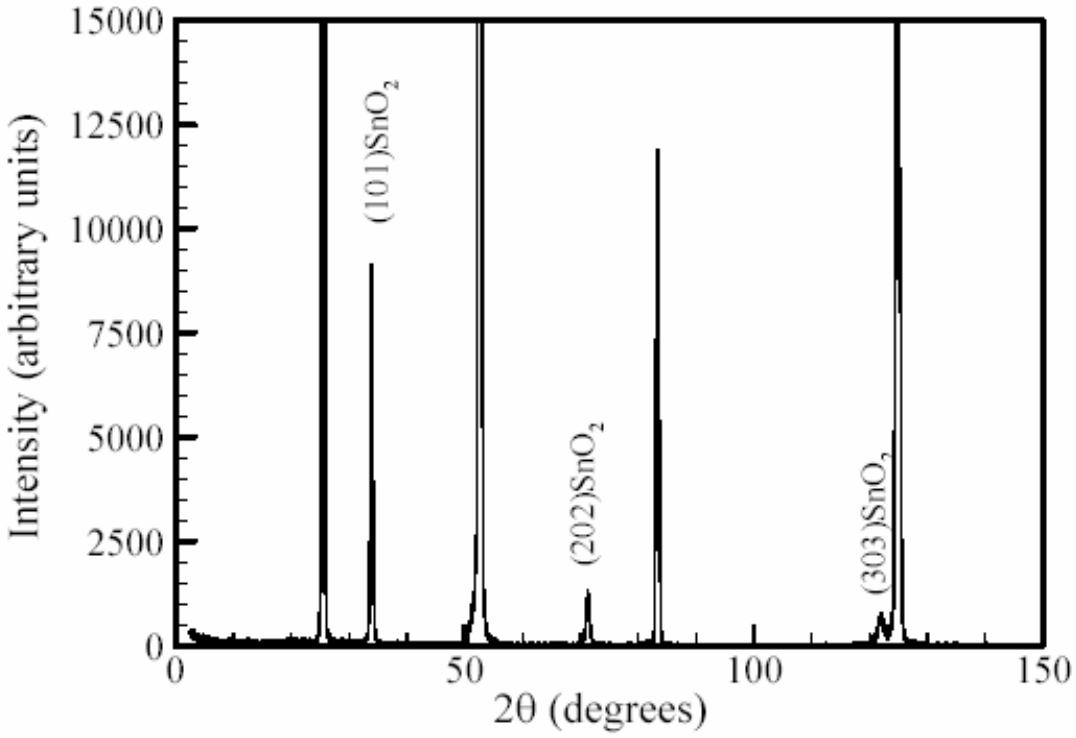

Figure 4.1 X-ray diffraction patterns of $Sn_{1-x}Co_xO_2$ thin film deposited on r-cut sapphire. The unlabeled peaks are diffractions from the sapphire substrate.

TEM studies on cross-sectional $SnO_{2-\delta}$: Co specimens indicate that there are no cobalt clusters which can be observed even at the sub-nanometer scale. Figure 4.2 a) shows a representative TEM image. It can be seen that the film growth is primarily columnar

perpendicular to the interface (for the samples with relatively poor crystallinity, the film growth is in grains rather than in columns). Although some dark areas are present in the image, they are not cobalt clusters but grains of $SnO_{2-\delta}$: Co, as determined from the elemental composition analysis by EDS.

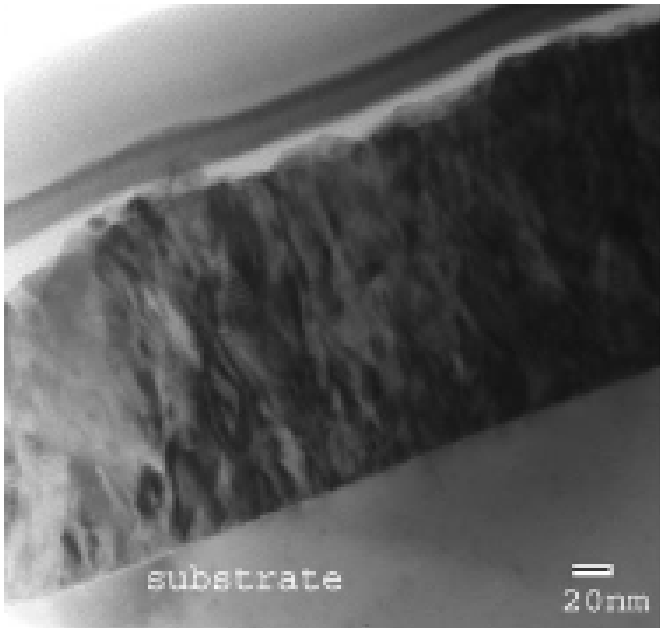

Figure 4.2 Representative microstructure of $SnO_{2-\delta}$: Co films from TEM. Here S is for the sapphire substrate. The straight line is the interface between substrate and the film.

Via EDS one can also determine the cobalt concentration. As determined by EDS, the cobalt content in $SnO_{2-\delta}$: Co films is in general ~10%, higher than the nominal 5% as in the target. That the Co concencentration in the deposited $SnO_{2-\delta}$: Co films is higher than that in the corresponding target has been reported previously. A very possible reason is the loss of tin by evaporation during film deposition, due to the low vapor pressure of tin. Although the tin evaporates preferentially, there are no cobalt metal clusters formed in the films.

Since there is no phase segregation in $SnO_{2-\delta}$: Co detected from the initial characterizations, this material may represent a true uniform DMS, and it may have potential application in Spintronics. In the following section, 4.4, the results obtained on this material so far will be presented and discussed.

4.4 Results and Discussion

The physical properties of the films of $SnO_{2-\delta}$: Co are studied in detail as a function of growth rate, temperature, and morphology.

4.4.1 Growth Condition Issue

$SnO_{2-\delta}$: Co films were grown at varying substrate temperatures, oxygen pressures and growth rates for search of optimum growth condition to gain a DMS. Below the effect of growth conditions on physical properties will be discussed.

4.4.1.1 Substrate Temperature dependence

It was discovered that the magnetism of the films depends on the substrate temperature during film deposition. There is a temperature range over which magnetism is obtained, and the optimum substrate temperature for growth of most magnetic films was found to be $T_s \cong 720^o C$.

4.4.1.2 Oxygen Pressure dependence

The oxygen growth pressure (PO_2) also determines the properties of the films. $PO_2 = 1mTorr$ results in optimum film growth. At low PO_2, films are non-magnetic and the crystallinity is poor. Films grown at high PO_2 are found to be non-magnetic as well and insulating.

4.4.1.3 Growth rate dependence

The growth rate was mainly controlled by the repetition rate of the laser pulse during film deposition.

High growth rate At the highest growth rate of 10Hz, the cobalt concentration at various points in the film is the most inhomogeneous and the relative increase in cobalt

concentration over that of the target is small. As would be expected, the high growth rate resulted in thicker $SnO_{2-\delta}$: Co film, compared to the other films deposited with the same product of growth rate and growing time; this is probably due to less evaporation of Sn atoms during shorter growth time. The films show simple activated semiconducting ρ vs. T behavior, not hopping behavior [35].

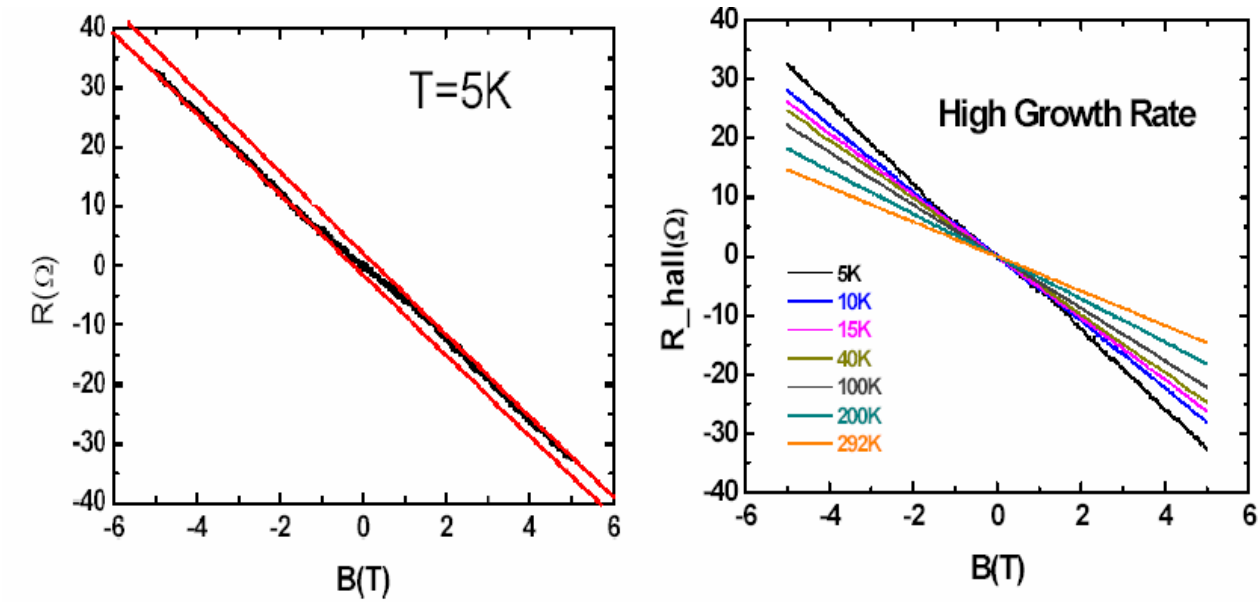

Figure 4.3 Hall Effect for the samples at high grow rate.

A small Anomalous Hall Effect (AHE) is observed at low temperatures. As shown in figure 4.3, a slight AHE at 5K supports possible intrinsic ferromagnetism in this material. The graph on the right in figure 4.3 shows isothermal Hall measurement at various temperatures, wherein only the normal Hall Effect is observed at temperatures higher than 10K. Carrier concentrations of $n = 2 \sim 4 * 10^{18} cm^{-3}$ and mobilities of $\mu = 13 \sim 16 cm^2 / V * s$ were obtained in this sample with higher values of n and μ at higher temperature from 5K to 300K.

A monotonically negative magnetoresistance was observed for samples with high growth rate, as seen in figure 4.4. Similar MR has been reported in literature. The negative MR comes from the alignment of the electron spins by an applied magnetic field.

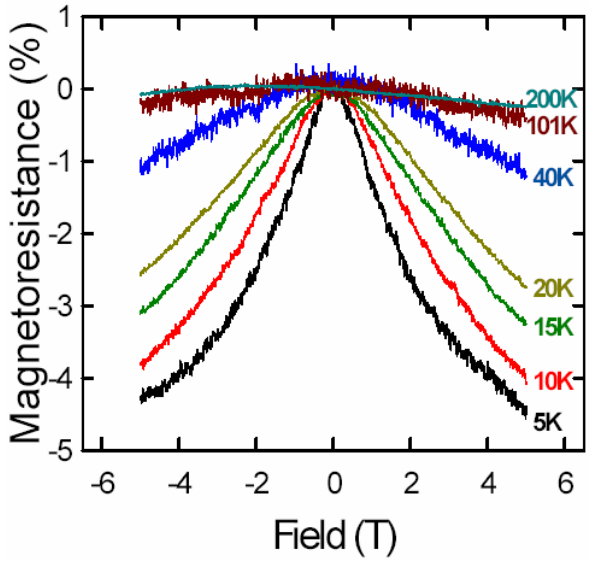

Figure 4.4 Negative magnetoresistance in $SnO_{2-\delta}$: Co. The film is deposited with high laser pulse frequency.

Low growth rate For those films grown at a lower rate of 3Hz, a better crystallinity was found, as determined by X-ray structural and cross-sectional TEM measurements.

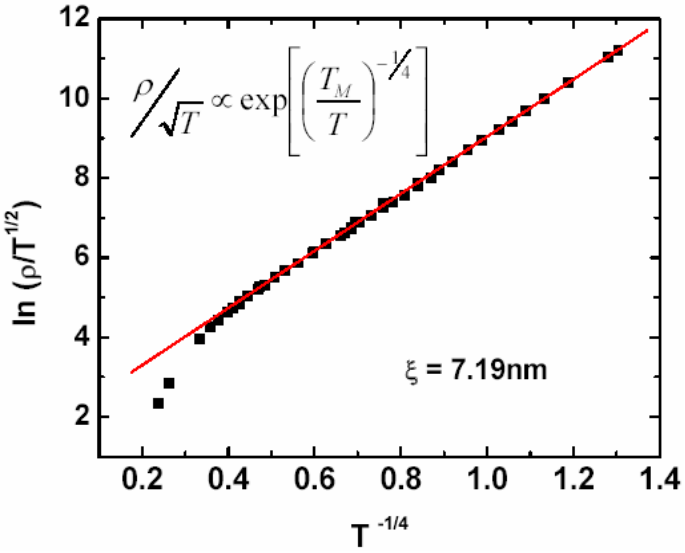

Figure 4.5 Mott's VRH are observed in samples at 3Hz growth rate.

The films at 3Hz growth rate also presented unique transport properties. As a reminder, the $\ln(\rho) \propto T^{-1/2}$ behavior of the $TiO_{2-\delta}$: Co films indicate an intergranular hopping conduction [35], which was confirmed with the observation of cobalt clusters by TEM and magnetic ZFC-FC in the films. For the $SnO_{2-\delta}$: Co films, the resistivity does not

show the characteristic $\ln(\rho) \propto T^{-1/2}$. Instead, the Mott variable range hopping law (VRH) of $\ln(\frac{\rho}{\sqrt{\rho}}) \propto T^{-1/4}$ was observed by fitting the resistivity as a function of temperature. An example of the observation of VRH is demonstrated in figure 4.5. By fitting the resistivity curve, a localization length of 7.19nm (see figure 4.5) was deduced.

For the low growth rate, 3Hz, samples, the Hall Effect is difficult to measure due to hopping conduction.

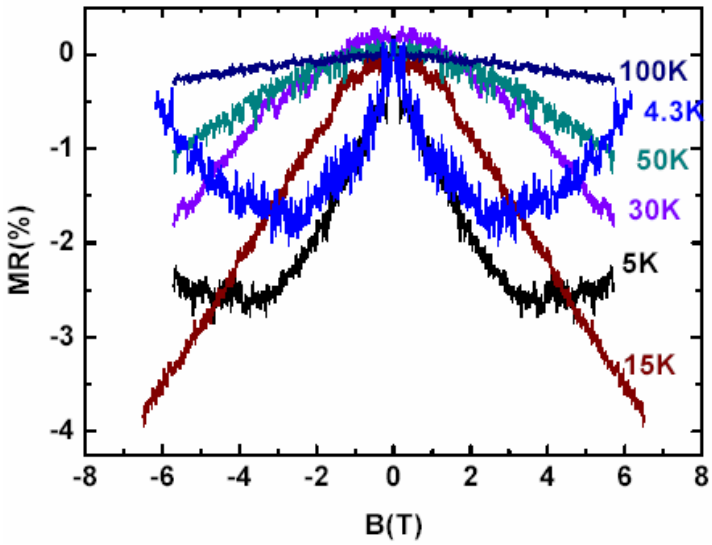

Figure 4.6 Isothermal MR at low temperatures. This phenomenon is associated with the VRH behavior of resistivity.

A turnover of the MR at low temperatures was observed in the low growth rate samples associated with VRH. As shown in figure 4.6, the MR is negative at low field up to H_{kink}. With higher applied field than H_{kink}, the MR exhibits a positive slope. H_{kink} decreases at lower temperatures. Similar MR has been observed in Co doped $SnO_{2-\delta}$ [83] and transition metal doped ZnO ([57], [62], [66]-[67]). Considering the observation of VRH which indicates the extent of the localized wave function of the charge carriers, the MR behavior can be understood as follows. There are two effects of the magnetic field on the electron waves. One is the field-enhanced spin alignment effect, which results a negative MR. On the other hand, from classical considerations, a strong magnetic field will result in a shrinkage of the localized electron wave, causing a higher hopping

resistivity. Thus there exists the kink in the MR at low temperatures. At higher temperatures, thermal fluctuations are stronger, which weakens the shrinkage of the wave function due to strong magnetic field. Thus the H_{kink} increases at higher temperature and when $T > 15K$, only negative MR can be observed.

Mott-type VRH This variable range hopping behavior happens on the insulating side of the metal insulator transition where the Fermi energy E_F is smaller than the mobility edge E_c. In a disordered system, electrons could be localized in some specific region, compared to the extended states where the electron wave function extends throughout the whole material. As one approaches the MIT from the insulating side, the localization radius increases rapidly, and diverges at the transition point to form extended states [114]. In the presence of impurities, the density of states has a tail where the states are localized (the shaded area in figure 4.7). The energy E_c is called the mobility edge, which separates the extended states and the localized states.

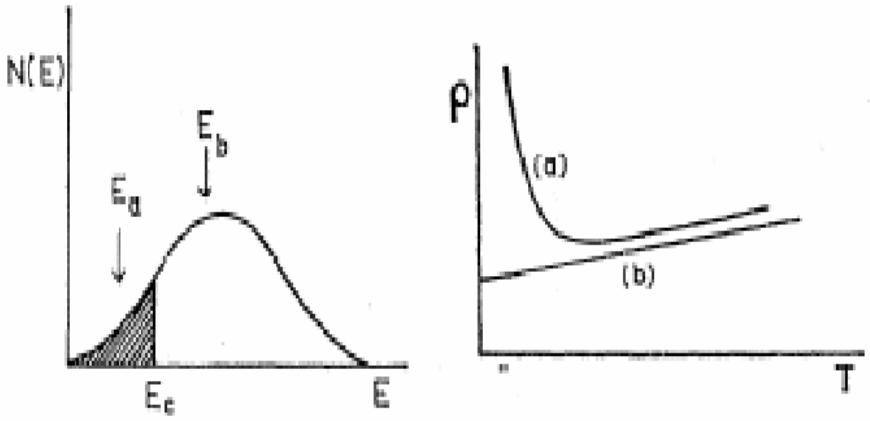

Figure 4.7 Mott-type VRH. The left graph show a density of states as a function of E_F. The right figure shows the resistivity curves $E_F = E_a$ and $E_F = E_b$ (after Ref. 114).

Conductivity of the system at zero temperature is mainly dominated by carriers near the Fermi energy (E_F). When $E_F > E_c$, the electrons are in extended states, transport is dominated by normal band conduction, and the system is metallic (curve b in figure 4.7); when $E_F < E_c$, the transport is dominated by electron hopping from one localized state to another with the aid of phonons (curve a in figure 4.7) and a Mott-type VRH conduction may dominate transport. The formula for VRH is:

$$\rho(T) \propto \sqrt{T}\exp[(T_M/T)^{-1/4}] \text{ with } T_M = 18/k_B L_V{}^3 N(E_F) \text{ [115]},$$

where L_V is the localization length and N (E_F) is the density of states at the Fermi energy.

Intermediate growth rate At the intermediate growth rate of 5 Hz, the samples showed ρ vs. T curve with a peak at low temperature. A representative curve of the resistivity as a function of temperature is shown in figure 4.8 a). Figure 4.8 b) shows the values of carrier concentration and mobility. The charge carriers are n-type electrons, as determined from isothermal Hall Effect measurement. As shown in the graph, both n and μ change abruptly at ~10K, and tend to be constant at higher temperatures. This behavior is not, as yet understood and will require further study.

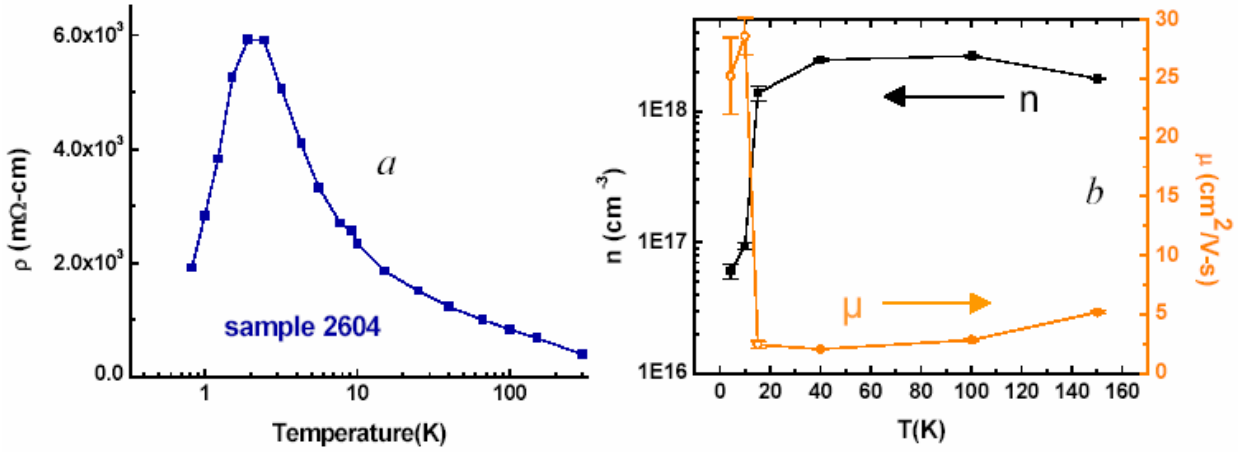

Figure 4.8 Transport of the $SnO_{2-\delta}$: Co film at the intermediate growth rate of 5Hz. a) ρ vs. T. b) Temperature dependence of carrier concentration (n) and carrier mobility (μ), the values are determined from isothermal Hall Effect measurements.

Target treatment effects It was found that target treatment was critical: after the target was left in vacuum for two weeks, inconsistent results were obtained on all films grown subsequently. Also, the film growth rate decreased rapidly as a function of depth into the target, indicating some change in the target as a function of total growth time. This suggests that for consistent results, it is not only necessary to be able to consistently reproduce growth conditions, but that the target needs to be changed out frequently.

To summarize the growth condition effects, a significant result of this work showed that there does indeed exist a window in the substrate temperature and oxygen pressure phase space where magnetism can be observed.

4.4.2 Magnetic properties as a function of film thickness

Although the physical properties of the films during search of optimum growth condition varied widely, further work on films with identical optimum growth condition showed consistent and promising intrinsic ferromagnetism and other consistent results.

Films were grown at identical conditions but for varying growth times, resulting in films with varying thickness. The following studies are on these samples.

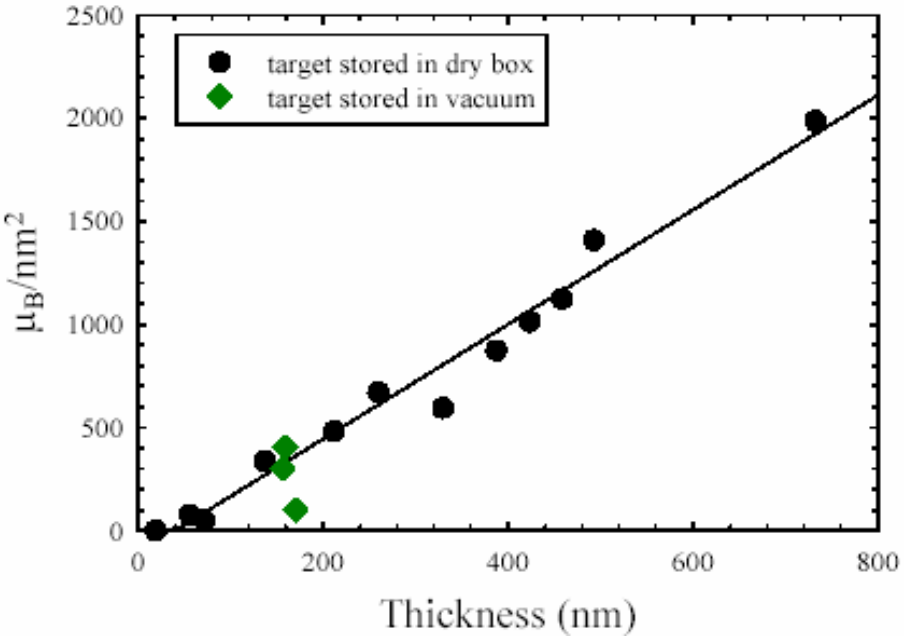

Figure 4.9 Normalized moment per unit area of film surface as a function of film thickness. There is a clear linear trend.

The magnetic moment as a function of film thickness can provide further evidence that the ferromagnetism is intrinsic and not caused by surface state impurities. The growth parameters are: optimum T_s of 720°C, optimum PO_2 of 1mTorr, and laser frequency of 3Hz. The moment normalized per unit area (see figure 4.9) shows a linear dependence on thickness, indicating a constant magnetization for the films, even for films grown on

different days. This is in direct contrast to results published by other groups in which there was no clear thickness dependence, leading to the speculation that impurities or surface states were the cause of the magnetization in these films [82]. In contrast our data suggest an intrinsic origin for the ferromagnetism in these carefully controlled materials. The green dots in the figure show films which were grown using the target that was stored in the vacuum chamber for an extended period. The locations of the green dots are perhaps due to a changed oxygenation state in the target. In general, after being stored in vacuum the magnetization was severely reduced. This highlights the importance of growth conditions and target control to obtaining consistent results.

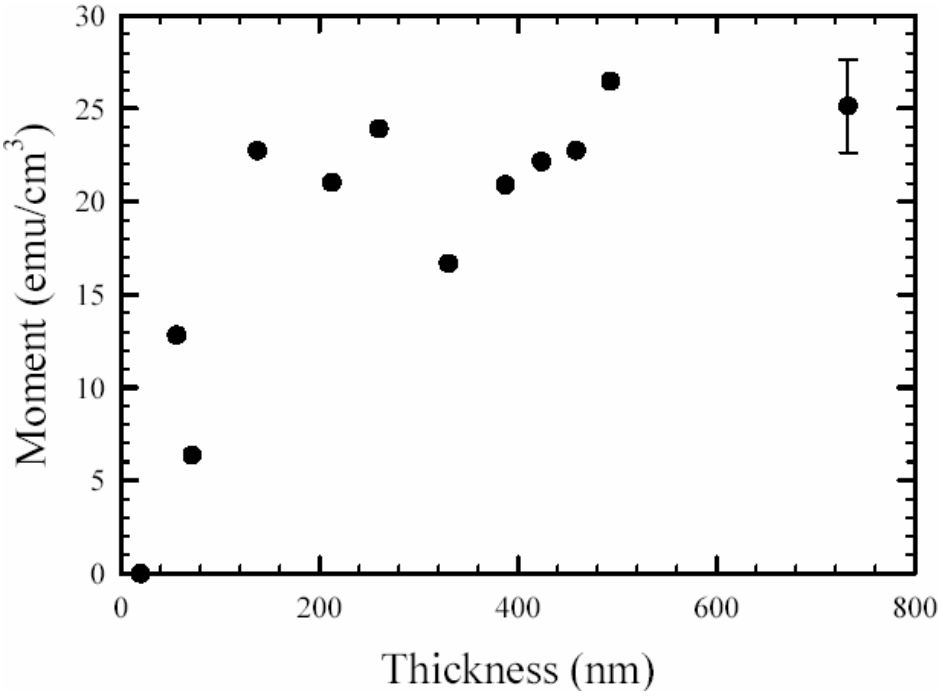

Figure 4.10 Moment as a function of thickness for films of various thickness but with identical growth conditions.

Figure 4.10 shows the thickness dependence of the moment normalized per volume for the same group of samples. Clearly for films thicker than 100nm, the normalized moments agree with one another within error. This provides further support for the intrinsic ferromagnetism. Transport measurements showed, furthermore, that these magnetic samples also have measurable resistivities, *i.e.* charge carriers may mediate the ferromagnetic coupling.

4.4.3 Electrical transport

From figures 4.9 and 4.10 it can be seen that films with thickness less than 100nm have a smaller moment than thicker films. As shown in figure 4.11, films thinner than 100nm are also insulating, while for films thicker than 100nm, the resistivities vary from ~150-3000 mΩ-cm with no clear thickness dependence. As can be seen dramatically, all of the thin film samples in which the moment decreases precipitously are insulators, while those with a thickness above 100 nm are more conductive with a measurable resistivity However, the absolute magnitudes are not easily correlated with the thickness measurements.

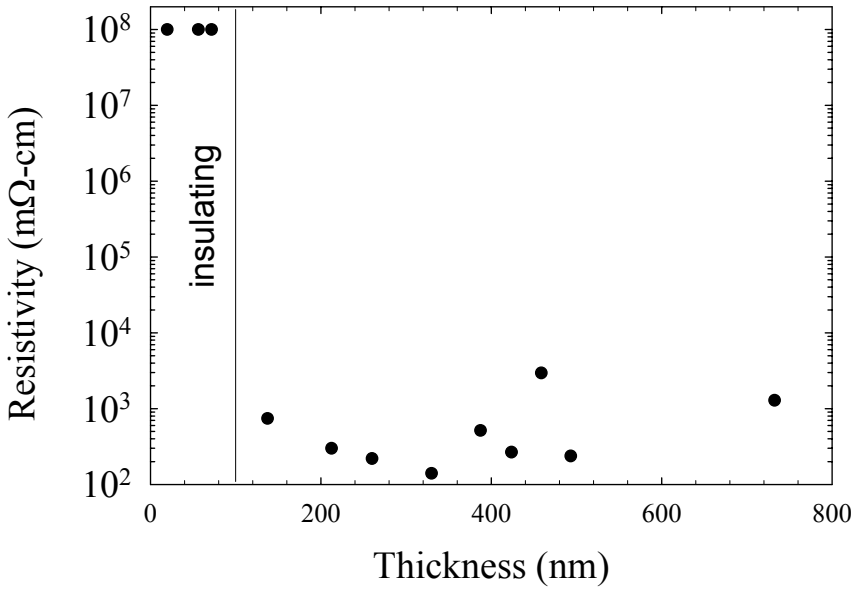

Figure 4.11 The room temperature resistivity plotted as a function of film thickness.

Since SnO_2 is well known to have transport properties strongly sensitive to gas absorption, it is likely that for very thin films, the films are completely oxygenated during the cool-down process in the growth chamber. The slight variations in resistivity for the thicker films could be a result of fluctuations in the amount of oxygen absorption during the cool down process. It is interesting to note that for this series of films, we strictly controlled all sample preheat and cool down times to agree within seconds from film to

film, yielding much more consistent results than for the series of films described in the previous section, 4.4.1, wherein growth temperature and oxygen pressure were varied in order to determine the optimum growth conditions.

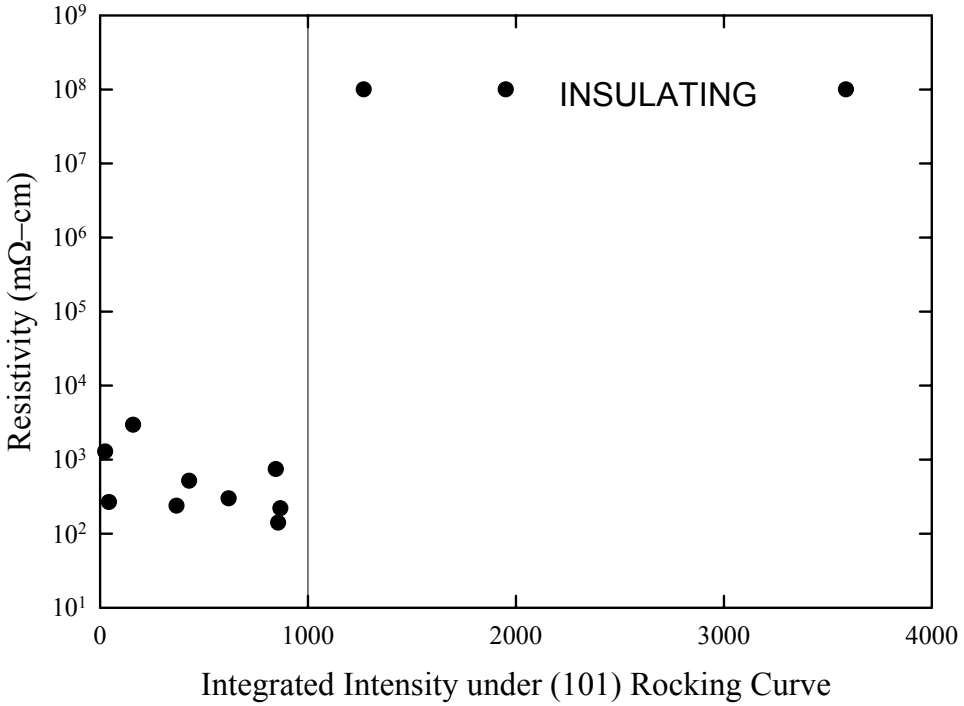

Figure 4.12 Room temperature resistivity of the films plotted as a function of the integrated intensity under the (101) x-ray reflection of the SnO_2 films.

Figure 4.12 shows the resistivity for the conducting films plotted as a function of the integrated intensity of the rocking curve of the principal (101) reflection of the rutile structure. The integrated intensity is a direct measure of the crystallinity of the film: the bigger the integrated intensity, the better the crystallinity. Apparently there are two regions in figure 4.12: separated by the solid line. On the left of the perpendicular line, films have relatively bad crystallinity and the corresponding resistivity magnitudes are measurable. On the right of the line, the crystallinity is better, but the films are too insulating to measure (the value of 10^8 is just to indicate our inability to measure larger magnitudes with confidence). Thus the insulating films have the best crystal structure. This is not surprising. SnO_2 is conductive and this conductivity is believed to originate from native defects resulting from the nonstoichiometric compositions of the material, *i.*

e. oxygen vacancies and/ or interstitial tin ions. With low crystallinity, there are more oxygen vacancies and the system is more conducting than on the right side of the line in which the crystallinity is more perfect and the defect density low.

4.4.4 Effects of Annealing

As mentioned earlier, if E_F is properly controlled crossing E_c in figure 4.7, the wave function of the charge carriers can possibly transit from localized states to extended states, leading to a insulator to metal transition (MIT). As the low growth rate samples showed Mott VRH transport, which is on the insulating side of this transition, it should be possible to "reduce" our $Sn_{1-x}Co_xO_{2-\delta}$ films and to drive the samples from insulating to metallic. For this purpose, we tried to anneal our samples in either N_2 flow or vacuum at various temperatures and for various times.

Trial annealing has been performed in a furnace in the same PLD chamber used for sample growth. Characterizations are performed on the $SnO_{2-\delta}$: Co films before and after annealing. X-ray diffraction was used to compare the crystal structure. A room temperature vacuum probe station with a Keithley source meter and a multimeter were used to check the resistivity at room temperature. Magnetic properties were also measured.

After annealing in N_2 at high temperature (900°C), most of the defects were eliminated. XRD showed great enchancement of the crystallinity after annealing. The intensity of the rocking curve was increased by a factor of ~3, and the FWHM shrunk from 1° to 0.4°. Consequently and consistent with the correlation between crystallinity, magnetic moment and conductivity, it was found that the annealed film is insulating, compared to 749.8 mΩ-cm before annealing; and the magnetic signal is almost gone after annealing, as in figure 4.13. The color of the sample also turned clear after annealing, indicating the elimination of defects and the perfection of the crystallinity brought about by anneal. As the film crystallinity was perfected when annealing at high temperature, it seems like that the defects in the $SnO_{2-\delta}$: Co films cause the magnetism and conductivity of the films.

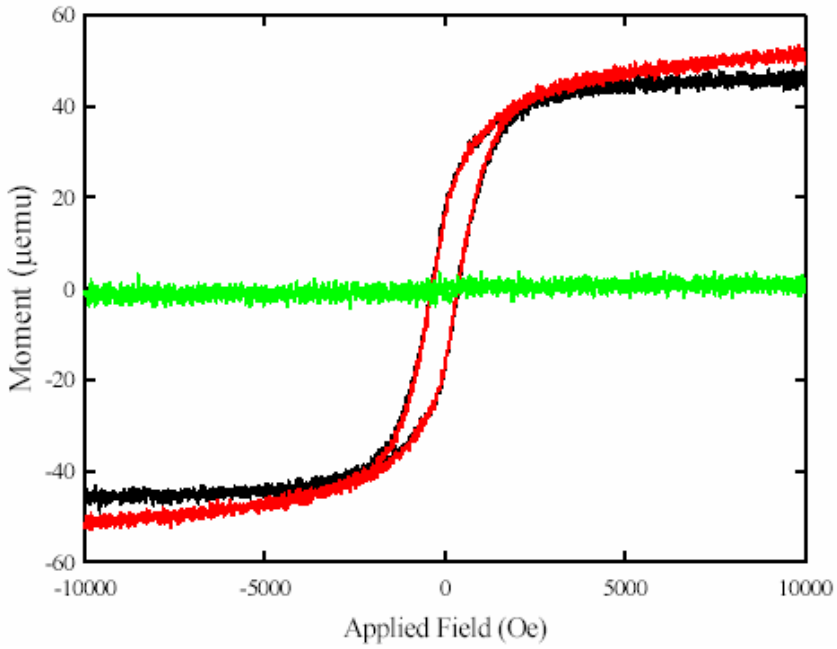

Figure 4.13 Magnetic curves M vs. H before and after anneal. The black and red curves are measured before anneal; the green one is for after anneal.

Our experience of thermal treatment on the $SnO_{2-\delta}$: Co films at lower temperatures than T_s (the substrate temperature during film deposition by PLD) in vacuum showed no effect on the films physical properties of magnetic, transport, crystallinity, *etc*.

Thus there exists a critical window of annealing temperature, which is close to T_s, to effectively reduce the films and achieve an MIT.

It turns out that for annealing at intermediate temperatures, the effect depends on the growth temperatures. What we learned from an annealing in N_2 at 750° for various time is as follows. For samples with higher T_s, annealing for less than 10 minutes significantly enhanced the ferromagnetism without too much change of conductivity; further annealing for longer time suppresses both. For samples with lower T_s, the ferromagnetism is enhanced within the first 15min, then saturates. There is not much change in the conductivity during the whole annealing process. Overall the magnetization is very sensitive to the annealing time. The enhancement and suppression of the ferromagnetism with time suggests that annealing induces defects in $Sn_{1-x}Co_xO_{2-\delta}$ at least through two processes containing variation of two kinds of defects:

oxygen deficiencies and Co interstitials. The complicated physical processes caused by annealing have been reported in the diluted magnetic semiconductor $Ga_{1-x}Mn_xAs$ [116].

4.5 Conclusion

Thin films of $SnO_{2-\delta}$: Co are deposited by PLD with various growth parameters. The films are studied for their structural, magnetic, and transport properties. Many interesting phenomena have been observed.

$SnO_{2-\delta}$: Co films have no observable Co clusters by TEM, which may indicate that the Co ions enter the matrix substitutionally.

The transport properties are studies as a function of growth rate. A variable range hopping transport of $\rho/\sqrt{T} \propto T^{-1/4}$ is observed on those samples with a low growth rate of 3Hz. This suggests that these samples just lie on the insulator side in the vicinity of the metal-insulator transition. A turnover of MR, from a negative MR at low applied magnetic field to a positive MR at high field, is observed for the samples at low temperatures. For the high growth rate samples, small AHE and negative MR are observed

With optimum T_s and PO_2, and careful duplication of growth conditions more consistent results are obtained. All the samples are ferromagnetic at room temperature. The magnetism is verified to originate from intrinsic bulk rather than surface effects. Film crystallinity also has a crucial effect on the magnetic moment and conductivity, indicating that defects in the material plays an important role in the magnetism as well as transport.

CHAPTER 5

CONCLUSIONS

Cobalt doped TiO_2 has been studied as a potential DMS after the observation of RTFM in this material [12]. However, there have been controversies on whether there exists the presence of the secondary cobalt metal phase. Growth methods and growth parameters are thought to determine the physical properties of the resulted films of TiO_2 with Co doping. In this thesis work, we studied the growth oxygen pressure, PO_2, effects on the properties of the films.

Rutile $TiO_{2-\delta}$: Co thin films were deposited by PLD technique, and have been systematically studied for the effect of oxygen pressure during growth on the physical properties of the films. Characterization of magnetic, transport, and structural properties were carried out. Magnetic behavior is dominated by the cobalt dopants. Room temperature coercivities have a dependence of PO_2 similar to the variation of Hc with particle size crossing a transition from superparamagnetic to single domain (non superparamagnetic) particles. Transport was found to be via hopping conduction and electrical field induced tunneling conduction in a multiphase material consisting of a dielectric matrix containing metallic grains. It turn out that the cobalt precipitates out as cobalt clusters within the studied PO_2 growth range. The cobalt nanoparticles size was affected by PO_2.

For an ideal DMS, the ferromagnetism has an intrinsic origin. It requires high carrier concentrations to mediate the collective magnetic behavior of magnetic impurities. In the $TiO_{2-\delta}$: Co system, oxygen vacancies are usually thought to provide carriers, in agreement with our results. However oxygen vacancies also accelerate the Co atoms' diffusion to form Co clusters. Thus it is very hard to obtain an intrinsic ferromagnetic in semiconducting $TiO_{2-\delta}$: Co.

Laser ablated rutile $SnO_{2-\delta}$: Co thin films were also studied. No cobalt clusters were observed. It was found that growth condition strongly affects the physical properties, and a group of optimum growth conditions were developed. In particular, as a function of laser pulse rate during growth, various transport and magnetotransport properties were observed. Ferromagnetism was found to originate from bulk rather than surface or interface effects. A correlation between saturation magnetization and conductivity were also found. Effective annealing of $SnO_{2-\delta}$: Co films was realized in a narrow temperature range and is very sensitive to the environment. To summarize the work on $SnO_{2-\delta}$: Co, very possibly it has intrinsic ferromagnetism, which makes it a potential DMS and of interest for future spintronics utilization.

REFERENCES

1. G. E. Moore, Proc. IEEE, **86**, 82 (1998).

2. R. P. Feynman, "There's Plenty of Room at the bottom." Talk given at the Annual Physics Society meeting, Pasadena, CA, December 26th, 1959.

3. S. A. Wolf, D. D. Awschalom, R. A. Buhrman, J. M. Daughtom, S. von Molnár, M. L. Roukes, A. Y. Chtchelkanova, and D. M. Treger, Science **294**, 1488 (2001).

4. D. D. Awschalom, M. E. Flatté and N. Samarth, Scientific American, **286**, 66 (2002).

5. M. N. Baibich, J. M. Broto, A. Fert, F. N. Vandau, F. Petroff, P. Eitenne, G. Creuzet, A. Friederich and J. Chazelas, Phys. Rev. Lett. **61**, 2472 (1988).

6. M. Oestreich, Nature, **402**, 735 (1999).

7. T. Dietl, Semicond. Sci. Technol. **17**, 377 (2002).

8. H. Ohno, Science, **281**, 951 (1998).

9. A. Haury, A. Wasiela, A. Arnoult, J. Cibert, S. Tatarenko, T. Dietl, and Y. Merle d'Aubigné, Phys. Rev. Lett. **79**, 511(1997).

10. T. Dietl, H. Ohno, F. Matsukura, J. Cibert and D. Ferrand, Science, **287**, 1019 (2000).

11. A.M. Nazmul, S. Sugahara, and M. Tanaka, Phys. Rev. B, **67**, 241308 (R) (2003).

12. Y. Matsumoto, M. Murakami, T. Shono, T. Hasegawa, T. Fukumura, M. Kawasaki, P. Ahmet, T. Chikyow, S. Koshihara, H. Koinuma, Science, **291**, 854 (2001).

13. C. C. Hsieh, K. H. Wu, J. Y. Juang, T. M. Uen, J.-Y. Lin and Y. S. Gou, J. Appl. Phys. **92**, 2518 (2002).

14. R. J. Kennedy and P. A. Stampe, J. Cryst. Growth **252**, 333 (2003).

15. M. Murakami, Y. Matsumoto, K. Nakajima, T. Makino, Y. Segawa, T. Chikyow, P. Ahmet, M. Kawasaki and H. Koinuma, Appl. Phys. Lett. **78**, 2664 (2001).

16. S. R. Shinde, S. B. Ogale, S. Das Sarma, J. R. Simpson, H. D. Drew, S. E. Lofland, C. Lanci, J. P. Buban, N. D. Browning, V. N. Vulkarni, J. Higgins, R. P. Sharma, R. L. Greene, and T. Venkatesan, Phys. Rev. B, 67, 115211 (2003).

17. P. Stampe, R. Kennedy, Y. Xin, J. S. Parker, J. Appl. Phys. **92**, 7114 (2002).

18. D. H. Kim, J. S. Yang, K. W. Lee, S. D. Bu, T. W. Noh, S.–J. Oh, Y.-W. Kim, J.-S. Chung, and T. Kawai, Appl. Phys. Lett. **81**, 2421(2002).

19. S. A. Chamber, S. Thevuthasan, R. F. C. Farrow, R. F. Marks, J. U. Thiele, L Folks, M. G. Samant, A. J. Kellock, N. Ruzycki, D. L. Ederer and U. Diebold, Appl. Phys. Lett. **79**, 3467 (2001).

20. S. A. Chambers, C. M. Wang, S. Thevuthasan, T. Droubay, D. E. McCready, A. S. Lea, V. Shutthanandan, C. F. Windisch Jr, Thin Soli. Films. **418**, 197 (2002).

21. S. A. Chambers, T. Droubay, C. M. Wang, A. S. Lea, R. F. C. Farrow, L. Folks, V. Deline and S. Anders, Appl. Phys. Lett. **82**, 1257 (2003).

22. J.-Y. Kim, J.-H. Park, B.-G. Park, H.-J. Noh, S.-J. Oh, J. S. Yang, D.-H. Kim, S. D. Bu, T.-W. Noh, H.-J. Lin, H.-H. Hsieh and C. T. Chen, Phys. Rev. Lett. **90**, 017401 (2003).

23. P. A. Stampe, R. J. Kennedy, Y. Xin and J. S. Parker, J. Appl. Phys. **93**, 7864 (2003).

24. J. S. Higgins, S. R. Shinde, S. B. Ogale, T. Venkatesan and R. L. Greene, Phys. Rev. Lett. **69**, 073201 (2004).

25. L. A. Balagurov, S. O. Klimonsky, S. P. Kobeleva, A. F. Orlov, N. S. Perov and D. G. Yarkin, JETP Lett. **79**, 98 (2004).

26. X. F. Yao, T. J. Zhou, Y. X. Gai, T. C. Chong and J. P. Wang, J. Appl. Phys. 95, 7375 (2004).

27. S. R. Shinde, S. B. Ogale, J. S. Higgins, H. Zheng, A. J. Millis, V. N. Kulkarni, R. Ramesh, R. L. Greene and T. Venkatesan, Phys. Rev. Lett. **92**, 166601(2004).

28. M. L. Cui, J. Zhu, X. Y. Zhong, Y. G. Zhao and X. F. Duan, Appl. Phys. Lett. **85**, 1698 (2004).

29. D. H. Kim, J. S. Yang, Y. S. Kim, T. W. Noh, S. D. Bu, S.-I. Baik, Y.-W. Kim, Y. D. Park, S. J. Pearton, J.-H. Park, H.-J. Lin, C. T. Chen, Y. J. Song, Phys. Rev. B, **71**, 014440 (2005).

30. H. Toyosaki, T. Fukumura, Y. Yamada, K. Nakajima, C. Chikyow, T. hasegawa, H. Koinuma and M. Kawasaki, Nature Mater. **3**, 221 (2004).

31. Y. Yamada, H. Toyosaki, A. Tsukazaki, T. Fukumura, K. Tamura, S. Segawa, K. Nakajima, T. Aoyama, T. Chikyow, T. Hasegawa, H. Koinuma and M. Kawasaki, J. Appl. Phys. **96**, 5097 (2004).

32. W. K. Park, R. J. Ortega-Hertogs, J. S. Moodera, A. Punnoose and M. S. Seehra, J. Appl. Phys. **91**, 8093 (2002).

33. N. Seong, S. Yoon and C. Cho, Appl. Phys. Lett. **81**, 4209 (2002).

34. H. Yang and R. Singh, J. Appl. Phys. **95**, 7192 (2004).

35. R. J. Kennedy, P. A. Stampe, E. Hu, P. Xiong, S. von Molnár and Y. Xin, Appl. Phys. Lett. **84**, 2832 (2004).

36. D. H. Kim, J. S. Yang, Y. S. Kim, Y. J. Chang, T. W. Noh, S. D. Bu, Y.-W. Kim, Y. D. Park, S. J. Pearton and J.-H. Park, Ann. Phys. **13**, 70 (2004).

37. V. Shutthanandan, S. Thevuthasan, S. M. Heald, T. Droubay, M. H. Engelhard, T.C. Kaspar, E. E. McCready, L. Saraf, S. A. Chambers, B. S. Mun, N. Hamdan, P. Nachimuthu, B. Taylor, R. P. Sears and B. Sinkovic, Appl. Phys. Lett. **84**, 4466 (2004).

38. R I Khaibullin, L R Tagirov, B Z Rameev, Sh Z Ibragimov, F. Yıldız and B Aktaş, J. Phys.: Condens. Matter **16**, L443 (2004).

39. Y. L. Soo, G. Kioseoglou, S. Kim, Y. H. Kao, P. Sujatha Devi, J. Parise, R. J. Gambino and P. I. Gouma, Appl. Phys. Lett. **81**, 655 (2002).

40. A. Manivannan, G. Glaspell and M. S. Seehra, J. Appl. Phys. **94**, 6994 (2003).

41. Y. G. Joh, H. D. Kim, B. Y. Kim, S. I. Woo, S. H. Moon, J. H. Cho, E. C. Kim, D. H. Kim, C. R. Cho, J. Korean Phys. Soc. **44**, 360(2004).

42. H. Toyosaki, T. Fukumura, Y. Yamada and M. Kawasaki, Appl. Phys. Lett. **86**, 182503 (2005).

43. T. Fukumura, Y. Yamada, H. Toyosaki, T. Hasegawa, H. Koinuma and M. Kawasaki, Appl. Surf. Sci. **223**, 64 (2004).

44. R. Janish, P. Gopal, and N. A. Spaldin, J. Phys.: Condens. Matter. **17**, R657 (2005).

45. W. Prellier, A. Fouchet and B. Mercey, J. Phys.: Condens. Matter **15**, R1583 (2003).

46. G. Han, P. Luo, Z. Guo, F. Nahar, M. Tay, Y. Wu and S. Wang, Thin Sol. Films **505**, 137 (2006).

47. J. E. Jaffe, T. C. Droubay and S. A. Chambers, J. Appl. Phys. **97**, 073908 (2005).

48. Z. Wang, W. Wang, J. Tang L. Tung, L. Spinu and W. Zhou, Appl. Phys. Lett. **83**, 518 (2003).

49. N. H. Hong, J. Magn. Magn. Mater. **303**, 338 (2006).

50. S. A. Chambers, Surf. Sci. Rep. **39**, 105 (2000).

51. M. Joseph, H. Tabata and T. Kawai, Jpn. J. Appl. Phys. **38**, L1205 (1999).

52. K. Sato and H. Katayama-Yoshida, Jpn. J. Appl. Phys. **39**, L555 (2000).

53. H. Saeki, H. Tabata and T. Kawai, Solid State Commun. **120**, 439 (2001).

54. S. Muthukumar, J. Zhong, Y. Chen, Y. Lu and T. Siegrist, Appl. Phys. Lett. **82**, 742 (2003).

55. C. Kim, S. Leem, I. K. Robinson, W. I. Park, D. H. Kim and G.–C. Yi, Phys. Rev. B, **66**, 113404 (2002).

56. T. Wakano, N. Fujimura, Y. Morinaga, N. Abe, A. Ashida and T. Ito, Physica E, **10**, 260 (2001).

57. K. Ueda, H. Tabata and T. Kawai, Appl. Phys. Lett. 79, 988 (2001).

58. Y.-Z. Yoo, Z. Jin, T. Chikyow, T. Fukumura, M. Kawasaki and H. Koinuma, Appl. Phys. Lett. **81**, 3798 (2002).

59. T. Fukumura, Z. Jin, A. Ohtomo, H. Koinuma and M. Kawasaki, Appl. Phys. Lett. **75**, 3366 (1999).

60. X. M. Cheng and C. L. Chien, J. Appl. Phys. **93**, 7876 (2003).

61. D. S. Kim, H. Kim, S. U. Yuldashev, S. J. Lee, T. W. Kang and D. Y. Kim, J. Korean. Phys. Soc. **42**, S333 (2003).

62. A. Tiwari, C. Jin, A. Kvit, D. Kumar, J. F. Muth, J. Narayan, Solid State Commun. **121**, 371 (2002).

63. S. W. Jung, S.-J. An, G. Yi, C. U. Jung, S. Lee and S. Cho, Appl. Phys. Lett. **80**, 4561 (2002).

64. Z. Jin, T. Fukumura, M. Kawasaki, K. Ando, H. Saito, T. Sekiguchi, Y. Z. Yoo, M. Murakami, Y. Matsumoto, T. Hasegawa and H. Koinuma, Appl. Phys. Lett. **78**, 3824 (2001).

65. S-J. Han, J. W. Song, C.-H. Yang, S. H. Park, J.-H. Park, Y. H. Jeong and K. W. Rhie, Appl. Phys. Lett. **81**, 4212 (2002).

66. W. Prellier, A. Fouchet, B. Mercey, C. Simon and B. Raveau, Appl. Phys. Lett. **82**, 3490 (2003).

67. K. Rode, A. Anane, R. mattana, J.-P. Contour, O. Durand and R. LeBourgeois, J. Appl. Phys. **93**, 7676 (2003).

68. J. Kim, H. Kim, D. Kim, Y. Ihm and W. Choo, Physica B, **327**, 304 (2003).

69. J. Kim, W. Choo, H. Kim, D. Kim and Y. Ihm, J. Korean Phys. Soc. **42**, S258 (2003).

70. Y.-Z. Yoo, T. Fukumura, Z. Jin, H. Hasegawa, M. Kawasaki, P. Ahmet, T. Chikyow and H. Koinuma, J. Appl. Phys. **90**, 4246 (2001).

71. S. Lim, D. Hwang and J. Myoung, Solid State Commun. **125**, 231 (2003).

72. J. Kim, H. Kim, D. Kim, Y. Ihm and W. Choo, J. Appl. Phys. **92**, 6066 (2002).

73. H. Lee, S. Jeong, C. Cho and C. Park, Appl. Phys. Lett. **81**, 4020 (2002).

74. Y. Cho, W. Choo, H. Kim, D. Kim and Y. Ihm, Appl. Phys. Lett. **80**, 3358 (2002).

75. K. Ando, H. Saito, Z. Jin, T. Fukumura, M. Kawasaki, Y. Matsumoto and H. Koinuma, Appl. Phys. Lett. **78**, 2700 (2001).

76. D. Paul Josepha, S. Ayyappan and C. Venkateswaran, J. Alloys Compd. **415**, 225 (2006).

77. J. J. Liu, M. H. Yu and W. L. Zhou, J. Appl. Phys. **99**, 08M119 (2006).

78. D. P. Norton, S. J. Pearton, A. F. Hebard, N. Theodoropoulou, L. A. Boatner, and R. G. Wilson, Appl. Phys. Lett. **82**, 239 (2003).

79. Y. W. Heo, M. P. Ivill, K. Ip, D. P. Norton, S. J. Pearton, J. G. Kelly, R. Rairigh, A. F. Hebard, and T. Steiner, Appl. Phys. Lett. **84**, 2292 (2004).

80. M. Ivill, S. J. Pearton, D. P. Norton, J. Kelly, and A. F. Hebard, J. Appl. Phys. **97**, 053904 (2005).

81. D. P. Norton, M. Ivill, Y. Li, Y. W. Kwon, J. M. Eric, H. S. Kim, K. Ip, S. J. Pearton, Y. W. Heo, S. Kim, B. S. Kang, F. Ren, A. F. Hebard, and J. Kelly, Thin Sol. Films **496**, 160 (2006).

82. M. Venkatesan, C. B. Fitzgerald, J. G. Lunney and J. M. D. Coey, Phys. Rev. Lett. **93**, 177206 (2004).

83. C. Song, K. W. Geng, F. Zeng, X. B. Wang, Y. X. Shen, F. Pan, Y. N. Xie, T. Liu, H. T. Zhou and Z. Fan, Phys. Rev. B **73**, 024405 (2006).

84. H. Kimura, T. Fukumura, H. Koinuma and M. Kawasaki, Physica E **10**, 265 (2001).

85. H. Kimura, T. Fukumura, M. Kawasaki, K. Inaba, T. Hasegawa and H. Koinuma, Appl. Phys. Lett. **80**, 94 (2002).

86. J. Philip, N. Theodoropoulou, G. Berera, J. S. Moodera and B. Satpati, Appl. Phys. Lett. **85**, 777 (2004).

87. C. B. Fitzgerald, M. Venkatesan, L. S. Dorneles, R. Gunning, P. Stamenov, J. M. D. Coey, P. A. Stampe, R. J. Kennedy, E. C. Moreira, and U. S. Sias, Phys. Rev. B **74**, 115307 (2006).

88. S. B. Ogale, R. J. Choudhary, J. P. Buban, S. E. Lofland, S. R. Shinde, S. N. Kale, V. N. Kulkarni, J. Higgins, C. Lanci, J. R. Simpson, N. D. Browning, S. Das Sarma, H. D. Drew, R. L. Greene and T. Venkatesan, Phys. Rev. Lett. **91**, 077205 (2003).

89. K. Gopinadhan, D. K. Pandya, S. C. Kashyap and S. Chaudhary, J. Appl. Phys. **99**, 126106 (2006).

90. L. Yan, J. S. Pan and C. K. Ong, Mater. Sci. Eng. B **128**, 34 (2006).

91. J. M. D. Coey, A. P. Douvalis, C. B. Fitzgerald and M. Venkatesan, Appl. Phys. Lett. **84**, 1332 (2004).

92. W. Wang, Z. Wang, Y. Hong, J. Tang and M. Yu, J. Appl. Phys. **99**, 08M115 (2006).

93. N. H. Hong, J. Sakai, N. T. Huong, N. Poirot and A. Ruyter, Phys. Rev. B, **72**, 045336 (2005).

94. P. I. Archer and D. R. Gamelin, J. Appl. Phys. **99**, 08M107 (2006).

95. N. H. Hong, J. Sakai, W. Prellier and A. Hassini, J. Phys.: Condens. Matter **17**, 1692 (2005).

96. K. Mohan Kant, K. Chandrasekaran, S. B. Ogale, T. Venkatesan, K. Sethupathi, and M. S. R. Sao, J. Appl. Phys. **97**, 10A925 (2005).

97. Y. G. Zhao, S. R. Shinde, S. B. Ogale, J. Higgins, R. J. Choudhary, V. N. Kulkarni, R. L. Greene, and T. Venkatesan, Cond. Matt. 0209267 (2002).

98. S. N. Kale, S. B. Ogale, S. R. Shinde, M. Sahasrabuddhe, V.N. Kulkarni, R. L. Greene, and T. Venkatesan, Appl. Phys. Lett. **82**, 2100 (2003).

99. J. Wang, J. Cai, Y. Lin, and C. Nan, Appl. Phys. Lett. **87**, 202501 (2005).

100. A. H. Morrish, The Physical Principles of Magnetism, IEEE, New York (2001).

101. C. P. Bean and J. D. Livingston, J. Appl. Phys. **30**, 120S (1959).

102. L. Néel, Compt. Rend. **228**, 664 (1949).

103. M. Sawicki, T. Dietl, J. Kossut, J. Igalson, T. Wojtowicz, and W. Plesiewicz, Phys. Rev. Lett. **56**, 508 (1986).

104. Ç. Kılıç and A. Zunger, Phys. Rev. Lett. **88**, 095501 (2002).

105. B. D. Cullity, Introduction to magnetic materials (1972).

106. G. A. Held, G. Grinstein, H. Doyle, S. Sun, and C. B. Murray, Phys. Rev. B **64**, 012408 (2001).

107. G. Xiao, S. H. Liou, A. Levy, J. N. Taylor, and C. L. CHien, Phys. Rev. B **34**, 7573 (1986).

108. S. Lakkis, S. Schlenker, B. K. Chakraverty, R. Buder, and M. Marezio, Rhys. Rev. B, **14**, 1429 (1967).

109. H. Ueda, K. Kitazawa, H. Takagi, and T. Matsumoto, J. Phys. Soc. Japan, **71**, 1506 (2002).

110. P. Sheng, B. Abeles, and Y. Arie, Phys. Rev. Lett., **31**, 44(1973).

111. P. Sheng and B. Abeles, Phys. Rev. Lett. **28**, 34 (1972).

112. Y. Xin, J. Ju, P. A. Stampe, and R. J. Kennedy, Appl. Phys. Lett. **88**, 112512 (2006).

113. J. M.D. Coey, M. Venkatesan, and C. B. Fitzgerald, Nature **4**, 173(2005).

114. M. Cutler and N. F. Mott, Phy. Rev. **181**, 1336 (1969).

115. A. J. Heeger, "The Critical Regime of the Metal-Insulator Transition in Conducting Polymers: Experimental Studies", Nobel lecture (2000)

116. S. J. Potashnik, K. C. Ku, S. H. Chun, J. J. Berry, N. Samarth and P. Schiffer, Appl. Phys. Lett. **79**, 1495 (2001).

BIOGRAPHICAL SKETCH

Erhong Hu

Erhong Hu is from He-nan Province, P. R. China. She did her undergraduate studies at Tsinghua University, Beijing, P. R. China, where she received a Bachelor of Engineering in engineering physics in July 2001. That fall she was accepted in the doctoral program of the physics department at Florida State University. She received a Master of Science degree in spring 2002 from Florida Stat University. This dissertation was defended on February 21st, 2007 at Florida State University.